

Mechanical Design of Deployable Structures for a Space-Based Nulling Interferometer

Felix Wilting

Delft University of Technology



Mechanical Design of Deployable Structures for a Space-Based Nulling Interferometer

by

Felix Wilting

Instructor: J. Bouwmeester
Project Duration: September, 2024 - June, 2025
Faculty: Faculty of Aerospace Engineering, Delft

Cover: Canadarm 2 Robotic Arm Grapples SpaceX Dragon by
NASA under CC BY-NC 2.0 (Modified)

Abstract

Detecting and characterising temperate rocky exoplanets within the habitable zones of nearby stars is now a central goal in astronomy. To advance this field, ESA is developing a space-based nulling interferometer that will use multi-aperture interferometry to suppress starlight and capture a planet's mid-infrared thermal emission for detailed study. The four-aperture system must stow four 2.5 m telescopes inside the Ariane 6 long fairing and deploy them to baselines of 8 m, 16 m or 32 m in linear or X-array layouts. This thesis establishes a high-level mechanical design for the deployable structure and quantifies how structural and deployment choices govern stowed volume and dynamic behavior.

A trade-off compared articulated, truss, and telescopic mechanisms. Telescopic booms emerged as the best option that combines high stiffness with stowage efficiency. Subsequent material screening selected high-modulus pitch-based carbon-fiber-reinforced polymer for the telescopic booms, owing to its exceptional stiffness-to-density and near-zero coefficient of thermal expansion, both critical for optical-path stability. CAD assemblies confirm that both four-telescope linear and X-array configurations with baselines up to 32 m fit within Ariane 6 while stowed.

Finite-element analyses in ANSYS evaluated modal, static-deflection, and buckling performance for all configurations. The 8 m and 16 m designs satisfy the 2 Hz fundamental-frequency requirement. X-array variants achieve higher stiffness and broader frequency margins than their linear counterparts. The 32 m layouts fall short of the 2 Hz target, but preliminary analysis shows the possibilities of adopting an elliptical boom cross-section and increasing wall thickness. This lifts the L32 first mode to 2 Hz, indicating that combined shape-and-thickness optimization could allow for longer baselines to achieve the minimum 2Hz first natural frequency requirement.

Acknowledgements

First and foremost, I would like to express my sincere gratitude to my supervisor, Professor Jasper Bouwmeester, for granting me the opportunity to work on this thesis. His continuous support, guidance, and valuable advice have been instrumental throughout the course of this project.

I would also like to thank Professor Jérôme Loicq and all those involved in the Space-Based Nulling Interferometer project. In particular, I am grateful to Colin Dandumont, Guilhem Terrasa, Denis Defrère, and Romain Laugier, whose presence during the Mechanical and Thermal meetings provided insightful feedback, helpful discussions, and thought-provoking questions that significantly contributed to the development of my work.

Finally, I would like to thank my friends and family, and especially my mother, for their unwavering support and encouragement throughout this journey.

Contents

Abstract	i
Acknowledgements	ii
Abbreviations	x
1 Introduction	1
1.1 Research Objectives	2
1.2 Thesis Outline	3
2 Project Description and Context	4
2.1 Interferometry Principles	4
2.1.1 Transmission Maps	5
2.1.2 The Airy Disk and Diffraction Limit	5
2.1.3 Requirements Set by ESA on Resolution	6
2.2 Ariane 6	7
2.3 Proposed Spacecraft Topologies	8
2.3.1 Linear Dual Chopped Bracewell (DCB)	8
2.3.2 X-array	9
2.3.3 Baseline and Aperture Trade-offs	10
3 Literature Review	11
3.1 Structures	11
3.1.1 Strength, Ductility, and Toughness	11
3.1.2 Stiffness	12
3.1.3 Stress and Strain	12
3.1.4 Moments of Inertia	12
3.1.5 Torsion and Shear Strain	13
3.1.6 Deformations of Booms	14
3.1.7 Bending and Buckling	14
3.2 Dynamics and Vibrations	14
3.2.1 Vibration and Resonance	14
3.2.2 Microvibrations (Jitter)	15
3.3 Heat Shielding and Thermal Control	16
3.3.1 Thermal Expansion and Contraction	16
3.3.2 Thermal Mechanical Effects	17
3.3.3 Thermal Flutter and Jitter	17
3.3.4 Thermal Shields and Control Systems	18
3.4 Large Deployable Space Structures	19
3.4.1 The James Webb Space Telescope (JWST)	19

3.4.2	Fourier Kelvin Stellar Interferometer (FKSI)	24
4	System Constraints	29
4.1	Predefined Dimensional Constraints	29
4.2	Large Components	30
4.3	Optical and Structural Alignment Constraints	31
4.4	Thermal Constraints	31
4.5	Additional Constraints	32
5	Boom Structure Design Trade-off	33
5.1	Challenges in Deployable Boom Design	33
5.2	Boom Deployment systems	35
5.2.1	Evaluation of Deployment Technologies	35
5.2.2	Boom Deployment and spacecraft topology	38
5.2.3	Conclusion Trade-off of Deployment Mechanisms	43
5.2.4	Evaluation of Boom Materials	44
6	Telescopic Booms	46
6.1	Research findings on Telescopic booms	46
6.1.1	Telescopic Tubular Mast (TTM): Design, Features, and Performance	46
6.1.2	COMAT-CNES Telescopic Boom	49
6.1.3	Implications for Nulling Interferometer Design	51
6.2	Telescopic Boom Design	51
6.2.1	Telescopic Tube Section	51
6.2.2	Design Input Parameters	51
6.2.3	Geometric Trade-Offs: Wall Thickness vs. Outer Diameter	52
6.2.4	Section Length and Overlap Fraction	54
7	Spacecraft Designs	57
7.1	Final Components and Design Representations	57
7.1.1	Telescopic Mechanism Designs	57
7.1.2	Simplified Telescope Connection Interfaces	60
7.1.3	Boom-to-Beam Combiner Connection	60
7.1.4	Articulation and Rotation Mechanisms	60
7.2	Linear Configurations	62
7.2.1	Lin8	62
7.2.2	Lin16	62
7.2.3	Lin32	63
7.3	X-array Configurations	64
7.3.1	X8	64
7.3.2	X16	64
7.3.3	X32	65
7.4	Articulated Lin16	66
8	Structural Dynamics and Stability Analysis	67
8.1	Linear Configurations	69
8.1.1	Lin8 – Designed for 2 Hz Fundamental Frequency	69

8.1.2	Lin8 – Maximum Volume Configuration	71
8.1.3	Lin16 – Designed for 2 Hz Fundamental Frequency	73
8.1.4	Lin16 – Maximum Volume Configuration	75
8.1.5	Lin32	77
8.2	X-array Configurations	79
8.2.1	X8	79
8.2.2	X16	83
8.2.3	X32	87
8.3	Summary and Comparative Discussion	89
8.3.1	Modal Performance Comparison	89
8.3.2	Stiffness and Deflection Comparison	89
8.3.3	Buckling Capacity Comparison	90
8.3.4	Mass Comparison	90
8.3.5	Cross-Topology Observations	91
8.3.6	Conclusion	91
8.4	Improving L32 Boom Design	93
8.4.1	Effect of Elliptical Cross-Section on Natural Frequency Behavior	93
8.4.2	Effect of Increasing Wall Thickness on Natural Frequency Behavior . .	95
9	Conclusion	96
	References	99
A	Design Requirements	101
B	MATLAB Script for SCB Shape Adjustments	102

List of Figures

2.1	Nulling interferometry principles	5
2.2	Airy disk patterns	6
2.3	Usable volume beneath payload fairing in single launch - Long fairing [1]	8
2.4	Comparison of Linear Dual Chopped Bracewell array configurations: Lin8, Lin16, and Lin32.	9
2.5	Comparison of X-array configurations: X8, X16, and X32.	10
3.1	JWST artist impression[14]	19
3.2	JWST Observatory-level heat flow diagram [12].	21
3.3	JWST ISIM cryogenic radiator configuration [12].	22
3.4	JWST isolator assembly [12].	23
3.5	Artist's concept of FKSI prototype [6]	24
5.1	Deployable length versus bending stiffness[16]	36
5.2	Deployable length versus packaging ratio[16]	37
5.3	Deployable length versus boom diameter[16]	38
5.4	Spacecraft Bus Design	40
5.5	M1 mirror Telescope assembly	41
5.6	Beam Combiner approximation	41
5.7	Visualization of the Ariane 6 fairing: (a) Halved 3D model showing interior shape, (b) top view with large components, and (c) side view confirming stowed configuration feasibility.	42
6.1	Deployed stiffness test configuration for the Telescopic Tubular Mast (TTM), Developed by Astro Aerospace, a division of Northrop Grumman Aerospace Systems[13]	47
6.2	STEM used for deployment of TTM	48
6.3	(a) Tapered pins used for latching and (b) Telescopic boom retraction sequence.	48
6.4	COMAT-CNES Telescopic boom 6-Tube configuration	49
7.1	Interface between two telescopic boom sections	57
7.2	4 m boom with 2 sections: stowed and deployed configurations	58
7.3	8 m boom with 2 sections: stowed and deployed configurations	58
7.4	8 m boom with 4 sections: stowed and deployed configurations	59
7.5	16 m boom with 4 sections: stowed and deployed configurations	59
7.6	Simplified connection geometries for mid and end telescope mounting	60
7.7	Simplified example of booms connecting to the central beam combiner	60
7.8	Simplified articulation and rotation mechanism: stowed and deployed	61
7.9	Lin8 spacecraft configuration in its stowed and deployed states designed for a 2 Hz fundamental frequency	62

7.10 Lin16 spacecraft configuration in its stowed and deployed states designed for a 2 Hz fundamental frequency	63
7.11 Lin32 in its stowed and deployed states designed for full fairing diameter utilization	63
7.12 X8 spacecraft configuration in its stowed and deployed states designed for a 2 Hz fundamental frequency	64
7.13 X16 spacecraft configuration in its stowed and deployed states designed for a 2 Hz fundamental frequency	65
7.14 X32 spacecraft configuration in its stowed and deployed states designed for full fairing diameter utilization	65
7.15 Articulation mechanisms used in the articulated Lin16 spacecraft	66
7.16 Articulated Lin16 spacecraft configuration in its stowed and deployed states . .	66
8.1 First four mode shapes of the Lin8 spacecraft designed for a 2 Hz fundamental frequency	69
8.2 First four mode shapes of the Lin8 spacecraft in the maximum volume configuration	71
8.3 First four mode shapes of the Lin16 spacecraft designed for a 2 Hz fundamental frequency	73
8.4 First four mode shapes of the Lin16 spacecraft in the maximum volume configuration	75
8.5 First four mode shapes of the Lin32 spacecraft	77
8.6 First four mode shapes of the X8 spacecraft designed for a 2 Hz fundamental frequency	79
8.7 First four mode shapes of the X8 spacecraft in the maximum volume configuration	81
8.8 First four mode shapes of the X16 spacecraft designed for a 2 Hz fundamental frequency	83
8.9 First four mode shapes of the X16 spacecraft in the maximum volume configuration	85
8.10 First four mode shapes of the X32 spacecraft	87
8.11 Elliptical boom	93
8.12 Simplified Lin32 using elliptical booms	93

List of Tables

5.1	Spacecraft Topology Deployment Requirements	39
5.2	Scoring comparison of candidate boom deployment mechanisms for the nulling interferometer mission (scores range from 1 (poor) to 5 (excellent))	44
5.3	Comparison of Candidate Materials for Deployable Boom Structure	45
6.1	Effect of Wall Thickness on First Natural Frequency, Relative Area, and Efficiency	53
6.2	Effect of Outer Diameter on First Natural Frequency, Relative Area, and Efficiency	54
6.3	Telescopic Boom Design Parameters Across L and X Topologies (All lengths in meters)	56
8.1	Natural frequency values for the Lin8 spacecraft designed for a 2 Hz fundamental frequency (first 6 modes)	69
8.2	Structural performance of L8 topology	70
8.3	Natural frequency values for the Lin8 spacecraft in the maximum volume configuration (first 6 modes)	71
8.4	Structural performance of L8 Max Volume topology	72
8.5	Natural frequency values for the Lin16 spacecraft designed for a 2 Hz fundamental frequency (first 6 modes)	73
8.6	Structural performance of L16 topology	74
8.7	Natural frequency values for the Lin16 spacecraft in the maximum volume configuration (first 6 modes)	75
8.8	Structural performance of L16 Max Volume topology	76
8.9	Natural frequency values for the Lin32 spacecraft (first 6 modes)	77
8.10	Structural performance of L32 topology	78
8.11	Natural frequency values for the X8 spacecraft designed for a 2 Hz fundamental frequency (first 6 modes)	79
8.12	Structural performance of X8 topology	80
8.13	Natural frequency values for the X8 spacecraft in the maximum volume configuration (first 6 modes)	81
8.14	Structural performance of X8 Max Volume topology	82
8.15	Natural frequency values for the X16 spacecraft designed for a 2 Hz fundamental frequency (first 6 modes)	83
8.16	Structural performance of X16 topology	84
8.17	Natural frequency values for the X16 spacecraft in the maximum volume configuration (first 6 modes)	85
8.18	Structural performance of X16 Max Volume topology	86
8.19	Natural frequency values for the X32 spacecraft (first 6 modes)	87
8.20	Structural performance of X32 topology	88
8.21	Fundamental natural frequencies for all topologies	89

- 8.22 Tip deflection and equivalent stiffness under 1 N load 89
- 8.23 Critical buckling loads for all configurations 90
- 8.24 Structural mass of the deployable truss for each topology and packaging variant (telescope and bus masses are identical for all concepts and are therefore omitted). 90
- 8.25 First four natural frequencies for L32 configurations 94
- 8.26 First four natural frequencies for elliptical boom with a wall thickness of 2 mm . 95
- 8.27 First four natural frequencies for elliptical boom with a wall thickness of 2.1 mm 95

- A.1 List of scientific (SREQ), functional (FREQ), and technical (TREQ) requirements.101

Abbreviations

Abbreviation	Description
ANSYS	(Ansys Inc.) commercial finite-element software
CAD	Computer-Aided Design
CFRP	Carbon-Fibre-Reinforced Polymer
CJAA	Cryocooler Jitter Attenuation Assembly
CTE	Coefficient of Thermal Expansion
DCB	Dual Chopped Bracewell
ESA	European Space Agency
FEA	Finite Element Analysis
FKSI	Fourier Kelvin Stellar Interferometer
IWA	Inner Working Angle
JWST	James Webb Space Telescope
L2	Second Sun–Earth Lagrange Point
LEO	Low-Earth Orbit
LOS	Line-of-Sight
MIR	Mid-InfraRed wavelength band
MIRI	Mid-InfraRed Instrument
MTMD	Magnetically Tuned Mass Damper
NIRCam	Near-InfraRed Camera
NIRSpec	Near-InfraRed Spectrograph
OTE	Optical Telescope Element
PAN	Polyacrylonitrile (precursor fibre for CFRP)
RWA	Reaction Wheel Assembly
RWIA	Reaction Wheel Isolator Assembly
SCB	SpaceCraft Bus
STEM	Storable Tubular Extendable Mechanism
TTM	Telescopic Tubular Mast

1

Introduction

The detection and characterization of exoplanets, particularly temperate rocky exoplanets within the habitable zones of nearby stars, has become a central goal in modern astronomy. To advance this field, the European Space Agency (ESA) is conducting a study to develop a space-based nulling interferometer. This mission will utilize multi-aperture interferometry to suppress starlight, enabling the detection of faint planetary signals. The primary objective is to directly observe exoplanets by capturing their thermal emissions in the mid-infrared range, allowing for detailed characterization [10].

This thesis focuses on the high-level mechanical design of the deployables for this nulling interferometer, addressing the unique challenges posed by the mission, including those associated with operating at the second Lagrange point (L2). Key objectives include the identification of inputs necessary for the top-level mechanical design, outputs affecting the optical system, and the development of a stowage and deployment strategy compatible with the Ariane 6 launch configuration. The thesis also involves 3D modeling to verify spacecraft sizing and the development of the boom deployment systems, with attention to vibrational response and deployment accuracy.

The spacecraft will feature a single-spacecraft design and is scheduled to be launched aboard an Ariane 6 rocket. Once in space, it will utilize advanced optical techniques to carry out its observations. By suppressing the overwhelming brightness of the host star, the interferometer can isolate the faint thermal emissions of the exoplanet, providing critical information about its atmosphere, surface properties, and potential habitability.

The spacecraft will be positioned at the second Lagrange point (L2), a region of space where the gravitational forces between the Earth and the Sun create a stable environment for space observatories. At L2, the spacecraft experiences minimal interference from Earth's radiation and can maintain a relatively stable position with minimal orbital adjustments. Unlike low Earth orbit (LEO), where day-night cycles cause frequent temperature variations, L2 offers a constant exposure to sunlight.

While this continuous exposure simplifies thermal gradient management, it also presents significant challenges in terms of thermal control. The spacecraft's sensitive infrared (IR) detectors

require extremely low temperatures to operate effectively, necessitating both active and passive cooling techniques. Sun shields will be deployed to block direct sunlight, and the thermal design must ensure that these shields maintain their effectiveness throughout the mission. Proper thermal management is critical to preserving the optical alignment and functionality of the interferometer.

The spacecraft will rely on deployable booms to increase the interferometer's baseline, thereby improving its angular resolution. These booms will position the apertures at precise distances to enhance the mission's capability to suppress starlight. However, the use of larger booms also necessitates larger sun shields, which must all fit within the Ariane 6 launch vehicle. This presents critical engineering challenges, as not only the booms and sun shields, but also the telescopes, beam combiner, and spacecraft bus must be designed to fit the Ariane 6 launch vehicle. Once in orbit, these structures must deploy efficiently and accurately to ensure the spacecraft meets its observational goals. These design elements are currently being evaluated as part of the mission's ongoing trade-off studies [17].

The mission is governed by a series of scientific, functional, and technical requirements (see Table A.1 in appendix A). These requirements focus on the instrument's ability to detect and characterize temperate rocky exoplanets, observe thermal light, and use advanced interferometric techniques while ensuring compatibility with launch constraints.

1.1. Research Objectives

The primary focus of this thesis is to explore the impact of various design factors on the overall volume of a space-based nulling interferometer spacecraft. Specifically, it seeks to answer the following main research question:

How do changes in structural and deployment design factors affect the overall volume of a nulling interferometer spacecraft, and how can these factors be managed to ensure its fit within the Ariane 6?

This thesis focuses on the high-level mechanical design of the deployables for this nulling interferometer, addressing the unique challenges posed by the mission at L2. Key objectives include the identification of inputs necessary for the top-level mechanical design, outputs affecting the optical system, and the development of a stowage and deployment strategy compatible with the Ariane 6 launch configuration. The thesis also involves 3D modeling to verify spacecraft sizing and the development of the boom deployment systems, with attention to vibrational response and deployment accuracy.

It has been decided to explore two generic configurations[10]: The 4T linear and The 4T X-array, determined through a trade-off process in September 2024. The following research goals have been outlined:

- Identifying key inputs for the mechanical design and understanding their impact on the optical system.
- Sizing the booms and deployment mechanisms, ensuring they meet vibrational stability requirements and offer precise deployment control.
- Developing a stowage and deployment strategy for integration with the Ariane 6 launch

vehicle.

- Conducting 3D modeling to verify spacecraft dimensions and ensure proper stowage.

1.2. Thesis Outline

This thesis is structured into nine chapters, followed by references and two appendices. Each chapter builds upon the previous to develop a comprehensive mechanical design for a nulling interferometer deployable system compatible with Ariane 6.

Chapter 2 – Project Description and Context Reviews the principles of nulling interferometry and establishes the top-level mission architecture. It summarizes Ariane 6 fairing dimensions and constraints, introduces the 4T linear and 4T X-array configurations, and details baseline and aperture trade-offs that informed subsequent design choices.

Chapter 3 – Literature Review Surveys relevant information and prior work in key areas. On structural design, dynamics and vibrations, thermal control and reviews in depth relevant large deployable spacecraft

Chapter 4 – System Constraints Specifies the predefined dimensional constraints, defines large spacecraft components, details optical and structural alignment requirements and details thermal requirements.

Chapter 5 – Boom Structure Design Trade-off Examines the challenges associated with long-baseline structure design. It compares telescopic tubes, articulated mechanisms, and deployable-truss concepts in detail. After this trade-off a material for the structural design is chosen based on performance criteria.

Chapter 6 – Telescopic Boom Design Reviews existing telescopic mast technologies (e.g., Telescopic Tubular Mast and COMAT-CNES designs) and derives sizing for nested tubes. Sections 6.2 and 6.3 develop the geometric design parameters for all telescopic boom topologies.

Chapter 7 – Spacecraft Designs Presents the final components for both 4T linear and 4T X-array topologies. It introduces CAD assemblies of the spacecraft topologies in their stowed and deployed states, verifying that nested telescopic sections, articulation joints, the beam-combiner and spacecraft bus all fit within the Ariane 6 envelope.

Chapter 8 – Structural Dynamics and Stability Analysis Evaluates the structural dynamics and stability analysis results for all spacecraft topologies by looking at mode shapes and natural frequencies, tip stiffness, and buckling loads across configurations. Additionally it briefly explores geometric enhancements (elliptical cross-section, increased wall thickness) to approach a 2 Hz fundamental frequency for 32 m booms.

Chapter 9 – Conclusion Concludes the principal findings and answers the research question and proposes directions for future work.

2

Project Description and Context

Observing exoplanets, particularly terrestrial ones that could harbor life, is an immense challenge due to the overwhelming brightness of their host stars. A planet orbiting a star emits only a tiny fraction of the light compared to its star, making it difficult to detect against the stellar glare. The problem is twofold: contrast and angular resolution. A conventional telescope attempting to observe a rocky exoplanet in the infrared spectrum would struggle because the host star's light is millions to billions of times brighter, depending on the wavelength you want to measure. This intense starlight saturates the detector, rendering the faint planetary signal undetectable. Even if the detector were sensitive enough, a single telescope's diffraction limit prevents it from resolving the exoplanet separately from its star. On Earth, the solution to increasing angular resolution is to build larger telescopes. A larger primary mirror allows for finer details to be resolved, which is why ground-based observatories continue to expand in size. However, this approach has fundamental limitations in space. Launching a monolithic space telescope with a mirror larger than 30 meters in diameter—necessary to achieve the resolution needed to distinguish exoplanets—remains infeasible due to size, weight, and deployment constraints. Moreover, even such a large telescope would still struggle with the contrast problem, as reducing the star's overwhelming brightness is equally crucial.

To overcome these challenges, nulling interferometry is employed. This technique combines light from multiple smaller telescopes to synthetically create a much larger effective aperture. By using destructive interference, the light from the host star can be suppressed, effectively “nulling” it out while allowing the much fainter planetary light to be detected. This approach circumvents the diffraction limit of individual telescopes and directly addresses the contrast problem, enabling the study of exoplanets in detail.

2.1. Interferometry Principles

Interferometry leverages the principle of superposition of light waves, where the amplitudes of waves combine constructively or destructively depending on their phase difference. Nulling interferometry employs destructive interference by introducing a phase shift of π radians (180°) in one optical path, effectively canceling coherent, centrally symmetric starlight while leaving the faint exoplanetary signal detectable. To achieve coherent combination of light from multiple

telescopes, optical path differences (OPDs) between beams must be minimized. Delay lines, consisting of movable mirrors or prisms, introduce precise optical path corrections to account for variations caused by telescope spacing and the direction of the observed source. An example of the workings of a Nulling interferometer is shown in Figure 2.1a

2.1.1. Transmission Maps

Transmission maps illustrate the spatial regions where light is transmitted or suppressed by an interferometric system. In nulling interferometry, these maps show how starlight is canceled, regions of destructive interference, while allowing off-axis planetary light to pass through. For example, Figure 2.1b demonstrates the transmission map for a planet orbiting a star observed by a Bracewell interferometer. The null regions align with the starlight, while planetary light at specific off-axis positions remains detectable. Transmission maps are used for evaluating system performance, as they reveal the interferometer's ability to suppress stellar light and isolate planetary signals. Misalignments or imperfections can reduce null depth, limiting the interferometer's sensitivity and contrast.

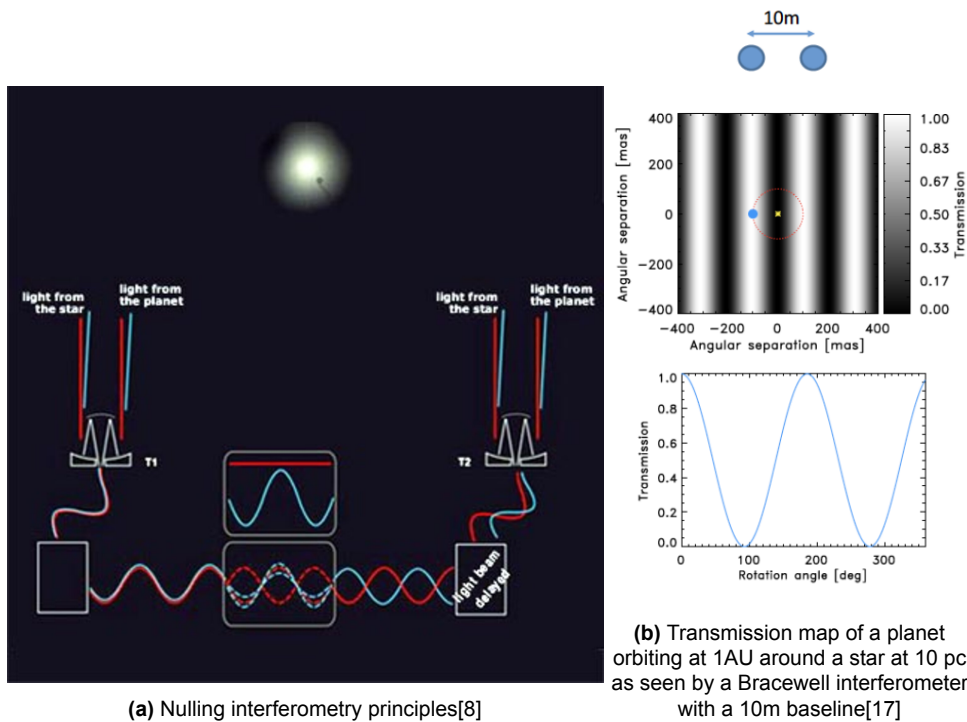


Figure 2.1: Nulling interferometry principles

2.1.2. The Airy Disk and Diffraction Limit

The resolving power of a telescope is fundamentally limited by diffraction, which arises due to the wave nature of light. The light entering a circular aperture produces a diffraction pattern known as the Airy disk, consisting of a central bright spot surrounded by rings of decreasing intensity. The angular resolution limit of a telescope, determined by the first minimum of the Airy pattern, is given by:

$$\theta = 1.22 \frac{\lambda}{D}, \quad (2.1)$$

where θ is the angular resolution, λ is the wavelength of observation, and D is the diameter of the telescope aperture.

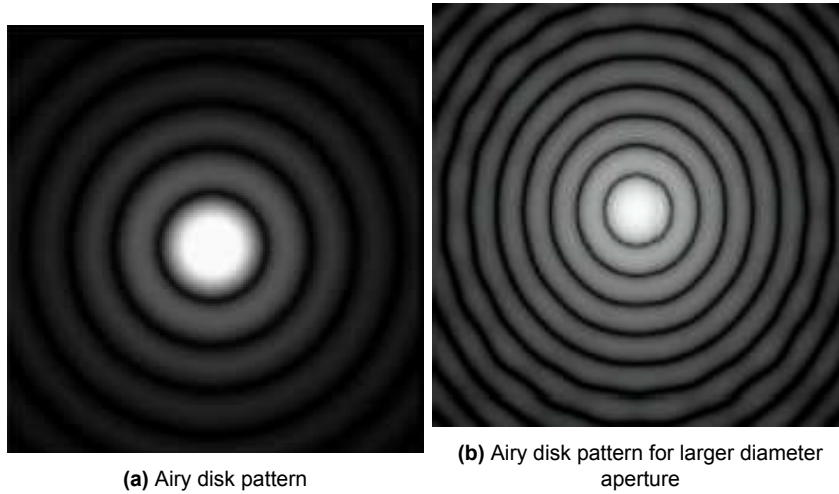


Figure 2.2: Airy disk patterns

The size of the Airy disk determines the smallest angular separation between two light sources that a telescope can resolve. For larger apertures, the Airy disk shrinks, improving angular resolution. In interferometry the effective aperture is determined by the baseline b between telescopes[20]:

$$\theta = \frac{\lambda}{b}. \quad (2.2)$$

This relationship demonstrates that interferometric baselines effectively overcome diffraction limits, allowing much finer resolution equivalent to that of a single telescope with an aperture equal to the baseline length.

2.1.3. Requirements Set by ESA on Resolution

The European Space Agency (ESA) has outlined detailed performance criteria for a nulling interferometer designed to detect and characterize Earth-like exoplanets. The mission is governed by a series of scientific, functional, and technical requirements, which are summarized in Table A.1 in Appendix A. These requirements encompass angular resolution, spectral performance, and system configuration, all tailored to achieve the mission's scientific objectives in the mid-infrared (MIR) range, as detailed in ESA's technical notes [10].

Observing Wavelength Range The nulling interferometer will operate within the mid-infrared spectrum, spanning wavelengths from 3 μm to 20 μm . This range is crucial for studying planetary atmospheres, as it includes key spectral features such as water vapor, carbon dioxide, ozone, and methane. Detecting these molecules enables the characterization of potentially habitable exoplanets and the search for biosignatures.

Inner Working Angle (IWA) The Inner Working Angle (IWA) defines the smallest angular separation between a star and a planet where the interferometer can effectively suppress starlight while detecting the planetary signal. For this mission, the IWA must be less than

300 milliarcseconds (mas) at a wavelength of 10 μm . The IWA is directly influenced by the interferometer's baseline length b and the observing wavelength λ , as described by:

$$\text{IWA} \approx \frac{\lambda}{2b}. \quad (2.3)$$

While the formula is the same as for angular resolution, the IWA specifically refers to the instrument's capability to detect planets near a star, considering practical starlight suppression, whereas angular resolution defines the instrument's ability to distinguish two closely spaced objects.

Spectral Resolution The interferometer must achieve a minimum spectral resolution of 20, allowing the system to differentiate between various molecular signatures in planetary atmospheres. Higher spectral resolutions improve the precision of atmospheric characterization but also require advanced beam-combining optics and detector technologies.

Apertures and Configuration The proposed spacecraft design will utilize four apertures with diameters ranging from 2 to 3 meters, chosen to balance light-gathering power, nulling performance, and practical constraints related to stowage and deployment within the Ariane 6 payload fairing. Using multiple apertures improves sensitivity by increasing collected flux and enhances null-depth through multiple nulling stages, following a Double Bracewell configuration. The range of aperture sizes offers a balance between light-gathering power and the constraints of stowage within the Ariane 6 payload fairing. The exact size of the apertures is yet to be determined and will be refined through further research and design trade-offs. For this thesis an aperture diameter of 2.5 meters will be assumed.

2.2. Ariane 6

The nulling interferometer spacecraft must be designed to fit within the payload fairing of the Ariane 6, Europe's next-generation heavy-lift launch vehicle. Operated by Arianespace and primarily built by ArianeGroup, Ariane 6 comes in two configurations: the Ariane 62 with two solid rocket boosters for lighter payloads and the Ariane 64 with four boosters for maximum lift capabilities [1]. This modularity allows Ariane 6 to support a wide array of missions, from deploying large constellations of small satellites to sending payloads into geostationary orbits and even beyond to lunar and deep-space missions.

Ariane 6's payload fairing, particularly in the long configuration, is designed for versatility. With an external height of 20 meters and a diameter of 5.4 meters, this fairing allows for a maximum payload mass of up to 11,500 kg to geostationary transfer orbit (GTO) in the Ariane 64 setup. This generous capacity supports the launch of large and complex payloads, either as a single mission or in dual configurations for added efficiency.

The fairing also offers an additional usable volume extension, subject to specific analyses to confirm feasibility and ensure compliance with the structural stability requirements of Ariane 6. This extension allows for certain protrusions or configurations that exceed the standard volume limits. Based on the measurements shown in Figure 2.3, the extended internal volume provides approximately 259.15 cubic meters, compared to 242.27 cubic meters without extension, representing a 7% increase in usable space. According to Chapter 4 of the tech-

of combined light to suppress starlight while enhancing sensitivity to off-axis planetary signals. The linear array is characterized by its straightforward geometry, which simplifies deployment mechanisms and alignment. The simplest configuration of the linear array fits entirely within the Ariane 6 payload fairing without requiring deployment mechanisms to space the telescopes apart. However, to improve the scientific yield, two additional configurations are proposed: one that doubles the baseline length and another that quadruples it. These configurations, referred to as Lin8, Lin16, and Lin32, represent baseline lengths of 8 meters, 16 meters, and 32 meters, respectively. While these extensions enhance angular resolution and the achievable Inner Working Angle (IWA), they also increase the stowage volume and structural complexity, particularly for the longer baselines. Figures 2.4a, 2.4b, and 2.4c illustrate these configurations within the Ariane 6 fairing. For the two larger baseline lengths, deployable booms are required to position the telescopes after launch. The trade-off analysis assumes that the telescopes are aligned with the vertical plane of the launch vehicle to avoid additional rotational deployments and maximize the available volume for deployable booms and sunshields.

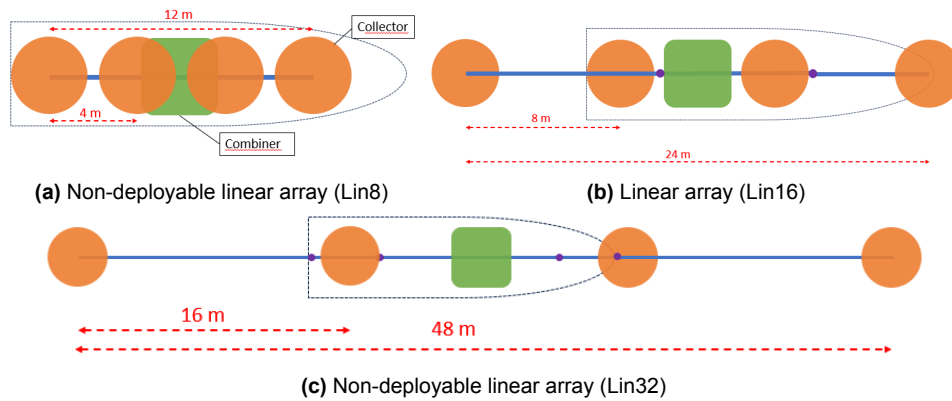


Figure 2.4: Comparison of Linear Dual Chopped Bracewell array configurations: Lin8, Lin16, and Lin32.

2.3.2. X-array

The X-array topology arranges four apertures in a rectangular configuration with an aspect ratio of 2:1. This design decouples nulling and imaging functions, with the shorter axis dedicated to starlight suppression and the longer axis enhancing angular resolution. The X-array's configuration lends itself naturally to techniques for removing instability noise and improves the interferometers ability to distinguish between multi planets[10]. Unlike the linear array, the simplest X-array configuration cannot fit entirely within the Ariane 6 payload fairing without deployment mechanisms. At least one rotational deployment is required to position the telescopes into their final configuration. More rotational deployments or other types of deployment mechanisms will be required to reach the final telescope positions for larger baselines. Similar to the linear array, the X-array has three baseline options: X8, X16, and X32, representing baseline lengths of 8 meters, 16 meters, and 32 meters, respectively. Figures 2.5a, 2.5b, and 2.5c illustrate these configurations within the Ariane 6 fairing, detailing the required rotational joints and stowage constraints. For the simplest 2:1 X-array configuration, at least two rotational deployments are necessary to align the telescopes post-launch. Additional challenges arise from the need to fit deployable booms and sunshields within the available volume. To maintain feasibility, the design assumes telescopes are pre-aligned in the vertical plane of

the launch vehicle. Horizontal alignment would require additional 90-degree rotations of individual telescopes, which would severely limit the available room for deployable components. Additionally, telescopes cannot be stowed behind each other due to fairing depth constraints.

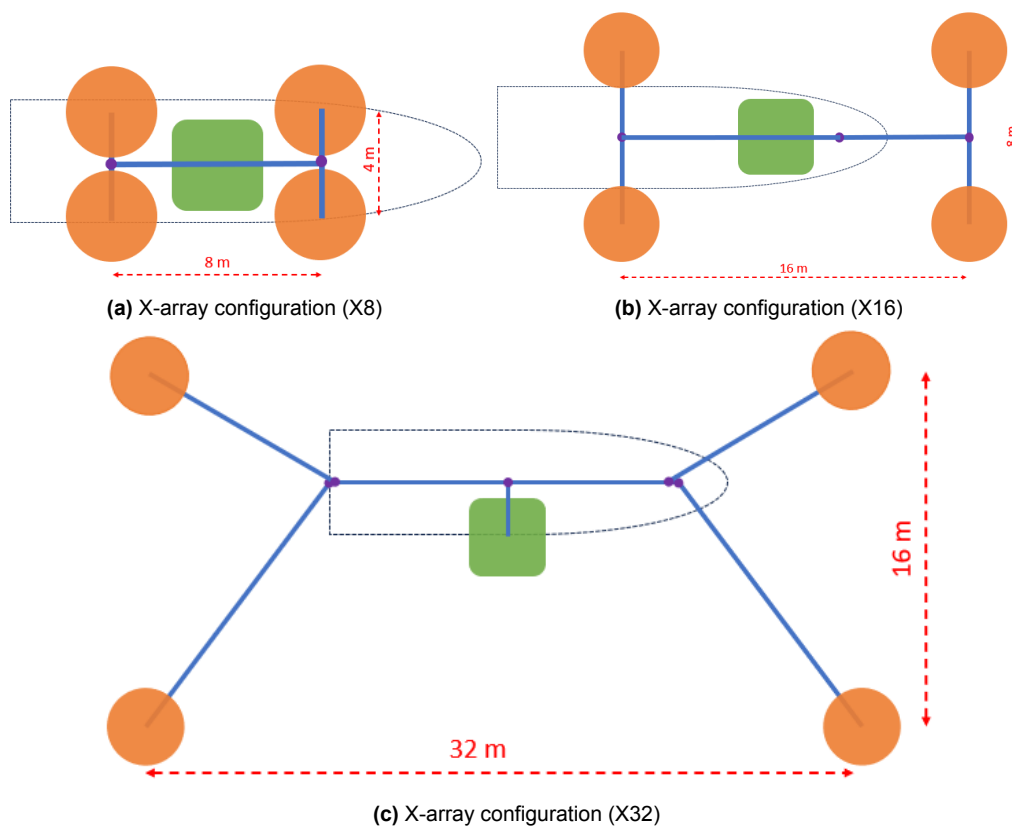


Figure 2.5: Comparison of X-array configurations: X8, X16, and X32.

2.3.3. Baseline and Aperture Trade-offs

Both the linear and X-array topologies involve baseline lengths and aperture sizes that significantly impact stowage, deployment, and scientific performance. Longer baselines improve the achievable IWA and angular resolution, while aperture diameters of 2 to 3 meters enhance light-gathering capabilities. However, increasing baseline lengths introduces additional deployment complexity, increases spacecraft volume and increases structural challenges. Figures 2.4 and 2.5 detail the configurations within the Ariane 6 fairing for various baseline lengths. These figures also highlight the deployment strategies and required rotational joints where applicable.

3

Literature Review

3.1. Structures

The design and analysis of the spacecraft structure for the nulling interferometer require a thorough understanding of several key structural properties. These properties, including strength, stiffness, ductility, moments of inertia, and torsional behavior, are essential for ensuring that the spacecraft can withstand the challenging conditions of space, from the launch environment to long-term operation at the second Lagrange point (L2). In addition to these structural properties, managing vibrations is crucial for the mission's success, especially in relation to the spacecraft's optical alignment. Vibrations, whether induced during launch or from in-orbit disturbances, can interfere with the precise positioning of optical instruments. Damping mechanisms are therefore vital to mitigate these vibrations and ensure the high degree of stability required for accurate nulling interferometry. This section provides the necessary background on these fundamental mechanical properties, which will be critical in evaluating the mechanical design of deployable structures, booms, sun shields, and vibration control strategies for the nulling interferometer mission.

3.1.1. Strength, Ductility, and Toughness

Strength, ductility, and toughness are fundamental mechanical properties of materials used in spacecraft structures. Strength is the material's ability to resist deformation or failure under applied loads. Materials with high strength are crucial for components subjected to high stresses, such as spacecraft frames and support structures. Ductility refers to the ability of a material to undergo plastic deformation before breaking. Ductile materials can absorb more energy during loading, making them ideal for components that experience dynamic or impact loads. Toughness is a combination of strength and ductility, representing the material's ability to absorb energy before fracturing. In spacecraft, materials with high toughness are essential to ensure they can withstand sudden loads or shocks during launch or collisions with space debris [19].

3.1.2. Stiffness

Stiffness is the resistance of a material or structure to deformation when subjected to an applied force. It is characterized by the modulus of elasticity (Young's modulus, E) and is critical for maintaining the alignment and performance of spacecraft components, especially in precision systems like antennas and optical instruments. The stiffness of a component can be expressed as:

$$k = \frac{EA}{L} \quad (3.1)$$

where E is the modulus of elasticity, A is the cross-sectional area, and L is the length of the component. Stiffness ensures that deployable booms, for example, maintain their shape and do not bend excessively under operational loads [19].

3.1.3. Stress and Strain

Stress and strain are fundamental concepts in the analysis of structural behavior. Stress is the internal force per unit area within a material, typically measured in Pascals (Pa). It helps determine whether a material will withstand an applied load or fail. The formula for normal stress is:

$$\sigma = \frac{F}{A} \quad (3.2)$$

where σ is the stress, F is the applied force, and A is the cross-sectional area over which the force is applied. Strain is the measure of deformation resulting from an applied stress and is a dimensionless quantity. It represents the change in length relative to the original length of the material:

$$\varepsilon = \frac{\Delta L}{L_0} \quad (3.3)$$

where ΔL is the change in length, and L_0 is the original length. Stress and strain relationships are essential for evaluating how spacecraft structures behave under various load conditions during launch, deployment, and operation in space [19].

3.1.4. Moments of Inertia

The moments of inertia of a cross-section are fundamental properties that describe its resistance to bending and twisting. These properties are critical in the design and analysis of structural elements, including spacecraft components that are subjected to complex loading conditions such as bending and torsion.

The area moment of inertia reflects the ability of a cross-section to resist bending. For any arbitrary cross-section, the area moments of inertia about the x -axis and y -axis are given by:

$$I_x = \int y^2 dA \quad \text{and} \quad I_y = \int x^2 dA \quad (3.4)$$

where dA represents an infinitesimal area of the cross-section, and x and y are the coordinates of the area element relative to the centroidal axes. The area moment of inertia is essential for predicting the deflection and stresses in beams and other elements subjected to bending.

Additionally, the parallel axis theorem is used to calculate the moment of inertia about any axis

parallel to one through the centroid. The theorem states:

$$I = I_c + Ad^2 \quad (3.5)$$

where I_c is the moment of inertia about the centroidal axis, A is the area of the section, and d is the distance between the centroidal axis and the axis of interest.

The polar moment of inertia, also known as the second polar moment of area, describes the resistance of a cross-section to torsion or twisting. It is particularly relevant for components subjected to rotational or torsional loads. The polar moment of inertia about the z -axis (perpendicular to the cross-section) is given by:

$$J = \int (x^2 + y^2) dA \quad (3.6)$$

where dA is the differential area, and x and y are the coordinates of the area element with respect to the centroid of the section.

The polar moment of inertia can also be related to the area moments of inertia:

$$J = I_x + I_y \quad (3.7)$$

This relationship highlights that the polar moment of inertia is the sum of the area moments of inertia about two perpendicular axes in the plane of the cross-section. It is a crucial property in the design of components such as spacecraft booms, antennae, or deployable structures, where both bending and torsional stiffness must be accounted for to ensure structural integrity and optimal performance.

3.1.5. Torsion and Shear Strain

Torsion occurs when a structural element, such as a bar or shaft, is subjected to a twisting moment or torque. The deformation due to torsion is characterized by the angle of twist, θ , which is related to the applied torque T , the length of the bar L , the shear modulus G , and the polar moment of inertia J :

$$\theta = \frac{TL}{GJ} \quad (3.8)$$

where: T is the applied torque, L is the length of the bar, G is the shear modulus, and J is the polar moment of inertia of the cross-section.

The shear modulus G is a material property that describes the material's response to shear stress. It is related to the material's ability to resist deformation under shear loads and is linked to the material's elastic behavior in response to torsional forces. For small angles of shear strain, γ , the relationship between shear strain and the angle of twist can be expressed as:

$$\gamma = \frac{\theta r}{L} \quad (3.9)$$

where r is the radius of the bar or shaft. In axisymmetric cases, such as circular shafts, the shear strain is uniform along the circumference, and the twist is proportional to the applied torque. This relationship is crucial in designing spacecraft components like deployable booms, which must resist twisting while maintaining structural integrity [19].

3.1.6. Deformations of Booms

Deployable booms in spacecraft structures undergo various types of deformations, including axial, bending, and torsional deformations. The axial deformation of a boom subjected to a tensile or compressive load is given by:

$$\delta = \frac{FL}{EA} \quad (3.10)$$

where F is the applied axial load, L is the length of the boom, E is Young's modulus, and A is the cross-sectional area. Bending and torsion can also induce deformations, which must be minimized to maintain the performance of the spacecraft's instruments or solar arrays attached to the booms. Proper analysis of these deformations helps ensure that the booms operate within their structural limits during both deployment and operational phases [19].

3.1.7. Bending and Buckling

Bending occurs when a structural element experiences a moment or lateral load that causes it to curve. The resulting stresses and deflections are critical in determining the performance of spacecraft structures, especially long elements like booms and trusses. Buckling, on the other hand, is a failure mode that occurs when compressive forces cause a structure to collapse or deform uncontrollably. Preventing buckling is especially important in lightweight, slender structures like spacecraft panels and booms, which are subject to compressive loads during launch and in space [19].

The critical buckling load for a slender column is given by Euler's formula:

$$P_{cr} = \frac{\pi^2 EI}{(KL)^2} \quad (3.11)$$

where E is the modulus of elasticity, I is the area moment of inertia, L is the length of the column, and K is the effective length factor, which depends on the boundary conditions.

3.2. Dynamics and Vibrations

Spacecraft structures are subject to various dynamic loads throughout their lifecycle. These loads can range from the intense vibrations experienced during launch to microvibrations in orbit, which can affect the performance of sensitive instruments. Managing vibrations is crucial to ensure structural stability and maintain the precise alignment required by systems such as antennas and optical instruments.

3.2.1. Vibration and Resonance

Vibration occurs when mechanical systems are subjected to dynamic loads, resulting in oscillatory motion. Resonance is particularly dangerous in spacecraft structures because it can occur when the frequency of external forces (such as engine vibrations or environmental disturbances) matches the natural frequency of the spacecraft's components. This can lead to large amplitude vibrations, potentially causing structural damage or failure. The natural frequency f_n of a structural element can be calculated as:

$$f_n = \frac{1}{2\pi} \sqrt{\frac{k}{m}} \quad (3.12)$$

where: k is the stiffness of the structure, and m is the mass of the structure.

When a structure is subjected to an external force with frequency ω_f , the response of the system can be described by the following equation of motion:

$$m\ddot{x}(t) + c\dot{x}(t) + kx(t) = F_0 \cos(\omega_f t) \quad (3.13)$$

where: m is the mass of the structure, c is the damping coefficient, k is the stiffness, F_0 is the amplitude of the external force, and ω_f is the forcing frequency.

The response of the structure becomes particularly dangerous when the forcing frequency ω_f matches the natural frequency ω_0 , leading to resonance. The amplitude of the vibrations is then given by:

$$A(\omega_f) = \frac{F_0}{\sqrt{(k - m\omega_f^2)^2 + (c\omega_f)^2}} \quad (3.14)$$

At resonance, when $\omega_f = \omega_0$, the amplitude can increase significantly, especially in lightly damped systems. The Dynamic Amplification Factor can be approximated as:

$$\text{Dynamic Amplification Factor} = \frac{1}{2\zeta} \quad (3.15)$$

where ζ is the damping ratio of the structure. Lower damping leads to higher amplification, making resonance a critical issue in spacecraft design. Spacecraft undergo extensive vibration testing during development to simulate launch loads and identify resonant frequencies. This testing helps avoid failure modes caused by resonance by enabling engineers to fine-tune the structural design. Damping mechanisms, such as viscoelastic materials or tuned mass dampers, are often incorporated into the spacecraft design to minimize the effects of resonance by dissipating the vibrational energy into heat.

3.2.2. Microvibrations (Jitter)

Microvibrations, or jitter, refer to small amplitude vibrations that can propagate through the spacecraft structure and degrade the performance of precision instruments such as optical systems and interferometers. Jitter can originate from internal sources, such as reaction wheels, momentum wheels, and cryocoolers, or external sources like thermal distortions.

For example, as discussed in [21], even minor thermal distortions in large space structures can cause microvibrations that affect alignment. These thermally induced vibrations, often referred to as thermoelastic jitter, occur when components of the spacecraft experience uneven thermal expansion or contraction due to differential heating from solar radiation. Over time, these small deformations can propagate through the spacecraft, causing disturbances that degrade instrument pointing accuracy or lead to wavefront errors in optical systems. Jitter is particularly concerning for instruments requiring high pointing accuracy, such as space telescopes, where even micrometer-level displacements can significantly degrade image quality. According to [15], minimizing jitter is crucial for maintaining the alignment of optical paths in space-based interferometers.

Strategies to mitigate jitter include:

Vibration isolation systems: Isolation mounts can decouple sensitive instruments from mechanical components, reducing the propagation of microvibrations. For example, passive vibration isolation systems using viscoelastic materials can be applied to dampen vibrations.

Active vibration control: Active systems such as piezoelectric actuators can be used to counteract vibrations in real time by generating compensatory forces.

Cryocooler isolation: Since cryocoolers often produce significant vibrations due to moving parts, they are isolated from sensitive instruments using vibration isolators and dampers.

Reaction wheels and momentum wheels are other major sources of jitter in spacecraft. These wheels are used for attitude control but can introduce vibrations due to imbalances or spinning at high speeds. This problem is especially acute in missions like exoplanet observation, where even tiny deviations in pointing can disrupt data collection. The Fourier Kelvin Stellar Interferometer (FKSI) mission [6] identified reaction wheel-induced jitter as a key risk factor, prompting the development of advanced isolation systems to reduce vibration transmission.

Lastly, residual strain energy from the deployment of large structures, such as booms or antennas, can lead to microlurching. After the primary vibration has subsided, small shifts in the structure caused by residual stresses can lead to position changes, which can affect spacecraft orientation or the positioning of solar arrays [23]. This effect is of particular concern for flexible appendages that are not rigidly supported during deployment.

3.3. Heat Shielding and Thermal Control

Thermal control is essential for maintaining the performance, structural integrity, and alignment of space-based instruments, particularly in environments like Lagrange Point 2 (L2). Spacecraft at L2 are exposed to constant solar radiation without the protection of Earth's atmosphere, creating unique thermal challenges. Effective thermal control systems must be designed to prevent uneven heating and maintain stable operating temperatures for sensitive components such as deployable optics, booms, and sensors.

3.3.1. Thermal Expansion and Contraction

One of the most critical thermal challenges is the expansion and contraction of materials in response to temperature fluctuations. Even small temperature changes can cause components to expand or contract, affecting the structural integrity and alignment of critical optical instruments. This is especially significant at L2, where spacecraft are continuously exposed to sunlight, creating thermal gradients between the sun-facing and shaded components.

The thermal expansion of a material can be quantified by the equation:

$$\Delta L = \alpha L_0 \Delta T \quad (3.16)$$

where: ΔL is the change in length, α is the coefficient of thermal expansion (CTE) of the material, L_0 is the original length of the material, and ΔT is the temperature change.

For spacecraft with deployable structures such as booms and solar panels, uneven heating can induce thermal stresses that lead to warping, bending, or even failure. The materials used must have low coefficients of thermal expansion (CTE) to minimize the effects of temperature changes. Composite materials such as carbon fiber reinforced polymers (CFRPs) are widely

used due to their high strength-to-weight ratio and low thermal expansion properties [19].

In high-precision systems, such as space-based interferometers, thermal expansion can introduce errors in the alignment of the optical path, which would directly impact the quality of observations. Therefore, selecting materials with appropriate thermal properties is crucial to ensure that the system remains within acceptable deformation limits throughout the mission.

3.3.2. Thermal Mechanical Effects

Thermal mechanical effects, including thermoelastic deformation and thermoelastic vibrations, arise when temperature changes induce mechanical stresses within the spacecraft's structure. These effects are particularly relevant when components made from different materials, with varying thermal expansion properties, are exposed to uneven heating. The resulting internal stresses can be modeled using the thermoelastic stress equation:

$$\sigma_{\text{thermal}} = E\alpha\Delta T \quad (3.17)$$

where: σ_{thermal} is the thermally induced stress, E is the modulus of elasticity (Young's modulus) of the material, α is the coefficient of thermal expansion, ΔT is the temperature change.

These internal stresses can lead to deformations, oscillations, and even structural failure if not properly managed [21]. Thermally induced vibrations, or thermally induced jitter, are especially problematic for spacecraft with sensitive optical instruments or large deployable structures. These vibrations can be triggered when thermal deformation interacts with the natural frequencies of the structure, potentially exciting resonant modes. This phenomenon, known as thermal flutter, can cause structural instability, misalignment, and performance degradation [15].

At L2, although the spacecraft is not subjected to drastic temperature variations like those experienced in low Earth orbit, it is still exposed to significant thermal gradients across its large structures. The long-term exposure to solar radiation at L2 necessitates efficient thermal management systems that mitigate these thermal gradients and ensure uniform temperature distribution across the spacecraft.

3.3.3. Thermal Flutter and Jitter

Thermal flutter and jitter are critical issues in spacecraft equipped with flexible structures. Thermal flutter results from cyclic thermal warping due to uneven exposure to solar flux. This phenomenon excites vibration modes in flexible structures, potentially leading to significant performance degradation. Similar issues were observed in the Hubble Space Telescope, where rapid temperature changes caused thermal warping, which introduced wavefront jitter and misalignment of the optical systems [15].

At L2, while there are no day-night cycles, constant solar exposure demands careful control of temperature gradients, as fluctuations could still induce unwanted vibrations, particularly in structures with low eigenfrequencies, such as deployable booms and solar arrays [15]. Addressing thermal flutter and jitter is essential for maintaining the stability and precision of space-based optical instruments.

3.3.4. Thermal Shields and Control Systems

To mitigate the effects of thermal expansion, mechanical stresses, and thermal flutter, spacecraft require robust thermal management systems that include both passive and active components.

Passive Thermal Control Passive thermal control provides the first line of defense against thermal challenges. Thermal shields, radiative surfaces, and multi-layer insulation (MLI) are commonly used to reduce the heat flux absorbed by sun-facing components and maintain a more uniform temperature distribution across the spacecraft.

A key property of materials used in thermal shields is emissivity, which determines how effectively a surface radiates absorbed heat. The radiative heat transfer can be expressed as:

$$Q_{\text{rad}} = \epsilon \sigma A T^4 \quad (3.18)$$

where: Q_{rad} is the radiative heat transfer, ϵ is the emissivity of the material, σ is the Stefan-Boltzmann constant, A is the area of the radiating surface, T is the temperature of the surface.

Radiative surfaces with high emissivity, such as certain metallic coatings, are used to help dissipate heat. For components that need to stay cooler, low-emissivity materials such as MLI are used to reflect incoming radiation and prevent excessive heat absorption.

Material properties important for passive thermal control include:

- Thermal conductivity: High thermal conductivity materials help to spread heat evenly, reducing thermal gradients. Metals such as aluminum and copper are often used due to their excellent thermal conductivity.
- Emissivity and absorptivity: The balance between these two properties determines how a material responds to radiative heat. Low-emissivity materials, like polished metals, reflect radiation, while high-emissivity materials help radiate heat away.
- Low CTE materials: Materials with low coefficients of thermal expansion, like carbon composites, minimize expansion and contraction due to thermal loading, reducing stress in deployable structures.

Active Thermal Control Active thermal control systems, such as onboard heaters and heat pipes, are often employed to manage temperature variations more precisely. Heat pipes are particularly effective in redistributing heat across the spacecraft by transferring thermal energy through phase changes in a working fluid.

Active systems help maintain consistent operating temperatures by redistributing heat throughout the spacecraft, especially in regions that are not exposed to direct sunlight. However, active systems increase power consumption and add complexity to the thermal management system, requiring careful integration into the overall mission design.

3.4. Large Deployable Space Structures

To develop a high-performing space-based interferometer, it is crucial to examine the mechanical and thermal design solutions used in other large space missions. In this section, we will discuss several space structures that demonstrate advanced deployable systems, with a particular focus on the James Webb Space Telescope (JWST). These missions offer valuable insights into the mechanical design of large structures, damping of mechanical and thermal vibrations, and strategies for both passive and active thermal control. The Fourier-Kelvin Stellar Interferometer (FKSI), and the International Space Station (ISS) will also be explored for their innovative approaches to deploying booms, sunshields, and other critical components. By studying the design and deployment strategies of these large space structures, we can better understand how to achieve precise control, stability, and thermal management, all while ensuring the components are stowed efficiently and deployed accurately in space. These lessons will guide the mechanical design and deployment strategies of the deployable systems discussed in this thesis.

3.4.1. The James Webb Space Telescope (JWST)

The James Webb Space Telescope (JWST) is a highly advanced infrared observatory designed to investigate key astrophysical phenomena, such as the formation of the first galaxies and the atmospheres of exoplanets. JWST is a significant successor to the Hubble Space Telescope, designed with a deployable 6.6-meter primary mirror and stationed at the Sun-Earth second Lagrange point (L2), which provides a stable thermal environment ideal for infrared observations. The mission's primary science goals include the study of galaxy formation, stellar birth, and exoplanet atmospheres, all of which require precision thermal control and mechanical stability [12].

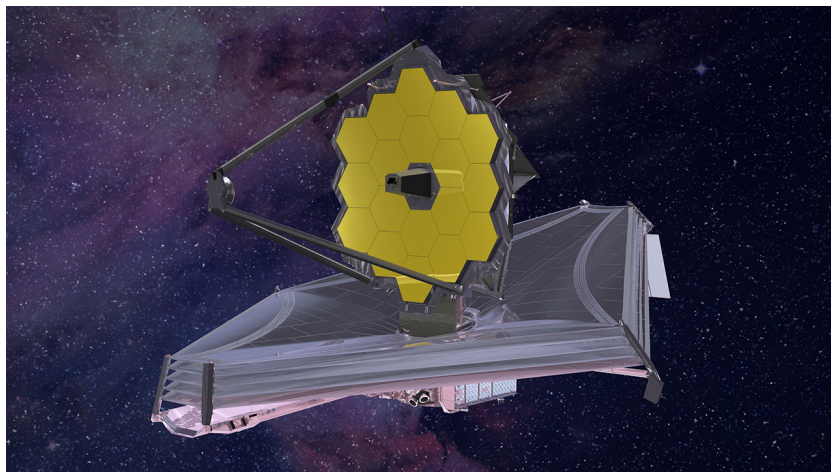


Figure 3.1: JWST artist impression[14]

The JWST's location at L2 and its mission aspects closely align with the goals of this thesis, which focuses on the high-level mechanical design of a spacecraft utilizing infrared nulling interferometry at L2 to detect and characterize exoplanets. Both spacecraft designs face the challenge of maintaining precise thermal control to prevent optical distortions while ensuring that the deployment of large structures, such as sunshields or booms, being stowed within the mechanical constraints imposed by launch vehicles like the Ariane 6.

3.4.1.1. JWST Thermal Design and Challenges

Operating in the infrared spectrum, the James Webb Space Telescope (JWST) is highly sensitive to thermal radiation, necessitating careful design to maintain cryogenic temperatures below 55 K for its Optical Telescope Element (OTE) and science instruments[12]. The spacecraft uses a five-layer sunshield, deployed to block sunlight and reduce heat flux, ensuring that the telescope and instruments remain passively cooled. This passive cooling system is critical, as any excess thermal radiation could compromise the accuracy of the telescope's infrared observations.

Sunshield Design: The JWST sunshield is approximately the size of a tennis court (21.197 m x 14.162 m), designed to keep the telescope in permanent shadow from the Sun, Earth, and Moon. This shadowing is essential for achieving the necessary cryogenic conditions without active cooling systems. The five-layer sunshield is made from Kapton E, chosen for its thermal stability and low mass. The outermost layer (Layer 1), facing the Sun, is coated with a silicon layer to modulate temperatures and ensure long-term durability, while the back side is coated with vapor-deposited aluminum (VDA) to reflect heat. Layers 2 to 5 are progressively thinner and reflect less solar energy as they approach the telescope. The first layer can reach temperatures as high as 400 K, while the coldest layers near the OTE are below 100 K. This multi-layer design reduces the thermal radiation from 218,000 W on the sun-facing side to less than 100 W reaching the cold side, allowing the telescope to maintain an operating temperature below 55 K [12]. The overall size of the sunshield, 21 m by 15 m, was determined by the need to fully shadow the OTE and Integrated Science Instrument Module (ISIM), ensuring passive cooling and meeting the radiometric sensitivity and stray-light requirements. The size also allows the telescope to maintain a wide operational field of regard, which required the sunshield to block sunlight while the telescope slews across the sky. These dimensions were constrained by the need to fit within the launch vehicle's fairing, requiring a folding and deployment mechanism. The thickness of each layer was optimized through computer models that tested configurations ranging from 2 to 7 layers, ultimately selecting the five-layer design as the best trade-off between thermal performance and weight savings. Thicker layers were avoided because they would conduct more heat, which would defeat the goal of thermal isolation. Instead, the thin layers separated by vacuum spaces minimize heat transfer. Each membrane has an embedded catenary to ensure structural integrity and tension, and the edges of the layers are corrugated to prevent buckling during deployment.

Challenges in Deployment: The sunshield's deployment sequence is one of the most complex ever attempted in space. After launch, it unfolds in multiple stages, with telescoping booms and tensioning cables pulling the five layers into place. Over 107 release mechanisms are actuated during deployment, ensuring that the layers do not tear or snag. This deployment is critical to ensuring the sunshield's functionality, as any snagging or damage could compromise the thermal isolation of the telescope [12].

Active Cooling for MIRI: While passive cooling suffices for most of JWST's instruments, the Mid-Infrared Instrument (MIRI) requires a much lower operating temperature of around 6.4 K. This is achieved using a cryocooler that operates via a two-stage process, utilizing a Pulse Tube (PT) pre-cooler and a Joule-Thomson (JT) stage. The cryocooler provides a cooling

power of approximately 119 mW at 6.4 K, which is close to the predicted value of 124 mW before launch. Keeping MIRI at these extreme temperatures is essential to avoid interference from its own infrared emission [12].

Thermal Control for Science Instruments: In addition to the sunshield, JWST's thermal architecture includes radiators to manage heat dissipation from sensitive components. The radiators, located on the Integrated Science Instrument Module (ISIM), provide passive cooling to instruments like the Near-Infrared Camera (NIRCam) and Near-Infrared Spectrometer (NIRSpec). These instruments require temperatures between 35-45 K for optimal performance. High-purity copper heat straps transport heat away from the detectors to the radiators, ensuring efficient thermal dissipation. The radiators are sized to cover approximately 16 square meters, allowing them to reject 400-500 milliwatts of heat. This sizing was chosen based on the cooling needs of the instruments and the available space on the spacecraft, and was validated through extensive pre-launch thermal modeling. The radiators were positioned at the rear and top sides of the spacecraft to optimize their exposure to cold space, ensuring effective heat emission. The radiators are made from high-purity aluminum subpanels coated with Z307, a high-emissivity material with an emissivity of around 0.95 to 0.98, which maximizes heat dissipation efficiency in the vacuum of space. This design provides a cooling margin of over 80%, ensuring that the instruments remain at their required operational temperatures [22].

Parasitic Heat Management: Minimizing parasitic heat loads is critical for maintaining low temperatures on the cold side. These heat loads arise from electronic systems, cabling, and the spacecraft bus on the hot side. JWST employs thermal isolation techniques, such as multi-layer insulation (MLI) blankets and careful routing of cables, to minimize conductive heat transfer. Pre-launch modeling predicted a safety margin of 80% for the cryogenic radiators, ensuring that parasitic heat would not compromise the telescope's thermal performance [12].

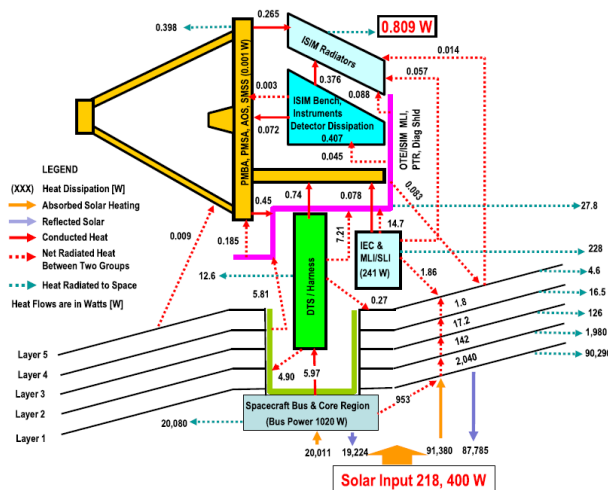


Figure 3.2: JWST Observatory-level heat flow diagram [12].

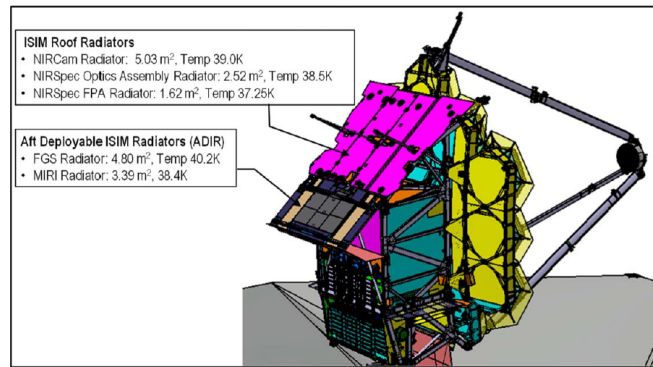


Figure 3.3: JWST ISIM cryogenic radiator configuration [12].

3.4.1.2. Vibration Management and Line-of-Sight Stability

Vibration management is a critical aspect of JWST's design, particularly with regard to ensuring the Line-of-Sight (LOS) stability required for precision imaging. The highly sensitive instruments onboard JWST, such as the Near-Infrared Camera (NIRCam) and the Mid-Infrared Instrument (MIRI), require an extremely stable platform, with LOS jitter controlled to within 1–2 milliarcseconds (mas)[12]. Even small disturbances can introduce optical distortions that degrade image quality and spectroscopic performance.

Sources of Vibration: Jitter, or small vibrations, can be induced by various spacecraft components, with the most significant contributors being the Reaction Wheel Assemblies (RWAs), the MIRI cryocooler, and other onboard mechanisms. These components generate vibrations in the 10-100 Hz frequency range, which could propagate through the spacecraft's structure and disturb the Optical Telescope Element (OTE) if left unchecked.

Isolation Techniques and the Isolator Assembly (IA): To mitigate these vibrations, JWST employs passive isolation techniques to decouple the OTE from vibration-inducing components. The primary isolation mechanism is the 1 Hz Isolator Assembly (IA), which connects the OTE to the spacecraft bus. The IA introduces a low-frequency "bounce mode" at 1 Hz, effectively preventing higher-frequency vibrations from reaching the telescope. This soft suspension system ensures that vibrations above 1 Hz are largely absorbed before propagating to the telescope. The IA consists of four composite fiber tubes arranged in an "X" pattern, supporting the OTE while allowing it to oscillate at low frequencies relative to the spacecraft. During launch, the IA is locked to prevent damage from ground loads, but once in orbit, it is released to operate as a soft isolation system. This design helps maintain the required 1-2 mas LOS stability.

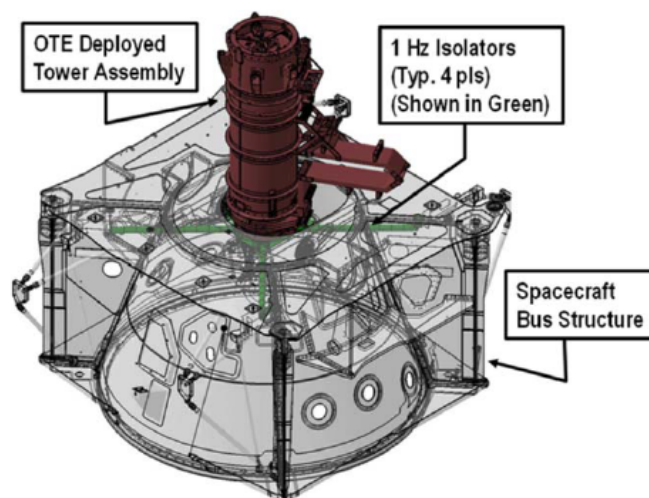


Figure 3.4: JWST isolator assembly [12].

Reaction Wheel Isolator Assembly (RWIA): The Reaction Wheel Isolator Assembly (RWIA), designed by Northrop Grumman, provides passive isolation for the spacecraft's reaction wheels, which are used for attitude control. Reaction wheels are significant sources of vibration due to their high rotational speeds. The RWIA uses soft spring dampers to isolate the vibrations from reaching the OTE, further enhancing LOS stability.

Magnetic Tuned Mass Dampers (MTMDs): JWST also utilizes Magnetic Tuned Mass Dampers (MTMDs) on the Sunshield Membrane Support Structure (SMSS) to control vibrations. MTMDs consist of masses tuned to the resonant frequency of the SMSS (3-6 Hz), counteracting vibrations by moving out of phase with the structure's oscillations. This damping effect minimizes any disturbances that could affect LOS stability.

Cryocooler Jitter Attenuation: The MIRI cryocooler, which operates between 29.5 and 31.5 Hz, also contributes to jitter. JWST addresses this through the Cryocooler Jitter Attenuation Assembly (CJAA), which uses preloaded Vectran support cords and a rigid mass to isolate vibrations at around 30 Hz, ensuring that the cryocooler's operation does not disrupt the telescope's performance.

3.4.1.3. Deployment Systems and Lessons Learned

One of the most challenging aspects of the JWST's mechanical design was the deployment of its large sunshield and primary mirror, both of which had to be folded for launch and then deployed once the spacecraft reached its operational orbit at L2. The successful deployment of these critical components relied on complex mechanisms, including several hundred launch-release mechanisms (LRMs) and a series of motor-driven actuators to unfold and tension the sunshield layers. The precision required in these deployments highlights the complexity involved in ensuring that large, flexible structures can be accurately deployed in space without interference or snagging [12].

The experience gained from JWST's deployment mechanisms provides important insights into the design and deployment strategy for the nulling interferometer's booms and sunshields.

Like JWST, the spacecraft in this thesis will rely on deployable structures that must fit within the constraints of the Ariane 6 launch vehicle and deploy reliably in space. The analysis of JWST's deployment mechanisms and isolation strategies offers valuable lessons for mitigating risks associated with the deployment and operation of large, flexible components in space environments.

3.4.2. Fourier Kelvin Stellar Interferometer (FKSI)

The Fourier-Kelvin Stellar Interferometer (FKSI) was a proposed mission concept for an imaging and nulling interferometer designed to operate in the mid-infrared spectral region (3–8 microns). Although FKSI never progressed beyond the design phase, its detailed mission studies provide valuable insights into the challenges and solutions associated with space-based interferometry [7]. As a structurally connected system with a 12.5-meter baseline, FKSI's conceptual design offers important lessons for future missions aiming to detect and characterize exoplanets and debris disks.

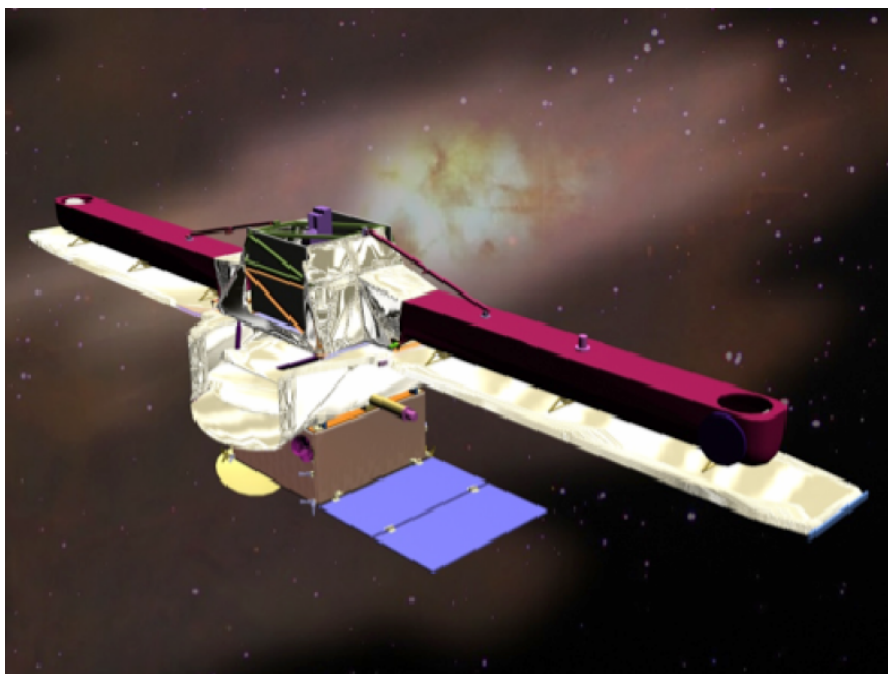


Figure 3.5: Artist's concept of FKSI prototype [6]

In this section, the mechanical and thermal design challenges that were analyzed during FKSI's development will be examined. These include the proposed boom deployment mechanisms, which were designed to maintain a stable baseline, and the use of composite materials that were optimized for low mass and high strength [2]. The boom also supported fixed sunshades, which played an important role in maintaining the passive cooling system, contributing to the structural stability and the reduction of thermal noise from the telescope itself. While FKSI was never built, the design studies on its passive cooling systems and cryogenic operations offer critical insights into thermal management strategies for future missions, especially those operating at L2 [6]. Additionally, the lessons learned from the precision alignment systems FKSI would have required to ensure stability and accuracy in a harsh space environment will be explored, as well as the cost and design trade-offs identified during the research phase.

3.4.2.1. Composite Materials and Structural Design

The deployment of the 12.5-meter boom in the Fourier-Kelvin Stellar Interferometer (FKSI) mission concept was a key structural challenge. The boom was designed to support the siderostat mirrors with 0.5 meter apertures at the ends, creating a stable baseline for interferometry. To meet the mission's requirements for a lightweight and thermally stable structure, the design utilized composite materials [7]. While the specific composite materials are not directly mentioned in [7], it is clear that the boom was designed to balance strength, weight, and stability, typical of advanced composite structures used in space applications.

Material Properties The selected composite material for the boom would have been optimized to meet several crucial design criteria:

- **Lightweight Design:** Minimizing the mass of the boom was essential to reduce launch costs and payload limitations. The use of composite materials provided the necessary structural strength while keeping the mass low.
- **Thermal Stability:** A key challenge for FKSI's boom was to maintain the precise baseline required for interferometry in the cryogenic environment. The composite material likely had a low coefficient of thermal expansion, which ensured minimal dimensional changes despite temperature fluctuations. This was important for maintaining alignment during operations at temperatures around 60 K [6].
- **Structural Integrity:** The boom had to support the mirrors and sunshades without flexing or bending. The composite material's high stiffness helped maintain structural integrity, ensuring that the baseline remained stable throughout the mission [7].

Deployment Mechanism and Design Considerations The boom deployment relied on MILSTAR hinge technology, which had been proven in previous space missions [2]. This technology allowed the boom to be stowed compactly during launch and then deployed in space to its full operational length. The simplicity of the hinge system reduced the mechanical complexity of the deployment, which minimized potential points of failure. The boom also supported fixed sunshades, which played an important role in maintaining the passive cooling system. By shading the structure from solar radiation, these sunshades helped keep the boom and optical instruments at cryogenic temperatures necessary for mid-infrared observations, as well as reducing the thermal noise emitted by the telescope [6].

3.4.2.2. Vibration Control and Fine-Pointing Mechanisms

Maintaining precise alignment between the siderostat mirrors of the Fourier-Kelvin Stellar Interferometer (FKSI) was critical for ensuring the success of its nulling interferometry. Any disturbances or misalignments in the optical path could degrade the system's ability to achieve the necessary contrast for detecting exoplanets and other faint astronomical signals. To address this, FKSI's design incorporated several strategies to manage vibrations and fine-pointing adjustments, both of which were essential for maintaining the accuracy of the optical path [6].

Vibration Control and Reaction Wheel Disturbances One of the primary sources of disturbance in the FKSI system was the spacecraft's reaction wheels, which are typically used for attitude control and maintaining orientation in space. These reaction wheels can introduce

vibrations into the spacecraft structure, which can propagate through the boom and cause misalignments between the mirrors. FKSI's design accounted for this by allocating a specific jitter tolerance for the system. Modeling studies showed that reaction wheel-induced vibrations needed to be kept below 6 nanometers (nm) of jitter in the optical path delay (OPD) to avoid negatively affecting the null depth of the interferometer. This tolerance was designed to ensure that even with high-frequency jitter from the reaction wheels, the overall stability of the optical system would not be compromised [2]. Additionally, the boom's fundamental vibrational modes were identified at 5.6 Hz and 7.3 Hz. These resonant frequencies were important to control, as they could lead to large-scale oscillations if triggered. The boom structure, made of composite materials, was designed to be stiff enough to minimize deflections at these frequencies, preventing them from propagating through the interferometer and disrupting the alignment of the optical path. A significant safety margin of 9.4 nm was incorporated into the vibration control strategy to account for other potential sources of noise or disturbances within the system [6]. This margin ensured that even in the presence of multiple vibration sources, the system could maintain its required precision.

Fine-Pointing Mechanisms for Precision Alignment In addition to controlling vibrations, FKSI's design included several fine-pointing mechanisms that allowed for real-time adjustments to the alignment of the mirrors. These mechanisms were essential for correcting any minor drifts or misalignments that could occur over time due to thermal effects, structural deformations, or external disturbances. The system included fast steering mirrors as part of the optical bench assembly. These mirrors were capable of making precise, small adjustments to the direction of the incoming light beams, ensuring that the optical path remained aligned. The steering mirrors worked in conjunction with the angle tracker assembly, which provided continuous feedback on the exact angles of the incoming light [7]. This feedback was used to adjust the mirrors and correct for any misalignments that could arise during the mission. The fringe tracker system played a critical role in maintaining the correct phase relationship between the light beams from the two telescopes. Any phase differences due to path length discrepancies could degrade the nulling performance of the interferometer. The fringe tracker continuously monitored the phase of the light and adjusted the optical delay lines (ODLs) to ensure that the beams remained in phase. These ODLs provided fine adjustments to the optical path lengths, compensating for any misalignments or disturbances [6].

Integrated Vibration Control and Pointing Strategy The combination of vibration control and fine-pointing mechanisms created a robust system for maintaining the alignment and precision required by FKSI's nulling interferometer. The vibration control strategy focused on minimizing the impact of reaction wheel disturbances and other structural vibrations, while the fine-pointing mechanisms provided real-time corrections to ensure that the mirrors and optical path remained stable. The closed-loop system of active control, including the fringe tracker, ODLs, and fast steering mirrors, allowed FKSI to achieve and maintain the precise alignment needed for high-contrast interferometric observations. This system was validated through modeling and simulation studies, which confirmed that the combined vibration control and pointing mechanisms would meet the stringent requirements for interferometric accuracy, even under the influence of spacecraft-induced disturbances [2]. Overall, the vibration control and fine-pointing mechanisms in FKSI were essential for ensuring the stability and alignment

of the optical system, allowing the mission to achieve the precision required for detecting faint exoplanetary signals and studying debris disks. These strategies provide valuable lessons for future space-based interferometers, where managing both vibrations and fine-pointing is critical to maintaining the performance of large deployable optical systems.

3.4.2.3. Passive Cooling Systems and Cryogenic Operations

The Fourier-Kelvin Stellar Interferometer (FKSI) was designed to operate in the mid-infrared spectral range, which required extremely low operational temperatures to minimize thermal noise and ensure optimal performance of the instruments. The mission relied on a passive cooling system to achieve cryogenic temperatures of approximately 60 K. This low temperature was critical to maintaining a zodiacal-background-limited sensitivity, rather than being dominated by the telescope's own thermal emissions [7, 2].

Sunshades for Passive Cooling One of the primary methods for maintaining the cryogenic environment in FKSI was the use of fixed sunshades, which were integrated with the boom structure. These sunshades played a crucial role in shielding the optical instruments and the boom from solar radiation. By blocking direct sunlight, the sunshades allowed the spacecraft to cool passively to cryogenic temperatures without the need for active cooling systems, such as cryocoolers, which would have added significant complexity, mass, and energy demands to the mission. The passive cooling system was designed to maintain a stable temperature of around 60 K, ensuring that the thermal emissions from the telescope itself were low enough to allow FKSI's instruments to detect faint exoplanetary signals. In particular, operating at this temperature helped reduce the background thermal noise in the mid-infrared range, which is crucial for achieving high-contrast observations in interferometry [6].

Thermal Stability and Structural Integrity Maintaining thermal stability was vital for ensuring the structural integrity of the boom and the precision alignment of the siderostat mirrors. Temperature fluctuations in space can cause materials to expand or contract, potentially leading to misalignments in the optical path. The sunshades not only provided passive cooling but also contributed to the overall thermal stability of the interferometer. By keeping the boom and mirrors at a constant low temperature, the design helped prevent thermal distortions that could degrade the performance of the nulling interferometer. The choice of materials for the boom, likely a composite with low thermal expansion coefficients, complemented the passive cooling strategy by further minimizing thermal deformations. Together, these design elements ensured that FKSI's optical system could maintain the necessary stability and alignment, even in the fluctuating thermal environment of space [7, 2].

Advantages of Passive Cooling The decision to use passive cooling over more complex active cooling methods was driven by several key advantages:

- **Simplicity and Reliability:** Passive cooling systems are inherently simpler and more reliable than active systems, which involve moving parts, mechanical systems, and energy consumption. This simplicity reduced the overall mission risk by lowering the number of potential failure points [6].
- **Lower Mass and Power Requirements:** By avoiding active cryocoolers, FKSI's passive cooling system allowed the spacecraft to maintain a lower overall mass and reduced

the power requirements. This was a significant advantage given the limited payload capacity and energy constraints of space missions [2].

- **Long-Term Stability:** Passive systems provide long-term stability without the need for consumables (such as liquid helium) or continuous power, making them ideal for a mission like FKSI, which was designed to operate for extended periods in deep space [6].

Thermal Management in the Space Environment In addition to the sunshades, the thermal design of FKSI accounted for the harsh temperature fluctuations in space. The spacecraft's orbit and exposure to solar radiation meant that temperature gradients could develop between different parts of the structure. The passive cooling system, combined with the thermal properties of the composite boom materials, helped mitigate these effects by ensuring a more uniform temperature distribution across the structure [7]. The success of the mission depended on maintaining cryogenic temperatures for both the optics and the spacecraft's thermal shields. Without effective thermal control, the background thermal radiation would have overwhelmed the signal from distant exoplanets, making it impossible to achieve the mission's scientific goals [6].

Lessons for Future Missions The passive cooling system designed for FKSI provides valuable lessons for future space-based interferometers and missions that operate in the mid-infrared range. Passive cooling offers a low-risk, cost-effective solution for achieving the cryogenic temperatures needed for high-precision observations without the added complexity of active cooling systems. The use of sunshades and materials with low thermal expansion coefficients can ensure both thermal stability and structural integrity over long mission durations. These insights are particularly relevant for future interferometric missions that need to operate in environments like L2, where maintaining stable, low temperatures is critical to minimizing noise and ensuring accurate data collection. By incorporating passive cooling strategies and thermally stable materials, future missions can reduce both cost and risk while achieving the precision needed for advanced astronomical observations [2, 6].

4

System Constraints

Building on the theoretical foundations and mission precedents discussed in Chapter 3, this chapter defines the system constraints that govern the mechanical and thermal design of the nulling interferometer spacecraft. These constraints are derived from both fundamental structural principles and the practical lessons learned from missions such as JWST and FKSII. They include requirements for maintaining structural stability, ensuring thermal control at L2, and preserving optical alignment within tight tolerances. Together, they define the critical parameters for the deployable elements of the system, enabling compact stowage and precise performance post-deployment.

The Ariane 6 long fairing provides an internal payload volume of approximately 259.15 cubic meters. However, this value does not directly translate to usable spacecraft volume. Fully utilizing this space would require a perfectly efficient layout without packing losses. In practice, the design is limited by the fairing's maximum dimensions along each axis. These axis-specific constraints influence the layout and integration of major components such as telescope apertures, the beam combiner, spacecraft bus, solar panels, and radiators. As shown by the JWST and FKSII missions, the choice of spacecraft topology—Linear or X-array—also significantly affects stowage efficiency and deployment strategy.

Ultimately, both topologies must fit within the fairing while ensuring integration of all essential systems. These geometric and volumetric constraints are central to evaluating whether a given architecture can be feasibly stowed and deployed using Ariane 6.

4.1. Predefined Dimensional Constraints

The design must comply with predefined physical constraints imposed by the Ariane 6 fairing and other mission-level requirements. This section outlines dimensional parameters that are considered fixed or predetermined in the context of this thesis. These serve as key design inputs and boundary conditions for the mechanical layout.

- **Ariane 6 Fairing Dimensions:** The long fairing configuration of Ariane 6 provides a total internal height of 18 meters and a maximum internal diameter of 4.6 meters. At a height of 11.185 meters, the fairing begins to taper conically, imposing additional spatial con-

straints on components stowed above this point. This tapering critically influences the layout of deployable structures and large components. The launch vehicle also imposes dynamic constraints, requiring a minimum fundamental frequency of 6 Hz in the lateral direction and 20 Hz in the longitudinal direction.

- **Telescope Aperture Size** D_{aperture} : Drawing inspiration from the Herschel Space Observatory's primary mirror, the proposed design features an aperture diameter in the range of 2 to 3 meters. For the purposes of this thesis, an aperture diameter of 2.5 meters is adopted for all analyses. The telescope is expected to use an off-axis Three-Mirror Anastigmat (TMA) configuration, which offers a compact layout with high optical performance in terms of light collection and image quality.
- **Baseline Length** L_{baseline} : This thesis considers a broad range of baseline lengths from 8 to 32 meters to evaluate different performance configurations. While longer baselines improve angular resolution, they require more complex deployment mechanisms and occupy more volume in the stowed configuration. Additionally, increased stiffness is necessary to minimize structural deformations, in accordance with the axial deformation behavior described by Equation (3.10).

4.2. Large Components

The components in this section are not fixed in size but play a major role in spacecraft geometry and must be evaluated carefully during design.

- **Spacecraft Boom Structure**: The boom structure, essential for achieving the interferometric baseline, is one of the primary drivers of spacecraft volume. Its stowed length must fit within the Ariane 6 fairing, while allowing deployment to lengths of 8 to 32 meters depending on the selected topology. The structural design—including joint mechanisms and nesting behavior—determines how compactly the booms can stow, which directly affects fairing utilization.
- **Spacecraft Bus**: Serving as the central hub for avionics, propulsion, and power systems, the spacecraft bus must remain within the fairing's lateral dimensions while providing reliable support for all mounted and deployable components. Its integration strategy is essential for maintaining internal clearances and avoiding overlap with adjacent systems such as radiators or booms.
- **Beam Combiner**: As the optical heart of the interferometer, the beam combiner coherently merges light from the four telescopes. Due to its central placement and multiple optical interfaces, it is expected to be one of the larger components. Its final shape and dimensions are still under evaluation and must strike a balance between optical path accuracy and compact integration.
- **Sunshield**: The sunshield must fold efficiently into the stowed configuration and expand to provide sufficient thermal protection in orbit. Its deployed size depends on the field of regard of the apertures and the need to block solar and planetary radiation across all pointing angles. This may result in a larger deployed area, especially if the apertures require wide slewing capabilities. Compact folding, structural integrity, and deployment reliability are critical design factors.

- **Solar Panels:** Designed to fold during launch and expand in orbit, solar panels must meet power requirements while conforming to the fairing's spatial envelope in the stowed configuration. Their positioning must account for clearance from adjacent structures during both stowage and deployment.
- **Damping Mechanisms:** Inspired by JWST's 1 Hz Isolator Assembly (Section 3.4.1), a functionally similar isolator will be incorporated between the spacecraft bus and the deployable boom structure to prevent higher-frequency vibrations from reaching the telescopes.

4.3. Optical and Structural Alignment Constraints

The performance of a nulling interferometer hinges on maintaining sub-microradian optical alignment, which requires a structurally stable spacecraft that can mitigate dynamic and thermal disturbances at L2. These disturbances can cause vibrations and deformations with uncertain amplitudes and frequencies. The spacecraft must be designed to minimize such effects before they propagate into the optical system.

- **Pointing Stability and Jitter** δ_{pointing} : FKSI targeted pointing stability within 1–2 milliarc-seconds (mas), with sub-nanometer delay line and wavefront control. These tolerances are adopted here and must be supported by structural damping and isolation. FSM capabilities (0.5–50 μrad RMS) require residual jitter to remain below their control threshold, as discussed in Section 3.2.
- **Vibrational Response** f_n : The fundamental frequency of structural elements must avoid overlap with dominant disturbance sources. The relevant natural frequency is given by Equation (3.12), and is influenced by both stiffness and mass. To remain decoupled from the isolator's 1 Hz mode, the spacecraft structure will be sized for a first natural frequency of at least 2 Hz. This 2 Hz target is the principal sizing driver for the structural design.
- **Stiffness and Damping Properties** Stiffness plays a critical role in resisting deformation. Materials with high E and optimized cross-sections A are selected to maintain optical alignment. Damping properties influence the dynamic amplification factor described in Equation (3.15).

4.4. Thermal Constraints

Operating in the L2 thermal environment enables passive cryogenic cooling, which is essential for infrared observations, but also imposes strict thermal control challenges. Although this thesis does not perform detailed thermal modeling, the required deployment space and volume for the sunshield are factored into the mechanical design. Thermal considerations also influence material selection for structural components.

- **Temperature Stability** ΔT : The spacecraft must remain below 55 K to ensure detector sensitivity, as demonstrated by the JWST. A multilayer sunshield, intended to limit radiative loading to under 100 W, will provide passive cooling. While thermal behavior is not analyzed in this thesis, the sunshield's required stowage and deployment volume is included in the design strategy.

- **Thermal Expansion** ΔL : To minimize differential expansion across components, materials with low coefficients of thermal expansion, such as carbon fiber composites, will be used—especially in the booms where alignment stability is paramount.
- **Thermally Induced Stress** σ_{thermal} : Although thermal stresses are not simulated in detail, they are considered in the material trade-off. Passive thermal control and careful material selection reduce the risk of stress-related misalignments over time.

4.5. Additional Constraints

In addition to dimensional, thermal, and optical constraints, the spacecraft design is further governed by mass and mechanical stability requirements.

- **Mass Constraints** m_{total} : The combined mass of all structural and deployable components must remain below 11,500 kg, consistent with Ariane 6 specifications. This requirement guides the use of high-strength, low-mass composites in the boom and sunshield systems.
- **Buckling Resistance** P_{cr} : Lightweight boom structures must resist buckling under compressive loads during launch and deployment. Structural stability will be ensured through geometric reinforcement and material selection consistent with Euler buckling theory (3.11).

The system constraints defined in this chapter provide the structural, thermal, and optical boundaries for the mechanical design explored in the following chapters. They are grounded in physical principles, informed by past missions, and tailored to ensure compatibility with Ariane 6 stowage and deployment conditions.

5

Boom Structure Design Trade-off

This chapter builds on the findings of the previous chapters by integrating mechanical and thermal considerations into a cohesive design trade-off that supports the mission's volumetric and optical requirements. The design and sizing of the boom structure are critical to the feasibility and success of the nulling interferometer. These booms must extend to precise lengths in orbit while maintaining the strict alignment tolerances essential for optical performance. Simultaneously, they must stow compactly within the limited payload volume of the Ariane 6 launch vehicle, ensuring that all other large components also fit without interfering with one another.

5.1. Challenges in Deployable Boom Design

Deployable booms face multiple challenges throughout their lifecycle, from launch dynamics to the operational environment at the L2 orbit. During launch, the booms must endure compressive and vibrational forces without compromising their structural integrity. Post-launch, they must deploy accurately and reliably to achieve the baseline distances and alignment required for interferometric operation. Once deployed, the booms face several ongoing challenges:

- **Internal Vibrations:** Subsystems such as reaction wheels and cryocoolers generate dynamic disturbances that propagate through the structure. If these coincide with the boom's natural frequencies, resonant amplification may occur, jeopardizing alignment stability.
- **Thermal Gradients:** Continuous solar exposure introduces temperature variations between illuminated and shadowed surfaces. These gradients induce thermal bending moments that can lead to expansion, contraction, and curvature, potentially resulting in thermal flutter or jitter.
- **Thermo-Mechanical Interactions:** The coupling of thermal loads and mechanical stresses can cause fatigue, long-term deformation, or transient misalignments. Such effects require robust materials and carefully optimized geometries.
- **Maneuvering Accelerations:** Satellite maneuvers at L2 generate angular accelerations and lateral forces, which the booms must resist to preserve structural integrity and align-

ment under both static and dynamic loads.

In addition, the required deployment mechanism and boom architecture depend strongly on the spacecraft topology and interferometric baseline length. For instance, a linear array topology may allow more direct telescopic deployment, while an X-array configuration could require rotational deployment mechanisms or articulated booms. Longer baselines impose more demanding structural requirements, while shorter baselines may ease deployment but decrease angular resolution. These differences must be considered as part of the trade-off analysis.

To address the outlined challenges, the boom design must strike a balance between structural, deployment, and volumetric performance, with thermal effects handled through material choice. Key design considerations include:

- **High Stiffness:** A stiffer structure resists bending and vibrational deformations, helping maintain optical alignment. This is especially important at joints between boom segments, where mechanical instabilities or hysteresis can degrade performance.
- **Compact Stowage and Reliable Deployment:** The structure must minimize stowed volume while enabling controlled, predictable deployment in orbit. Mechanisms, segment interfaces, and actuation systems must be designed for both compactness and reliability.
- **Low Coefficient of Thermal Expansion (CTE):** Materials with low CTE reduce sensitivity to thermal gradients, minimizing deformation due to expansion or contraction. While the spacecraft sunshield helps reduce thermal variations, some residual gradients are unavoidable.
- **High Thermal Conductivity:** Good thermal conductivity allows heat to distribute evenly, mitigating gradients that cause thermal bending moments. This reduces thermal jitter and improves structural stability.

These considerations involve mechanical trade-offs between competing design requirements. For example, achieving high structural stiffness often requires thicker or more complex geometries, which can increase mass or stowed volume. Designs that enhance deployment reliability, such as additional hinges or locking mechanisms, may add mechanical complexity or reduce stiffness at segment interfaces. Furthermore, minimizing stowed volume to fit within the Ariane 6 payload fairing can constrain the boom's cross-sectional shape or segment length, potentially compromising structural stability or increasing sensitivity to vibration. Balancing factors such as stiffness, mass, deployment complexity, and compact stowage represents a key challenge in the mechanical design of the boom. Thermal considerations are addressed primarily through material selection and are discussed later in this chapter.

The goal of this chapter is to analyze and evaluate various types of deployment mechanisms, boom structures, and materials. This analysis considers their mechanical properties, such as stiffness, damping, and stowed volume, across different spacecraft topologies and baseline configurations. Based on this trade-off, the most promising combination of deployment mechanism and boom structure will be selected for each topology.

5.2. Boom Deployment systems

The physical design of the boom structure for the nulling interferometer mission requires a systematic approach to evaluate and optimize its deployment mechanisms and structural configurations. First, a review of deployment system technologies must be conducted, evaluating all mechanisms based on three key criteria: stiffness, the packing ratio and the associated boom diameters. These factors are critical for ensuring that the spacecraft fits within the limited payload fairing of the Ariane 6 while maintaining structural integrity. This evaluation process starts with an initial assessment, using insights from earlier research done by other researchers. Based on the results of this first evaluation, potential candidates will be identified for further analysis. Next, the different spacecraft topologies for the Linear Dual Chopped Bracewell (DCB) array and the X-array will be reviewed, and a trade-off analysis will be performed to determine which deployment mechanisms are best suited for each topology and which may be mandatory. This trade-off will be conducted with the constraints of the Ariane 6 and other large spacecraft subsystems in mind, ensuring feasibility within the mission's structural and volumetric limitations. The shortlisted options will then be simulated to assess their performance against one another. The best-performing mechanism, which optimally balances stiffness and stowage volume, will be selected for the final design. Boom materials and their properties, including stiffness, coefficient of thermal expansion (CTE), and thermal conductivity, will also be evaluated during this process. By integrating physical and material considerations into a comprehensive design framework, this approach aims to deliver a robust and reliable solution.

5.2.1. Evaluation of Deployment Technologies

A review on deployable structures [16] provides valuable insights into various technologies, supported by analyses, testing, and data extrapolated from existing literature back in 2010. Some of these technologies are even flight-proven. Figures 5.1, 5.2, and 5.3, derived from this review, summarize key information. These figures enable a preliminary assessment of deployment mechanisms, helping identify candidates for further research. The goal is to determine the mechanism that offers the highest stiffness while maintaining a compact stowed volume and the ability to deploy to large lengths. To provide a clear comparison of performance, the figures use different colors for the various technologies:

- **Yellow:** Telescopic Booms
- **Red:** Articulated Booms
- **Light Blue:** Deployable Truss Structures
- **Green:** Coilable Booms
- **Purple:** Shape Memory Composite Booms
- **Dark Blue:** Inflatable Booms

5.2.1.1. Bending Stiffness

High stiffness is crucial for a structure to resist bending and vibrational deformations, ensuring proper alignment and preventing resonance with disturbance frequencies. A stiffer structure provides greater alignment accuracy and stability, both of which are vital for the performance of the nulling interferometer. Upon visual inspection of the figure 5.1, it is evident that three

technologies, telescopic booms, articulated booms, and deployable truss structures, exhibit significantly higher bending stiffness potential compared to the others. According to the research done in [16] the telescopic boom achieves bending stiffness values ranging from 3×10^5 to $1.5 \times 10^7 \text{ Nm}^2$, while the articulated boom falls between 2.5×10^6 and $3 \times 10^7 \text{ Nm}^2$. The deployable truss structure offers values approximately between 8×10^5 and $2 \times 10^7 \text{ Nm}^2$. Given the critical importance of bending stiffness in the design, the other three technologies, coilable booms, shape memory composite booms and inflatable booms are deemed unsuitable for the structural design of the nulling interferometer.

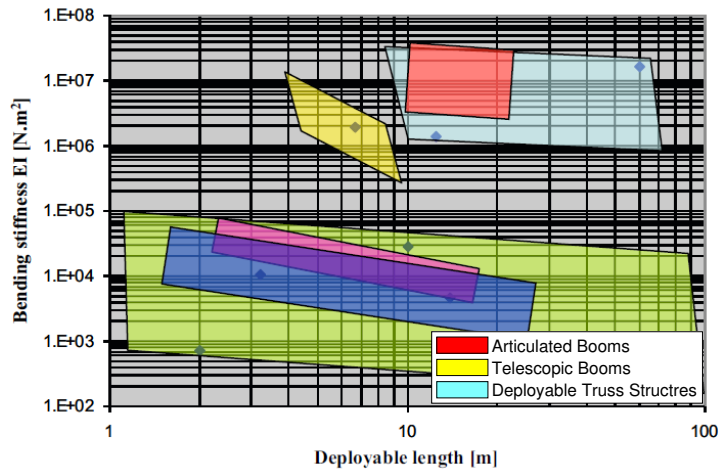


Figure 5.1: Deployable length versus bending stiffness[16]

5.2.1.2. Packing Ratio

The design of the nulling interferometer is constrained by the size of the payload of Ariane-6 fairing, making it essential for the structure and its deployment system to be stowed as compactly as possible. Furthermore, a better packing ratio allows for the possibility of larger baselines between the telescopes of the nulling interferometer, which enhances its scientific performance. Figure 5.2 illustrates the packaging ratio, which is defined as the ratio between deployable length and stowed length. According to the research in [16] the telescopic mechanism achieves a constant packing ratio of 0.075 over its entire length, while the deployable truss structure ranges between 0.06 and 0.045. In comparison, articulated deployment mechanisms exhibit poor packaging ratios, with the smallest value being 0.14, significantly higher than those of telescopic and truss structures. Although articulated booms have been studied for astrophysics missions such as FIRI and ATHENA, where they demonstrated excellent deployment accuracy and stiffness, their poor packaging ratio make them unsuitable for missions requiring compact stowage.

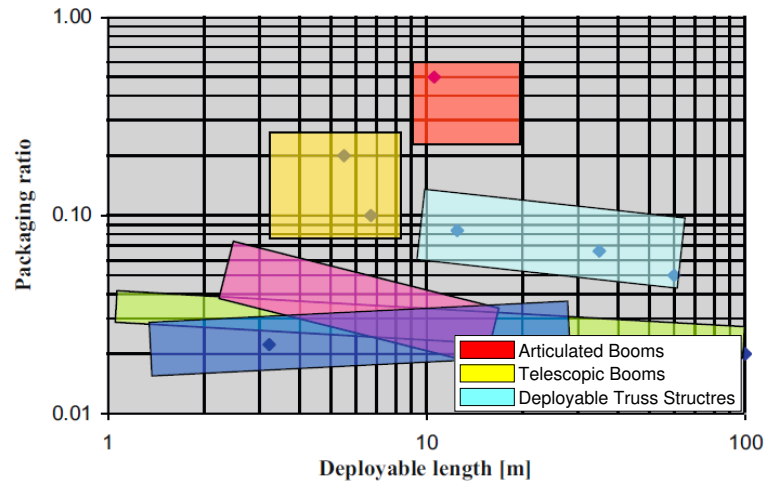


Figure 5.2: Deployable length versus packaging ratio[16]

5.2.1.3. Boom Diameter

While high bending stiffness and a good packing ratio are desirable, the overall size of the structure is also a critical factor. The packing ratio discussed above only considers the length of the structure and not the total volume. To estimate the stowed volume, the boom diameter is a critical factor. It not only affects its own stowed volume but also influences other design aspects. A larger diameter boom requires a larger sunshield and presents additional challenges in finding a suitable location within the Ariane 6 fairing. Figure 5.3 compares boom diameters for different deployed lengths[16]. Deployable truss structures, despite their excellent stiffness, have significantly larger diameters ranging from 600 to 1400 mm, making them less compact. In contrast, telescopic booms, with diameters ranging from approximately 100 to 650 mm, and articulated mechanisms, ranging between 200 and 400 mm, maintain relatively smaller diameters, enhancing their compactness and suitability for missions with stringent volume constraints.

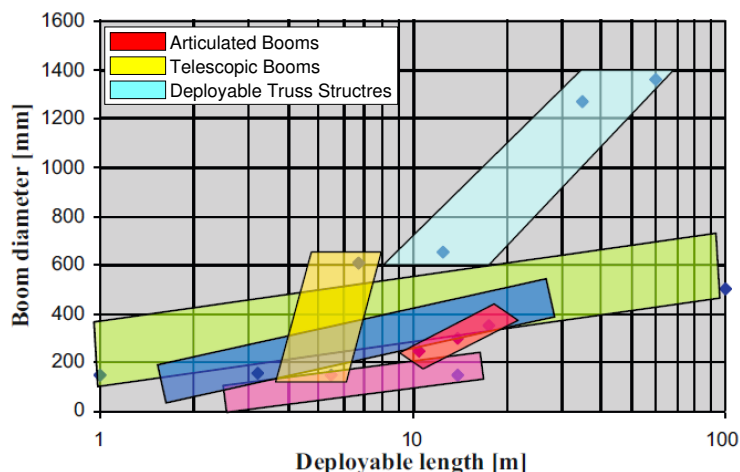


Figure 5.3: Deployable length versus boom diameter[16]

5.2.2. Boom Deployment and spacecraft topology

The choice of deployment mechanisms is intrinsically linked to the spacecraft topology and its baseline requirements. While the previous section analyzed deployment mechanisms based on performance metrics (bending stiffness, packing ratio, and outer diameter—this), section extends the trade-off by assessing their practical feasibility and necessity for the different spacecraft configurations.

Each topology, whether the Linear Dual Chopped Bracewell (DCB) array or the X-array, comes with unique spatial constraints and structural challenges. For shorter baselines (e.g., *Lin8* and *X8*), deployment may be unnecessary or minimal, while for longer baselines (e.g., *Lin32* and *X32*), specific mechanisms become mandatory due to performance constraints or volumetric constraints. This section systematically evaluates:

- Which type of mechanisms are mandatory for different topologies and baseline lengths
- Which deployment mechanisms are feasible within the stowed volume constraints of the Ariane 6 fairing
- Which mechanisms are impractical or introduce excessive complexity

By analyzing deployment feasibility within the mission scope, this section builds upon the initial performance-based trade-off to determine which deployment strategies will be selected for each spacecraft configuration.

5.2.2.1. Minimum Deployment Requirements for Different Spacecraft Topologies

To systematically evaluate the feasibility of each deployment system, we analyze their applicability to different spacecraft topologies and baseline lengths. Figures 2.4a, 2.4b, 2.4c, 2.5a, 2.5b, and 2.5c illustrate the deployed configurations of these topologies in comparison to the Ariane 6 fairing.

For the 8-meter baseline Linear Dual Chopped Bracewell topology, a deployment mechanism

is not required, as this configuration fits within the height constraints of the Ariane 6 fairing (Figure 2.4a). The only limiting factor is the size of the telescopes and other large spacecraft components. If these components constrain the available space too much and a non-deployable structure with an 8-meter baseline no longer fits, then a deployable mechanism should be considered.

In contrast, the 16-meter and 32-meter baseline Linear Dual Chopped Bracewell topologies (Figures 2.4b and 2.4c) require deployment mechanisms to extend from their stowed configurations to their final baseline lengths, as these lengths would not fit within the height constraints of the Ariane 6 fairing.

For the 8-meter baseline X-array topology, no deployment is needed to achieve the required baseline length in its stowed configuration. However, since it cannot fit within the Ariane 6 constraints as an X-shaped structure, a rotational deployment is necessary to transition it into its final X-shaped configuration (Figure 2.5a). Additionally, if large spacecraft components constrain the available space too much, similar to the 8-meter baseline Linear Dual Chopped Bracewell topology, a deployable mechanism may be required to ensure the structure fits within the fairing.

Similarly, the 16-meter and 32-meter baseline X-array topologies (Figures 2.5b and 2.5c) require rotational deployment to transition from a linear stowed configuration to an X shape. Additionally, further deployment is necessary to extend to their required baseline lengths.

	Rotational	Linear	mechanisms
Lin8	-	-	0
Lin16	-	X	4
Lin32	-	X	4
X8	X	-	2
X16	X	X	6
X32	X	X	6

Table 5.1: Spacecraft Topology Deployment Requirements

5.2.2.2. Volume Constraints

The available volume within the Ariane 6 fairing imposes strict limitations on deployable structures. In addition to volume constraints, the fairing's shape further restricts the allowable positioning and dimensions of these structures. Furthermore, deployable structures are not the only components that must fit within the fairing. The four telescopes will occupy a significant portion of the available space, along with other large subsystems such as the spacecraft bus and the beam combiner. To determine the feasible volume and placement for the deployment mechanisms, the sizing and positioning of these major components must first be defined. However, since the full study on the space-based nulling interferometer does not yet have concrete designs for its telescopes, spacecraft bus, and beam combiner, their positioning, shapes and sizes will need to be approximated based on fairing dimensions, optical requirements and comparisons with other large satellites, such as the JWST.

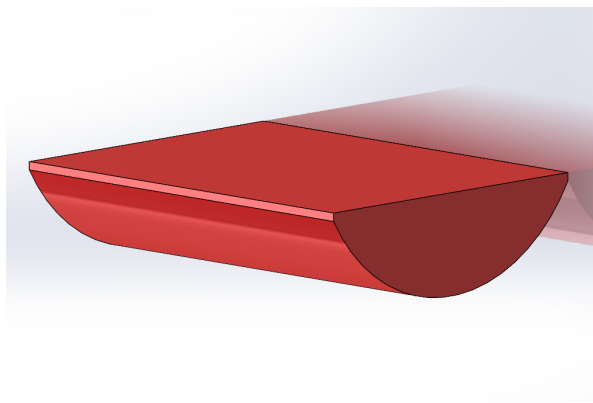


Figure 5.4: Spacecraft Bus Design

Spacecraft Bus The spacecraft bus of the space-based nulling interferometer will serve similar functions to that of the James Webb Space Telescope (JWST), including power generation and distribution, attitude control, propulsion, thermal management, and communication. Since JWST is also a large satellite with comparable mission requirements in terms of stability, thermal shielding, and deployment constraints, its spacecraft bus provides a suitable reference for volumetric analysis. As the nulling interferometer's spacecraft bus design is not yet finalized, its size will be approximated based on JWST's spacecraft bus to ensure a realistic estimation of available space within the Ariane 6 fairing while accounting for subsystem integration and deployable structures. The dimensions of the JWST spacecraft bus are approximated as a cuboid with sides measuring $3510 \text{ mm} \times 3210 \text{ mm} \times 1600 \text{ mm}$, resulting in a total volume of 18 m^3 . However, the spacecraft bus (SCB) for the space-based nulling interferometer will differ in shape due to the 90-degree shift in its stowage orientation compared to JWST. This subsequently also allows for optimization of available fairing volume. Instead of a cuboid, the SCB will take the form of a part-cylinder with a thin cuboid on top, ensuring structural efficiency while maintaining the required volume. The minimum edge thickness of the half-cylinder will be 10 cm. To facilitate design iterations, a MATLAB script (see Appendix C) has been developed, allowing for flexible adjustments to the SCB shape based on parameters such as the fairing radius, required volume, and height, which is set to 5 meters. A simplified visual representation of the current spacecraft bus design is shown in Figure 5.4.

Telescopes The design and sizing of the telescopes are still under consideration, with only the shape of the 2D mirrors currently defined. For this analysis, a three-mirror off-axis design with a 2.5-meter aperture will be used and an approximate weight of 750 kg. It is assumed that the secondary mirror will be deployable, allowing the telescope's stowed configuration to fit more efficiently within the Ariane 6 fairing. As the telescope design is not yet finalized only the M1 mirror, the largest optical component, is shown in Figure 5.5 to provide a sense of its scale and impact on spacecraft stowage. In the final design, the M1 will be mounted on a dedicated support structure. Therefore, the current representation is purely a placeholder and does not reflect a representative structural interface.

Beam Combiner The shape and dimensions of the beam combiner are still under evaluation. However, an approximation can be made for the first design iteration. The shape will likely

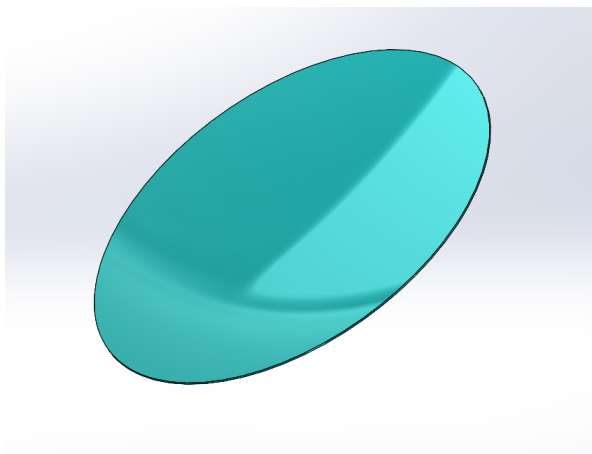


Figure 5.5: M1 mirror Telescope assembly

resemble a cuboid with a long length which is approximated to be 4 meters for this thesis, a thickness ranging from 0.7 to 1 meter, and a width that must remain within the physical limits of the Ariane 6 fairing. The width is chosen to be the same as the aperture diameter of the telescopes. A simplified visual representation of the beam combiner design is shown in Figure 5.6.

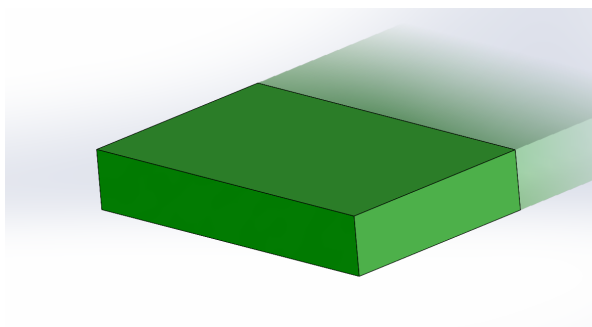
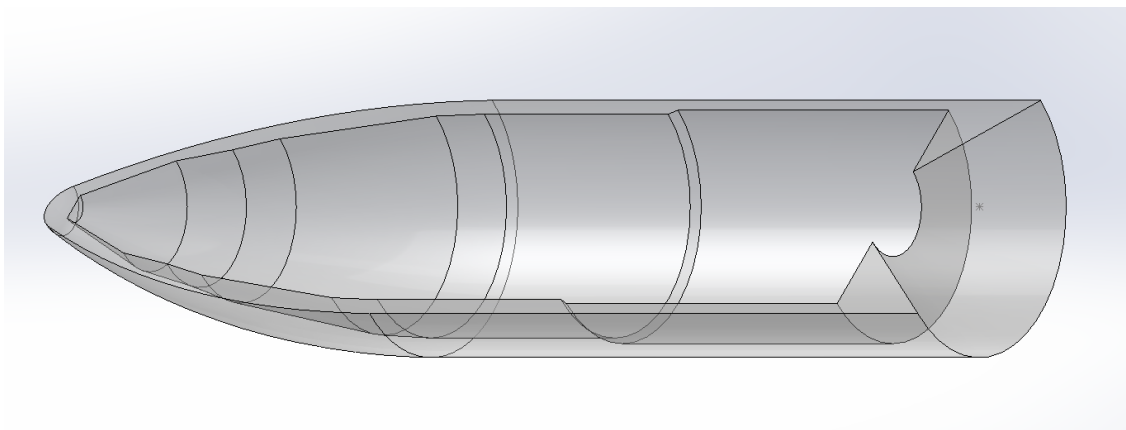


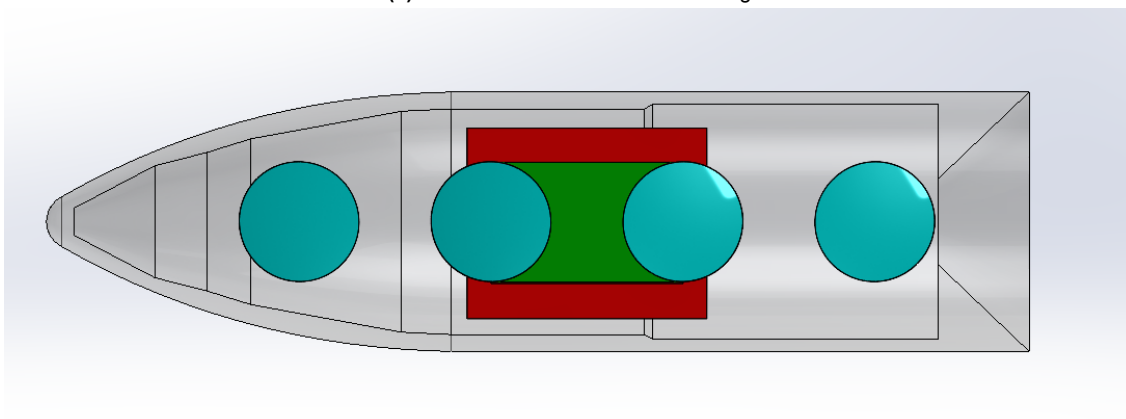
Figure 5.6: Beam Combiner approximation

Available Fairing Space Figure 5.7 shows a 3D visualization of the Ariane 6 fairing. The model is halved for clarity and is shown together with top and side views of the internal configuration of the large spacecraft components. The spacecraft bus and beam combiner are positioned centrally within the spacecraft and are therefore also located at the vertical midpoint of the fairing. The four telescopes, represented by their M1 mirrors, are spaced evenly along the height of the fairing, with the bottom telescope positioned just above the fairing's base. This configuration corresponds to the L8 spacecraft topology and confirms that the full arrangement, including all major components, fits within the fairing without requiring any deployment mechanisms. As such, this layout serves as the baseline stowed configuration for evaluating other, more complex topologies. Importantly, the figures reveal critical volumetric constraints. The top view (Figure 5.7b) shows that the only significant available space for stowing deployment mechanisms is alongside the telescopes, between them and the fairing walls. The side view (Figure 5.7c) highlights that the bottom region of the fairing that is reserved for elements such as the sunshield, radiators, and solar panels. Additionally, the nose end of the fairing tapers

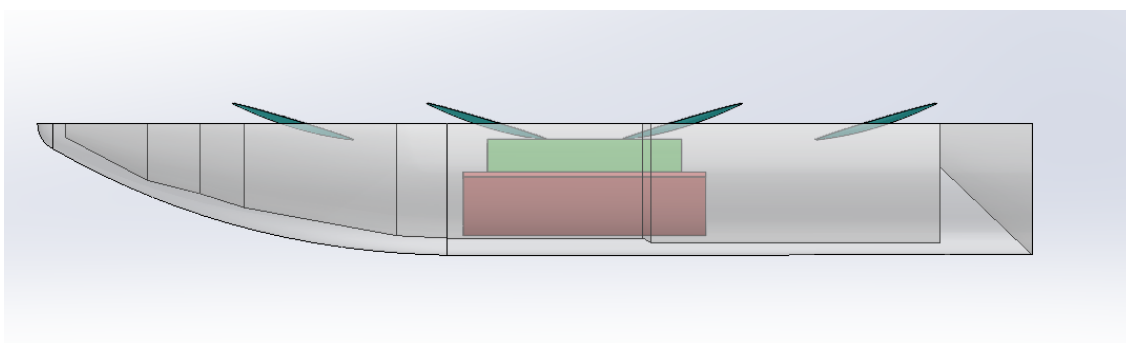
conically, significantly restricting the available diameter for any structural elements in that region. Furthermore, the central axis of the spacecraft is kept free to enable the uninterrupted transmission of light beams from the telescopes to the beam combiner, which limits options for placing structural components along the central axis. These spatial constraints impose strong limitations on the type and location of allowable deployment mechanisms.



(a) 3D model of halved Ariane 6 fairing



(b) Top view of fairing with large components



(c) Side view of fairing with large components

Figure 5.7: Visualization of the Ariane 6 fairing: (a) Halved 3D model showing interior shape, (b) top view with large components, and (c) side view confirming stowed configuration feasibility.

5.2.3. Conclusion Trade-off of Deployment Mechanisms

The objective of this trade-off assessment was to identify deployment systems that offer high stiffness, maintain a compact stowed volume, and can achieve the required deployed lengths. After evaluating various deployment technologies based on bending stiffness, packing ratio, and boom diameter, three candidates emerged as viable options: telescopic booms, articulated booms, and deployable truss structures.

However, incorporating the volume constraints derived from the Ariane 6 fairing layout reveals major limitations for truss and articulated designs. Deployable truss structures, despite their high stiffness and acceptable packing ratios, require large boom diameters ranging from 600 to 1400 mm. This makes them incompatible with the available stowage space alongside the telescopes, particularly toward the tapered nose section of the fairing where the conical geometry sharply reduces radial clearance.

The high stiffness and packing ratio attributed to deployable truss structures in earlier literature [16] assumes that every hinge is equipped with an zero-play clamping device. In practice such clamps occupy radial and axial space, and a large truss contains hundreds of them. The cumulative volume requirements of these clamps reduces the effective packing ratio and may introduce micro-slip that lowers the global stiffness. Consequently, the original scores of 5 for both stiffness and packing ratio are optimistic; a more realistic appraisal must acknowledge this penalty. For these reasons, deployable truss structures are deemed unfeasible for the nulling interferometer mission.

Articulated booms, while offering excellent stiffness and more manageable diameters, suffer from poor packing ratios. To achieve the necessary deployed lengths, multiple articulated sections would need to fold alongside each other. This increases mechanical complexity and results in highly inefficient use of the available volume, especially within the narrow side regions of the fairing. Moreover, the need to keep the central axis clear for light transmission to the beam combiner further limits placement options. Nevertheless, articulated booms are capable of rotational deployment, which is required for the X-array topologies. As such, articulated mechanisms will be employed specifically to enable the rotational transformation of these topologies from a linear to an X-shaped configuration.

Telescopic booms demonstrate a favorable balance of structural stiffness, diameter, and compact stowage. Their moderate diameters, typically between 100 and 650 mm, and a packing ratio of 0.075 make them well-suited for placement in the available side volumes next to the telescopes. However, telescopic booms are limited to translational deployment and cannot provide rotational motion. Therefore, for the X-array topologies, telescopic mechanisms alone are insufficient, and must be complemented by articulated elements to achieve the required rotational deployment.

To support the selection process, a scoring-based trade-off matrix is provided in Table 5.2. Each candidate mechanism is scored from 1 (poor) to 5 (excellent) based on six key criteria: stiffness, packing ratio, boom diameter, rotational capability, stowage feasibility, and mechanical complexity. The total score reflects the overall suitability of each mechanism for the nulling interferometer mission.

Mechanism	Stiffness	Packing Ratio	Diameter	Rotational	Compatibility	Total
Telescopic	4	5	5	1	5	20
Articulated	5	2	4	5	3	19
Truss	4	4	2	1	1	12

Table 5.2: Scoring comparison of candidate boom deployment mechanisms for the nulling interferometer mission (scores range from 1 (poor) to 5 (excellent))

As shown, telescopic booms score the highest overall, primarily due to their compactness, stiffness, boom diameter and fairing compatibility. Articulated booms score high as well due to their strong stiffness, boom diameter and rotational capability. However they are penalized by their low packing efficiency. Truss structures perform reasonably well in stiffness and packing but are disqualified due to their large diameters and low stowage feasibility within the fairing.

Therefore, the following conclusions are drawn:

- Telescopic deployment mechanisms will be used for all linear deployments, as they best satisfy both the structural and volumetric requirements of the mission.
- Articulated booms will be used only where rotational deployment is mandatory, specifically in the X-array topologies where a transition from a linear to an X-configuration is required. They will also serve as a fallback solution should the performance of telescopic booms prove inadequate.
- Deployable truss structures are excluded from further analysis due to their excessive diameters and incompatibility with the constrained fairing volume.

Although the reference study [16] indicates a maximum deployable length of 8 meters for telescopic systems, more recent advancements in boom technology have extended this range. These advancements will be explored in the next chapter to evaluate their potential for meeting the longer baseline requirements of the nulling interferometer mission.

5.2.4. Evaluation of Boom Materials

In this section, potential materials for the deployable boom structure are evaluated, focusing on their stiffness, coefficient of thermal expansion (CTE), thermal conductivity, and density. The materials under consideration are aerospace-grade aluminum alloys, titanium alloys, Invar, and pitch-based carbon fiber reinforced polymer. These materials are selected due to their widespread use in aerospace structures where minimizing mass, ensuring thermal stability, and maintaining structural integrity are critical requirements.

5.2.4.1. Material Properties and Trade-Off

Aluminum alloys, such as 7075-T6, are widely used in aerospace due to their relatively low density (2810 kg/m^3) and excellent thermal conductivity ($173 \text{ W/m}\cdot\text{K}$). While their Young's modulus is moderate (71.7 GPa), they exhibit a high CTE ($23.4 \mu\text{m/m}\cdot\text{K}$), which can lead to significant thermal deformation. Their favorable strength-to-weight ratio and ease of fabrication make them suitable for large structures, but the high thermal expansion limits their use in thermally sensitive components. [9]

Titanium alloys, particularly Ti-6Al-4V, offer excellent strength-to-weight performance, with a

Young's modulus of 113.8 GPa, density of 4430 kg/m³, and a relatively low CTE of 8.6 $\mu\text{m}/\text{m}\cdot\text{K}$. Though their thermal conductivity is low (6.7 W/m·K), their superior corrosion resistance and high-temperature capability make them suitable for structural spacecraft elements. However, their higher density and machining complexity increase cost and limit their use in deployable, mass-sensitive structures. [11]

Pitch-based CFRPs, such as XN-90-60S, offer extremely high stiffness, with fiber-level Young's modulus values up to 860 GPa and densities around 2190 kg/m³. Laminates using this fiber can achieve 0° tensile modulus up to 550 GPa. They exhibit very low CTE (<1 $\mu\text{m}/\text{m}\cdot\text{K}$) and excellent thermal conductivity at the fiber level (500 W/m·K). However, composite laminates are anisotropic: modulus in the transverse direction may drop to 5 GPa. Multidirectional layups (e.g., [0/90]s or [0/45/90/-45]s) help balance directional properties but reduce peak stiffness. In addition, the resin matrix significantly lowers thermal conductivity to around 20–60 W/m·K. Despite their brittleness and high cost, pitch-based CFRPs remain ideal for stiffness-critical, thermally stable components such as deployable booms and optical benches. [5]

Invar (Fe-36Ni alloy) is well known for its extremely low CTE (1.2 $\mu\text{m}/\text{m}\cdot\text{K}$), making it suitable for components requiring thermal dimensional stability. With a moderate Young's modulus (141 GPa) and a very high density (8120 kg/m³), it is typically used in ground-based or internal optical components, not in deployables where mass is critical. [4]

Table 5.3: Comparison of Candidate Materials for Deployable Boom Structure

Material	Specific Modulus ($10^6 \text{ m}^2/\text{s}^2$)	CTE ($\mu\text{m}/\text{m}\cdot\text{K}$)	Thermal Conductivity (W/m·K)
7075-T6 Aluminum	25.5	23.4	173
Ti-6Al-4V	25.7	8.6	6.7
Pitch-Based CFRP	392	<1	20–60
Invar 36	17.4	1.2	13

Material Selection: Based on this trade-off, pitched-based CFRP's offer the most favorable material characteristics for deployable boom structures. Their high specific modulus and low CTE provide excellent dimensional stability and stiffness with minimal thermal deformation. Pitch-based CFRP is selected for the primary boom design to maximize stiffness and packaging efficiency. Its moderate thermal conductivity also contributes to reducing gradients in the cold environment at L2. PAN-based CFRP may be used in secondary or cost-sensitive components, or layered with pitch fiber to tune performance. These material properties serve as the foundation for the detailed boom structure design and simulation phase.

6

Telescopic Booms

Telescopic booms are a class of deployable structures widely used in space applications to extend payloads, antennas, and structural components—for example the two-section Deployable Tower Assembly and the seven-tube Mid-Boom Assemblies that deploy the five-layer sunshield on the James Webb Space Telescope [12]. Their design combines high precision, structural stiffness, and compact stowage, making them suitable for missions requiring high accuracy and stability, such as astrophysics telescopes and interferometers. A telescopic boom consists of concentric tubular sections that nest within each other when stowed. Deployment is typically driven by motorized lead screws, spring-based actuators, or Storable Tubular Extendable Mechanisms (STEM). Other configurations, such as spindle-and-nut or cable-and-pulley systems, may also be employed depending on the mission requirements. The deployment process proceeds in sequential stages:

1. **Initiation:** The innermost tube is extended by the actuation mechanism, such as a STEM or motor-driven worm screw, generating sufficient force to overcome static friction [13].
2. **Locking:** Locking mechanisms such as tapered pins or preloaded latches secure adjacent sections in place, enhancing structural rigidity. For instance, tapered pins are preloaded to ensure stiffness during deployment, with tolerances as low as 0.05 mm achieved in advanced systems [3].
3. **Guidance:** Rails or stabilizers are incorporated to prevent misalignment and reduce the risk of jamming due to surface irregularities or elastic deformation. These features also mitigate torsional stresses during deployment [18].
4. **Completion:** The deployment sequence repeats until all segments are fully extended and locked. Fail-safe mechanisms ensure deployment integrity even in cases of partial spring failure [13].

6.1. Research findings on Telescopic booms

6.1.1. Telescopic Tubular Mast (TTM): Design, Features, and Performance

The Telescopic Tubular Mast (TTM) [13] is a deployable boom system developed by Astro Aerospace, a division of Northrop Grumman Aerospace Systems. It is designed to meet the

requirements of space applications, including precise deployment, high structural stability, and compact stowage. The TTM has been extensively tested under laboratory conditions, demonstrating its potential capability in long boom applications.



Figure 6.1: Deployed stiffness test configuration for the Telescopic Tubular Mast (TTM), Developed by Astro Aerospace, a division of Northrop Grumman Aerospace Systems[13]

Design Overview The TTM consists of 17 thin-walled telescoping tubes constructed from high-modulus graphite composite material, which offers a lightweight yet robust design. Each tube is optimized for stiffness, strength, and mass, with the outer diameters decreasing progressively from the base to the tip. The diameter of the tubes decreases by approximately 1.3 cm between successive tubes to accommodate the latching and guiding mechanisms.

- The largest tube (Tube 1), located at the base, has an outer diameter of 31.8 cm (12.5 inches), a wall thickness of 0.51 mm, and a bending stiffness EI of $868 \times 10^3 \text{ N}\cdot\text{m}^2$.
- The smallest tube (Tube 17), located at the tip, has an outer diameter of 11.4 cm (4.5 inches), a wall thickness of 1.02 mm, and a bending stiffness EI of $81.1 \times 10^3 \text{ N}\cdot\text{m}^2$.

These tubes are stowed compactly, with a stowed length of 2.16 meters (85 inches), and are capable of deploying to an impressive 34.3 meters (1350 inches), resulting in a packaging ratio of 0.063. The deployment mechanism uses a Storable Tubular Extendable Mechanism (STEM), a lightweight and reliable system driven by a brushless DC motor (Figure 6.2). The STEM consists of a “C”-shaped section of thin formed metal that is flattened and rolled onto a spool for launch. Once in orbit, the motor-driven spool actuates the STEM, causing it to unroll and push against the tip plate of the stowed tube segments. This motion pushes the payload and package of nested tubes from within the fixed external base tube. When the package reaches the end of the fixed segment, the outermost tube latches into place. This tip deployment process continues sequentially until all segments are fully extended.

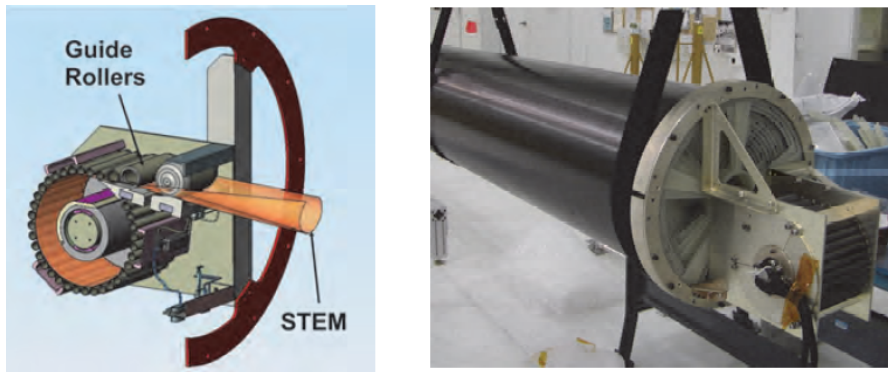
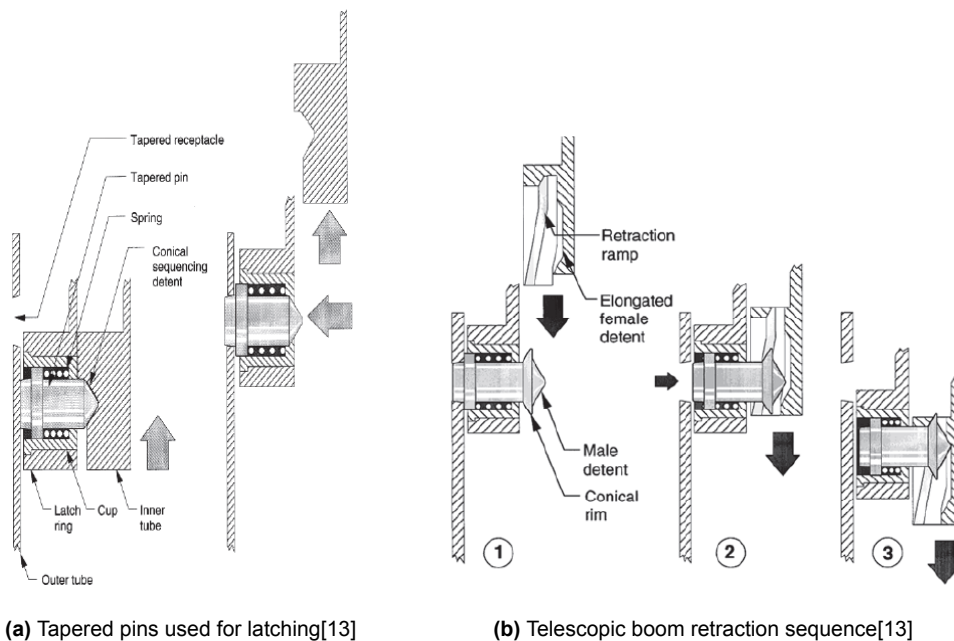


Figure 6.2: STEM used for deployment of TTM

Deployable booms in the STEM family are extremely lightweight and mechanically simple. With over 300 successful deployments in space and no known failures, the system has a proven track record of reliability. Once deployed, each tube segment is locked into position using a spring-loaded latching mechanism (Figure 6.3). This mechanism employs tapered pins to create secure mechanical interfaces between adjacent segments, ensuring structural rigidity and alignment throughout the full length of the deployed boom.



(a) Tapered pins used for latching[13]

(b) Telescopic boom retraction sequence[13]

Figure 6.3: (a) Tapered pins used for latching and (b) Telescopic boom retraction sequence.

Performance Characteristics The TTM has been tested for its mechanical performance under various operational conditions. Key performance metrics include:

1. **Mass:** The total mass of the system is approximately 58 kg (128 pounds), which is lightweight for its capabilities.
2. **Deployment Time:** The system deploys fully within **14 minutes**, meeting operational requirements. A feedback control system ensures smooth operation, compensating for fluctuations in velocity caused by friction and latching forces.

3. Frequency Requirements:

- In the **stowed configuration**, the fundamental natural frequency is **37.88 Hz**, exceeding the required 35 Hz. This ensures the mast remains stable during launch.
- In the **deployed configuration**, the fundamental natural frequency is **0.1 Hz**, meeting the minimum requirement. Although this value appears low, it is acceptable given the mast's deployed length of 34.3 meters. Due to the inverse-square relationship between natural frequency and structural length, such values are typical for long cantilevered systems.

Structural Stability The deployed TTM demonstrates excellent stiffness, and the addition of load rings at each tube's tip enhances local stability, reducing deformations under load. These features enable the mast to handle axial, shear, and moment loads effectively, making it suitable for supporting payloads such as telescopes, large sunshields, and solar panels. The TTM's performance has been validated through extensive analysis and testing. It offers a lightweight, compact solution for space applications that demand large deployable structures. With its innovative latching mechanism, advanced composite materials, and optimized structural stiffness ranging from $868 \times 10^3 \text{ N}\cdot\text{m}^2$ to $81.1 \times 10^3 \text{ N}\cdot\text{m}^2$.

6.1.2. COMAT-CNES Telescopic Boom

The Telescopic Boom developed in collaboration between COMAT and CNES [3] is designed to position a payload at a specific location away from a satellite while ensuring rigidity, precision, and reliability during deployment. Their engineering model has demonstrated promising results, with further testing planned for space qualification.



Figure 6.4: COMAT-CNES Telescopic boom 6-Tube configuration

Design Overview The Telescopic Boom employs a patented synchronization and locking mechanism (European Patent FR 2 929 593 – A1). The system is composed of concentric tubular parts made of carbon resin. In its stowed configuration, the tubes are nested inside

one another, with the smallest inner tube housing the payload. Deployment is powered by an electric motor driving a worm screw system.

- Stowed configuration: 120 mm diameter × 554 mm length.
- Deployed configuration:
 - 6-Tube Model: 2.7 m (specification: 3.0 m).
 - 8-Tube Model: 4.0 m.

The boom includes interlocking mechanisms between each tube, consisting of front and back rings that provide preloaded surface contact and ensure rigidity. During deployment, each tube is guided by three pins sliding along the central worm screw. These features enhance deployment precision and structural stability.

Performance Characteristics The Telescopic Boom has undergone extensive testing to evaluate its performance in simulated space conditions. Key performance metrics include:

1. Mass:
 - 6-Tube Model: 2.92 kg (measured, excluding payload and cables).
 - 8-Tube Model: 3.15 kg.
2. Deployment Time:
 - 6-Tube Model: 8 minutes.
 - 8-Tube Model: 11.4 minutes.
3. Frequency and Rigidity:
 - The first natural frequency of the deployed boom (6-tube model with a 400 g payload) was measured at 3.25 Hz, exceeding the 1 Hz requirement.
 - For the 8-tube model, predictions estimate a first natural frequency of 5.6 Hz.
4. Deployment Accuracy:
 - Using a laser theodolite, the deployment accuracy of the 6-tube model was measured to have a deviation of -0.761 mm, corresponding to 0.03% of the total deployed length. This level of precision ensures minimal misalignment and meets the stringent requirements for space applications.
 - The system demonstrated a consistent accuracy of ± 1.5 mm, highlighting its reliability across multiple tests.

Modular Configurations The modular design of the Telescopic Boom allows for customization to meet mission-specific requirements. Potential configurations include:

- Increasing deployed length by:
 - Adding more tubes (increasing stowed diameter).
 - Extending individual tube lengths (increasing stowed length).
- Exploring tube cage designs to reduce mass while maintaining rigidity and precision.

- Developing bi-directional or multi-directional deployment systems for complex payload positioning.

6.1.3. Implications for Nulling Interferometer Design

The performance of the TTM and COMAT-CNES booms demonstrates the feasibility of using telescopic structures for high-precision space missions. The TTM offers extreme deployment length and compact stowage, highlighting the potential for achieving long baselines with high packaging efficiency, critical for interferometric configurations. Its relatively low deployed frequency is acceptable for passive structures in deep space, especially when aided by damping or control systems. The COMAT-CNES boom emphasizes modularity, deployment accuracy, and structural stiffness over shorter distances, offering precision and adaptability. For the nulling interferometer, which requires both tight alignment tolerances and deployment within the constrained volume of the Ariane 6 fairing, these examples show that a telescopic boom can be tailored to balance stowage, stiffness, and precision. Design considerations for the proposed boom will leverage this trade-off space to achieve a structurally stable, accurately deployable solution within the mission constraints.

6.2. Telescopic Boom Design

This section details the design of a telescopic boom for various baseline lengths. Based on the dimensional results obtained for the individual tube sections, 3D models will be created in SolidWorks.

6.2.1. Telescopic Tube Section

Before designing the telescopic boom, it is necessary to define the characteristics of a single section and how multiple sections interconnect. Each tube in the telescopic mechanism is modeled as a hollow cylinder with specific dimensions.

The first section, referred to as Section 1, is characterized by its outer diameter, inner diameter, and length. The difference between the outer and inner diameters defines the wall thickness of the section. The subsequent section, Section 2, has an outer diameter smaller than the inner diameter of Section 1 by an amount sufficient to accommodate the latching mechanism that connects the sections. Similarly, the inner diameter of Section 2 is determined by subtracting its wall thickness from its outer diameter.

This sequence continues for a specified number of sections, which is determined by the overall length of the boom and the length of each individual section. Each section also features a small overlap with the next, facilitating secure latching. Using the dimensions of each section, calculated based on these relationships, the second moment of area of each hollow cylinder can be determined using the properties of the chosen material, as given by:

$$I = \frac{\pi}{64}(D_{\text{outer}}^4 - D_{\text{inner}}^4) \quad (6.1)$$

6.2.2. Design Input Parameters

Telescopic booms will be designed to accommodate the different linear deployments to achieve the baseline lengths of 8, 16, and 32 meters. The design aims to maximize stiffness while

minimizing stowed volume. To achieve these objectives, the following parameters must be determined:

- Radius required for the latching mechanisms
- Wall thickness of each tube
- Outer diameter of the base tube
- Length of each section
- Overlap fraction between sections

Minimizing the radius reduction between successive tubes is critical, as smaller radius tubes result in decreased bending stiffness. To maximize the overall bending stiffness of the telescopic boom, the radius required for the latching mechanisms should be as small as feasible. Based on the design of the TTM (see Figure 6.3a), a radius reduction of 0.0065 meters, corresponding to a diameter decrease of 1.3 cm, has been selected.

6.2.3. Geometric Trade-Offs: Wall Thickness vs. Outer Diameter

Achieving a high bending stiffness for a telescopic tube can be done in two ways: by increasing the outer diameter or by increasing the wall thickness. However, the objective is not only to maximize bending stiffness; the spacecraft must also meet a structural requirement of a minimum fundamental natural frequency of 2 Hz. This raises a critical design question: is it more efficient to increase the wall thickness or to fix the wall thickness and instead increase the outer diameter?

The structural performance of telescopic booms is governed by their flexural rigidity, defined as the product EI , where E is the Young's modulus of the material and I is the second moment of area (equation 6.1). For thin-walled circular tubes, the cross-sectional area can be expressed as:

$$A = \frac{\pi}{4} (D_o^2 - D_i^2) \quad (6.2)$$

with wall thickness defined as:

$$t = \frac{1}{2}(D_o - D_i) \quad (6.3)$$

Bending Stiffness and Mass Efficiency The natural frequency of a cantilever beam with distributed mass is proportional to the square root of the ratio between flexural rigidity and mass per unit length:

$$f_1 \sim \sqrt{\frac{EI}{\rho A}} \sim \sqrt{\frac{I}{A}} \quad (6.4)$$

This shows that maximizing the ratio I/A is key to achieving higher structural frequencies. For a hollow circular tube, the second moment of area I and cross-sectional area A are given by:

$$I = \frac{\pi}{64} (D_o^4 - D_i^4) = \frac{\pi}{64} (D_o^4 - (D_o - 2t)^4) \quad (6.5)$$

$$A = \frac{\pi}{4} (D_o^2 - D_i^2) = \frac{\pi}{4} (D_o^2 - (D_o - 2t)^2) \quad (6.6)$$

Substituting these into the frequency relation yields:

$$f_1 \sim \sqrt{\frac{I}{A}} = \sqrt{\frac{1}{16} \cdot \frac{D_o^4 - (D_o - 2t)^4}{D_o^2 - (D_o - 2t)^2}} \quad (6.7)$$

This expression captures the dependence of natural frequency on both wall thickness t and outer diameter D_o . It can be used to evaluate the efficiency of two different design strategies: increasing wall thickness at fixed outer diameter, or increasing outer diameter at fixed wall thickness.

Effect of Increasing Wall Thickness Increasing the wall thickness t increases both stiffness and mass, but not equally. The quartic difference in Equation (6.5) grows more slowly than the quadratic difference in Equation (6.6) for small t . This results in diminishing returns in the stiffness-to-mass ratio. While initial increases in t significantly improve f_1 , later increases lead to proportionally smaller gains.

Effect of Increasing Outer Diameter In contrast, increasing the outer diameter D_o at fixed wall thickness causes both the numerator and denominator in Equation (6.7) to increase, but in a more favorable manner. Since the second moment of area grows with D_o^4 and the cross-sectional area with D_o^2 , the ratio I/A scales approximately with D_o^2 . This leads to a near-linear improvement in natural frequency with diameter, with a more favorable stiffness-to-mass trade-off than increasing wall thickness.

Simulation Results: Varying Wall Thickness To evaluate the practical implications of these geometric trade-offs, a series of finite element simulations were conducted in ANSYS Mechanical. The first simulation involved increasing the wall thickness from 1.0 mm to 3.0 mm in steps of 0.5 mm, while keeping the outer diameter constant at 200 mm. The resulting changes in natural frequency are summarized in Table 6.1.

Table 6.1: Effect of Wall Thickness on First Natural Frequency, Relative Area, and Efficiency

Wall Thickness (mm)	Relative Frequency Increase	Relative Area Increase	Efficiency
1.0	–	–	–
1.5	21.1%	50.00%	0.422
2.0	14.2%	33.33%	0.426
2.5	10.4%	25.00%	0.416
3.0	8.7%	20.00%	0.435

The results confirm the theoretical expectation that increasing wall thickness yields diminish-

ing returns in terms of natural frequency. While the initial gain from 1 mm to 1.5 mm is significant (+21.1%), subsequent increments result in progressively smaller improvements. This is consistent with the earlier observation that the D_i^4 term rapidly dominates in the inertia expression, limiting further stiffness gains. Based on the results of the analytical and simulation study, a constant wall thickness of 1 mm is selected for all telescopic boom designs. This value represents the largest wall thickness used in the Telescopic Tubular Mast (TTM). For each spacecraft topology, the required outer diameter D_o of the base tube will be determined to achieve a minimum first natural frequency of 2 Hz. This sizing process will be performed iteratively during the simulation phase and adapted to the specific deployed lengths and loading conditions of each configuration.

Simulation Results: Varying Outer Diameter In the second simulation, the outer diameter was increased from 200 mm to 240 mm in steps of 10 mm, while maintaining a constant wall thickness of 1 mm. The results are shown in Table 6.2.

Table 6.2: Effect of Outer Diameter on First Natural Frequency, Relative Area, and Efficiency

Outer Diameter (mm)	Relative Frequency Increase	Relative Area Increase	Efficiency
200	—	—	—
210	6.75%	5.00%	1.350
220	7.56%	4.76%	1.588
230	6.20%	4.55%	1.363
240	6.82%	4.35%	1.567

Unlike thickness variation, increasing the outer diameter provides more consistent and efficient improvements in natural frequency. Comparing these results with the corresponding increases in cross-sectional area (approximately 4–5% per step) shows that frequency gains (6–7.5%) generally outpace the associated mass increase. This matches the analytical result that $f_1 \sim D_o$ under thin-walled assumptions, confirming that diameter scaling offers superior structural performance per unit mass.

6.2.4. Section Length and Overlap Fraction

The total deployed length of each telescopic boom is achieved by stacking multiple nested sections that extend sequentially. Each section slides out from within the previous one and must maintain sufficient engagement with its predecessor to ensure structural integrity during and after deployment. This engagement length is defined as the overlap fraction, and is based on design data from the Telescopic Tubular Mast (TTM), for which a constant overlap of 10 mm is used.

The required number of sections and their individual lengths vary per spacecraft topology. The base configuration used for calculating the stowed distances is the L8 layout. In this configuration, the stowed distance from the center of the spacecraft, where the beam combiner and spacecraft bus are located, to the first telescope is 2 m, and the distance from the first to the second telescope is 4 m. These stowed distances define the maximum retraction lengths into which each mechanism must fit. As such, these fixed stowed lengths apply to all other topologies built upon the L8 baseline.

For instance, the L16 topology requires a deployed length of 4 m between the beam combiner and the first telescope, and 8 m between the first and second telescope. Given the 2 m and 4 m stowed lengths, respectively, the corresponding extension ratios are 2:1. Similarly, for the L32 configuration, the deployed distances become 8 m and 16 m, while the stowed lengths remain unchanged.

To determine the length of each telescopic section, the deployed length of the boom is divided by the number of sections n , while also accounting for the required overlaps. The section length L_{sec} is then given by:

$$L_{\text{sec}} = \frac{L_{\text{deployed}}}{n} \quad (6.8)$$

Each deployed section must maintain a 10 mm overlap with its predecessor. As a result, the stowed length of the boom is not simply the section length but must include all overlapping segments. The total stowed length L_{stowed} is expressed as:

$$L_{\text{stowed}} = L_{\text{sec}} + (n - 1) \cdot L_{\text{overlap}} \quad (6.9)$$

where:

- L_{deployed} is the total deployed boom length,
- $L_{\text{sec}} = \frac{L_{\text{deployed}}}{n}$ is the length of one extended section,
- $L_{\text{overlap}} = 0.01$ m is the constant overlap per section.

Under this definition, the first (outermost) telescopic segment has a base length equal to L_{sec} , and every subsequent inner section must include an additional 10 mm to ensure proper overlap with the preceding tube. Consequently, the total stowed length of the boom equals the length of the base section plus the cumulative overlaps of the remaining $n - 1$ sections.

This sectioning approach ensures that each section maintains sufficient engagement to preserve axial stiffness and buckling resistance during both deployment and operation. The method described here is used uniformly across all spacecraft topologies, including the L16 and L32 layouts, which employ combinations of 2 m or 4 m telescopic sections to achieve deployed lengths of 4 m, 8 m, and 16 m.

The same telescopic mechanisms are also reused in the X-array configurations (X16 and X32), but arranged in a different geometric layout. Rather than sequentially connecting telescopes along a linear path, the X-array deploys its telescopic booms from a central rotation mechanism. In this layout, the longest boom extends outward first from the beam combiner to the articulation point. From there, two additional telescopic mechanisms extend orthogonally from the center of the rotation mechanism to reach the individual telescopes. This branching structure introduces a more compact footprint during launch while maintaining the required baseline distances for interferometric operation.

Importantly, the telescopic booms in X-array topologies use the same deployed lengths and section lengths as in the linear layouts. For example, X16 uses the same 4 m and 8 m deployed lengths as L16 but with 2 m and 4 m section lengths in reversed order. Similarly, X32

uses 8 m and 16 m booms with the same 2 m and 4 m section types as in L32. The total stowed lengths of these mechanisms are determined using the same expressions, ensuring mechanical consistency across all configurations.

A constant wall thickness of 1 mm is applied to all telescopic boom designs. This value was chosen based on the maximum thickness used in the TTM, offering high stiffness while minimizing additional mass. Between each section, a radius reduction of 6.5 mm is applied to accommodate the latching and guiding mechanisms, consistent with the TTM system. The required outer diameter for the base tube will be determined iteratively for each topology to ensure that the deployed boom satisfies the minimum 2 Hz natural frequency requirement.

The full telescopic boom configurations, including deployed length, number of sections, section length, stowed length, fixed wall thickness, and radius reduction, are summarized in Table 6.3.

Table 6.3: Telescopic Boom Design Parameters Across L and X Topologies (All lengths in meters)

Topology	Deployed Length	Sections n	Section Length	Stowed Length	Wall Thickness	Radius Reduction
L16	4.00 m	2	2.00 m	2.01 m	1.0 mm	6.5 mm
L16	8.00 m	2	4.00 m	4.01 m	1.0 mm	6.5 mm
L32	8.00 m	4	2.00 m	2.03 m	1.0 mm	6.5 mm
L32	16.00 m	4	4.00 m	4.03 m	1.0 mm	6.5 mm
X16	8.00 m	2	4.00 m	4.01 m	1.0 mm	6.5 mm
X16	4.00 m	2	2.00 m	2.01 m	1.0 mm	6.5 mm
X32	16.00 m	4	4.00 m	4.03 m	1.0 mm	6.5 mm
X32	8.00 m	4	2.00 m	2.03 m	1.0 mm	6.5 mm

7

Spacecraft Designs

This chapter provides an overview of the spacecraft designs and their components relevant to the various topologies evaluated in this study. The components presented are essential for the mechanical realization and structural simulation of the deployable configurations. Visualizations and simplified representations are included to illustrate key mechanical interfaces, geometric constraints, and connection strategies.

7.1. Final Components and Design Representations

7.1.1. Telescopic Mechanism Designs

Telescopic mechanisms are the main deployable structures used in the spacecraft designs. These mechanisms are composed of concentric cylindrical tubes nested within one another. During deployment, each section extends outward sequentially, guided and supported by internal interfaces. A latching mechanism ensures structural continuity and stiffness between deployed sections. These interfaces are modeled as bonded contacts, effectively treating the transition between tube sections as rigid once deployment is complete. An example interface between two boom segments is shown in Figure 7.1, illustrating the geometric principle used for all configurations.



Figure 7.1: Interface between two telescopic boom sections

The following figures illustrate the baseline designs of telescopic booms for different deployed lengths and section counts, tailored to the specific topological configurations of the spacecraft. The starting outer diameter for each of these telescopic booms will differ depending on the spacecraft topology.

4 m Boom with 2 Sections The 4 m boom is composed of two nested segments and is implemented in both the Lin16 and X16 topologies. Figure 7.2 presents both the stowed and deployed configurations.

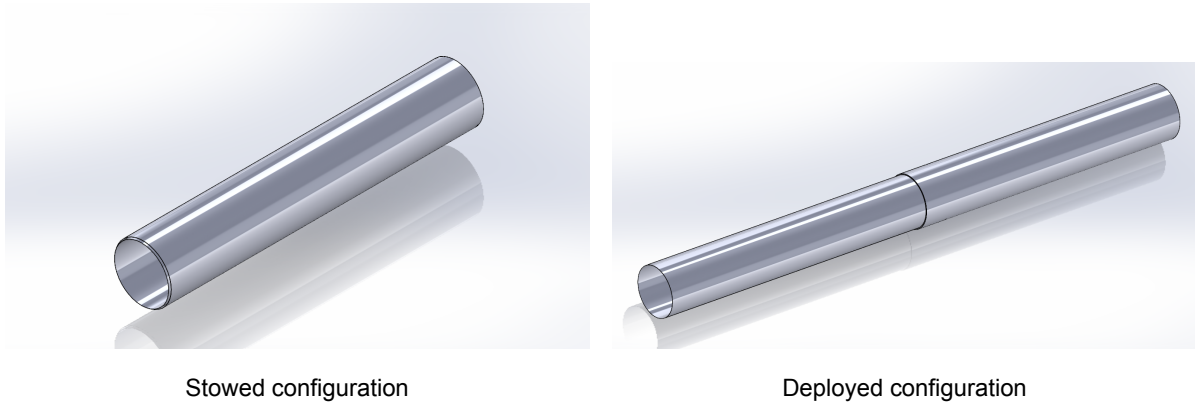


Figure 7.2: 4 m boom with 2 sections: stowed and deployed configurations

8 m Boom with 2 Sections This 8 m boom variant also uses two sections and is used in the Lin16 and X16 spacecraft. The configurations are depicted in Figure 7.3.

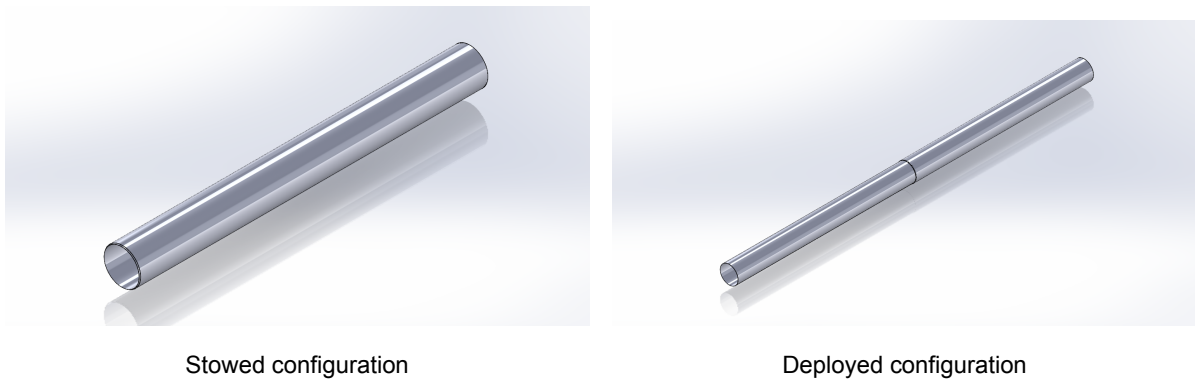
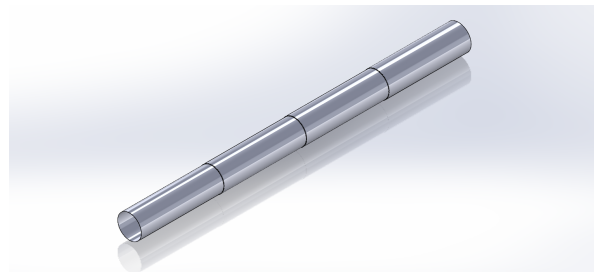


Figure 7.3: 8 m boom with 2 sections: stowed and deployed configurations

8 m Boom with 4 Sections In the Lin32 and X32 configurations a 4-section telescopic boom is used to achieve the 8 m deployed length. Figure 7.4 shows both states.



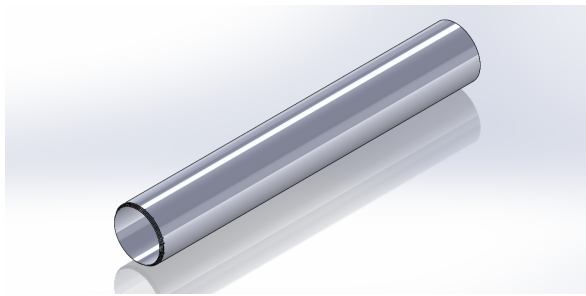
Stowed configuration



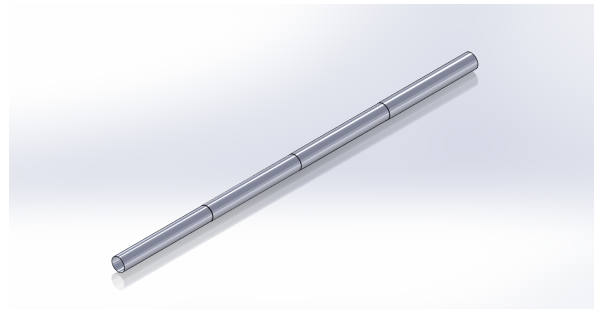
Deployed configuration

Figure 7.4: 8 m boom with 4 sections: stowed and deployed configurations

16 m Boom with 4 Sections The 16 m boom is the longest configuration implemented, composed of four nested sections. It is featured in both Lin32 and X32 spacecraft designs. The configurations are shown in Figure 7.5.



Stowed configuration

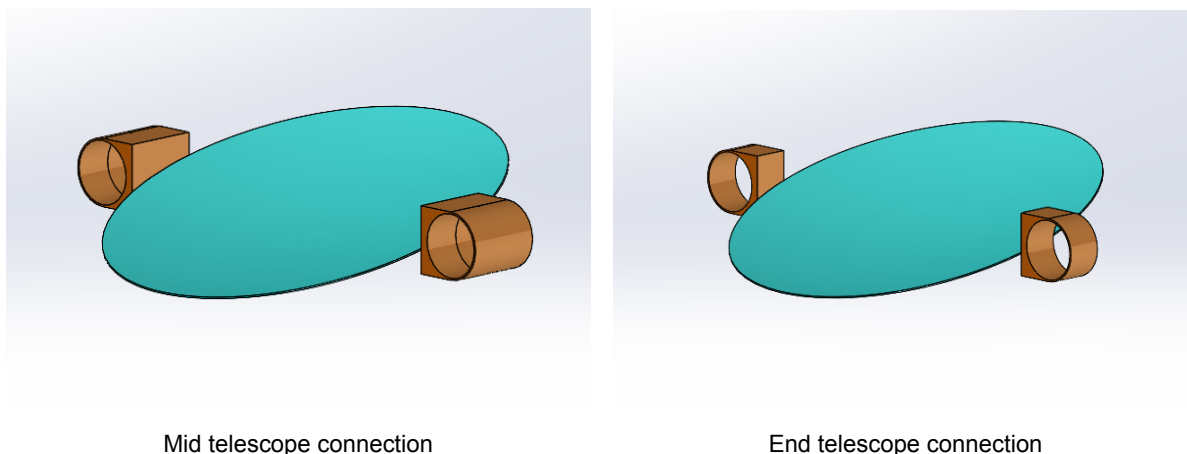


Deployed configuration

Figure 7.5: 16 m boom with 4 sections: stowed and deployed configurations

7.1.2. Simplified Telescope Connection Interfaces

The telescope mounting points vary across spacecraft topologies. In linear designs such as Lin16 and Lin32, telescopes positioned between two booms must accommodate differing diameters due to the diameter transitions of each telescopic segment. In contrast, the X-array configurations place telescopes at the outermost ends of each boom, avoiding this asymmetry. Figure 7.6 presents simplified connection geometries for a mid-mounted telescope (with differing interface diameters) and an end-mounted telescope. In the final design, the primary mirror (M1), secondary mirror (M2), and other optical components will require a dedicated support structure. In this study, it is assumed that sufficient design freedom exists to integrate these support structures within the footprint of the M1 mirror diameter.



Mid telescope connection

End telescope connection

Figure 7.6: Simplified connection geometries for mid and end telescope mounting

7.1.3. Boom-to-Beam Combiner Connection

Each boom structure must interface rigidly with the central spacecraft bus and beam combiner. This connection is critical for modal analysis and is modeled using a simplified flat mounting surface, as shown in Figure 7.7. The flat surface acts as a fixed boundary condition in structural simulations, representing the high-stiffness interface of the boom with the central body.

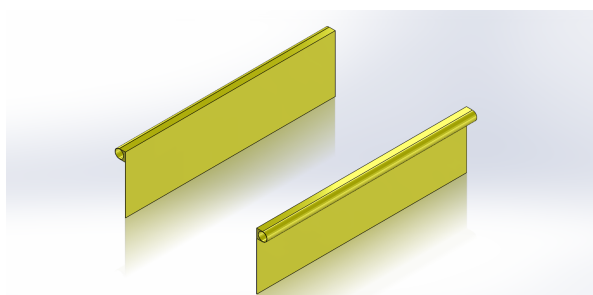
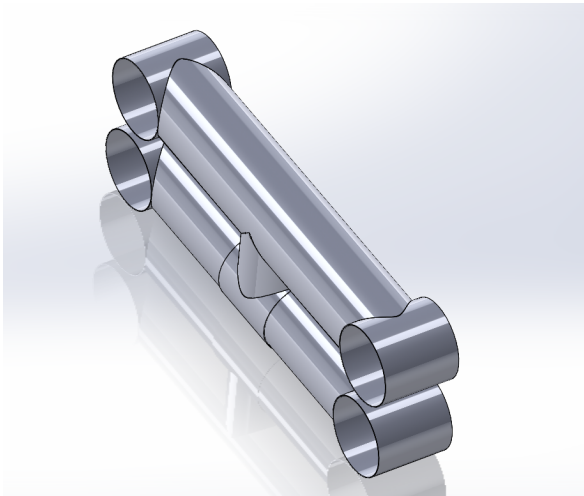


Figure 7.7: Simplified example of booms connecting to the central beam combiner

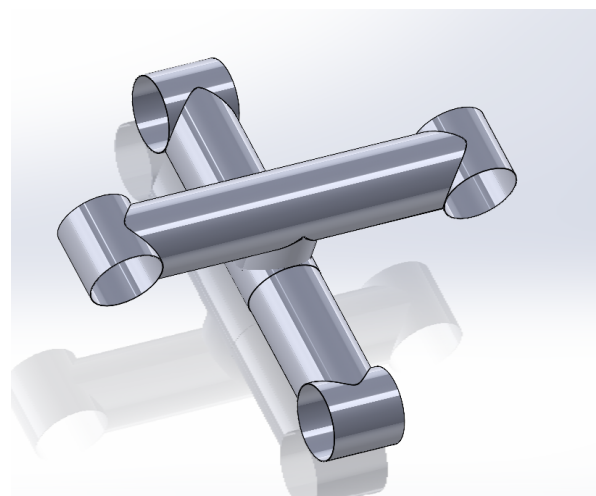
7.1.4. Articulation and Rotation Mechanisms

X-array topologies require an additional rotational articulation mechanism to transition the booms from a stowed linear alignment into the final X-shaped deployed configuration. This mechanism is represented by two rigid parts joined by a central rotational axis, as shown

in Figure 7.8. In the finite element model, this joint is treated as a stiff rotational interface, approximating the behavior of a real-world articulation mechanism.



Stowed configuration



Deployed configuration

Figure 7.8: Simplified articulation and rotation mechanism: stowed and deployed

7.2. Linear Configurations

The linear configurations evaluated in this study are based on the Linear Dual Chopped Bracewell (DCB) topology introduced in Chapter 2. Each design places four telescopes along a single axis, connected via deployable or rigid booms. Three configurations are considered: Lin8, Lin16, and Lin32, representing increasing baseline lengths of 8 m, 16 m, and 32 m, respectively. While Lin8 requires no deployment and serves as the stowed baseline layout, Lin16 and Lin32 rely on telescopic mechanisms to achieve their extended baselines post-launch. This section presents the finalized structural layouts of these configurations.

7.2.1. Lin8

Figure 7.9 shows the final Lin8 spacecraft configuration in both the stowed state with the fairing and the isolated view without it. This design requires no deployment mechanisms, as all four telescopes are mounted directly to the central spacecraft body via two non-deployable booms which combined have a weight of 26.25 kg. As discussed in Chapter 5, the Lin8 configuration forms the basis for evaluating stowage feasibility of more complex topologies, since its geometric layout is reused in the stowed condition for all larger designs. Through iterative modal analysis, an outer boom diameter of 160 mm was selected to ensure the required minimum first natural frequency of 2 Hz set in section 4.2. The

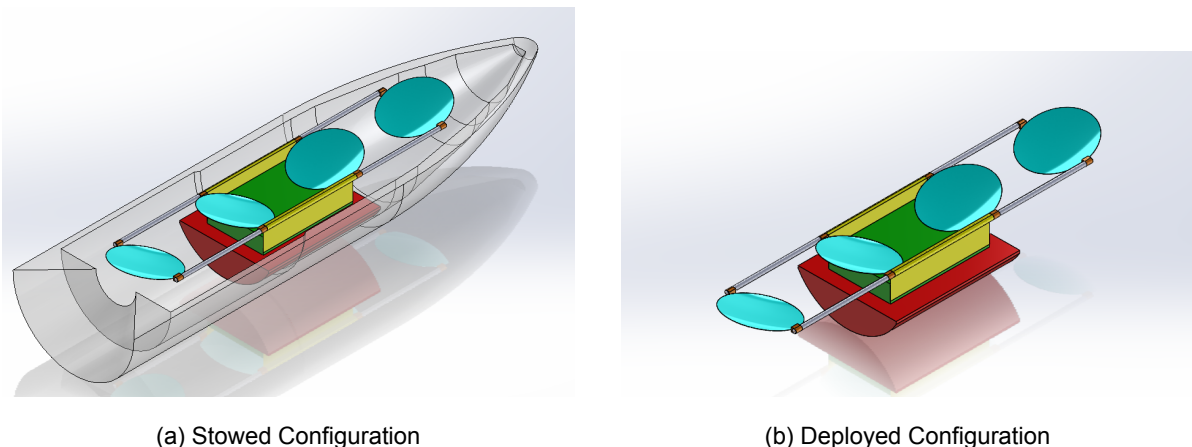


Figure 7.9: Lin8 spacecraft configuration in its stowed and deployed states designed for a 2 Hz fundamental frequency

7.2.2. Lin16

The Lin16 configuration, shown in Figure 7.10, builds upon the same structural layout as Lin8 but introduces two deployable booms of different lengths to increase the baseline to 16 m. This longer baseline enhances interferometric performance by improving angular resolution and reducing the inner working angle (IWA), as described in Chapter 2. However, the increased deployment length introduces additional mass and stiffness constraints that must be managed through design optimization. To ensure that the deployed structure still meets the first natural frequency requirement of 2 Hz, a larger outer diameter of 420 mm was selected for both the 4 m and 8 m telescopic booms, composed of two sections, used in this configuration. The eight telescopic booms have a total weight of 137.644 kg. These diameters were determined through successive modal simulations which will be discussed in Chapter 8. The

fairing-bound geometry confirms that deployment is necessary, as the fully deployed layout would not otherwise fit within the Ariane 6 volume constraints.

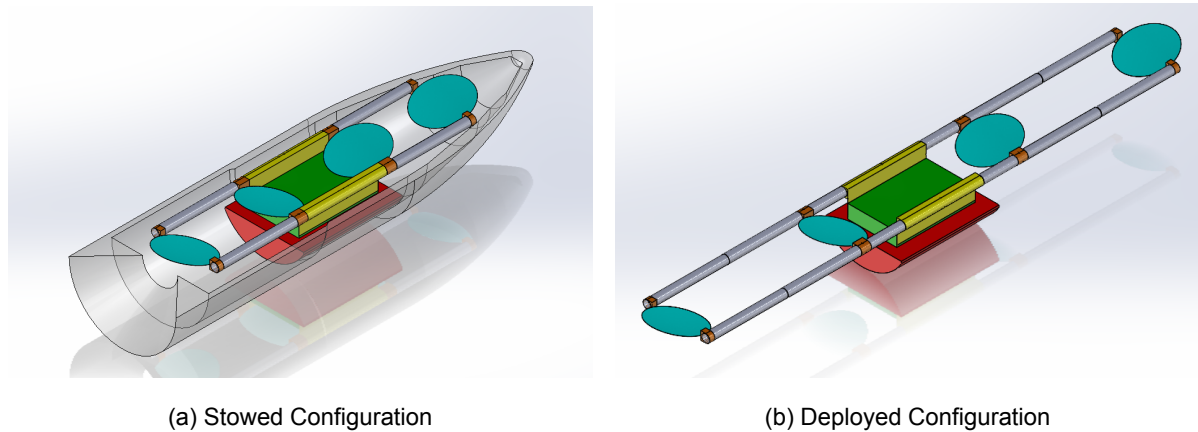


Figure 7.10: Lin16 spacecraft configuration in its stowed and deployed states designed for a 2 Hz fundamental frequency

7.2.3. Lin32

The Lin32 configuration is the largest of the linear designs and utilizes the full capacity of the Ariane 6 fairing envelope. Figure 7.11 shows the configuration in the stowed and deployed configuration. To achieve a total deployed baseline of 32 m, this design includes two long telescopic mechanisms, 8 m and 16 m in length, each composed of four nested segments.

The outer diameter of these booms was increased to 620 mm to maximize structural stiffness while remaining within the fairing's allowable internal diameter at the tapered section. This is the largest boom diameter considered in this study that still satisfies volume constraints in the stowed configuration. The eight telescopic booms have a net weight of 401.87 kg. Unlike Lin8 and Lin16, this design was not tuned to a target frequency of 2 Hz, but instead optimized for maximum fairing diameter utilization while stowed.

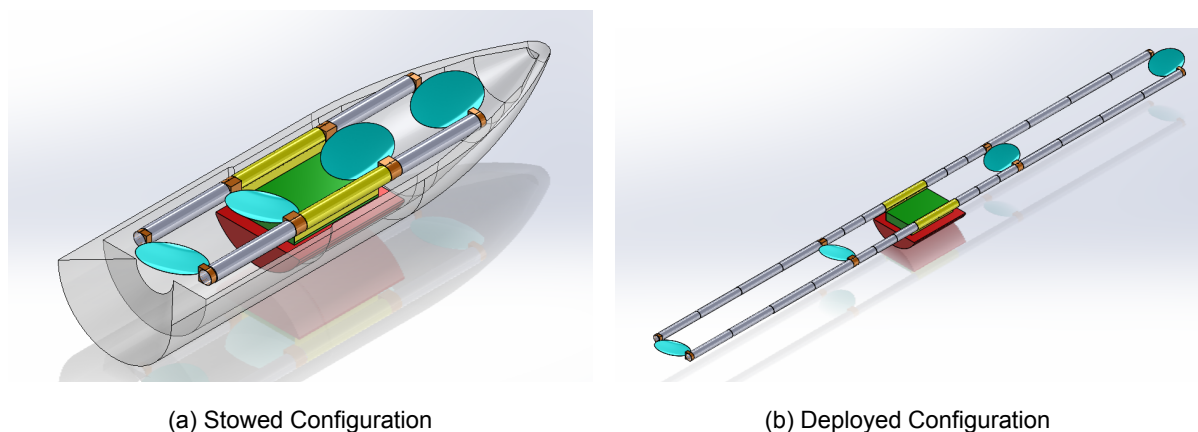


Figure 7.11: Lin32 in its stowed and deployed states designed for full fairing diameter utilization

7.3. X-array Configurations

The X-array configuration refers to a layout in which the four telescopes are positioned symmetrically around the central beam combiner in an 'X'-shaped pattern. Similar to the linear topologies, three variants are evaluated: X8, X16, and X32, corresponding to increasing interferometric baselines of 8 m, 16 m, and 32 m. Unlike the linear variants, every X-array topology requires an articulation mechanism to rotate the booms from their stowed configuration into the final deployed 'X' formation. Depending on the required baseline, telescopic mechanisms are added to extend the booms post-launch.

7.3.1. X8

Figure 7.12 presents the final design of the X8 spacecraft in both stowed and deployed states. In the stowed configuration (a), the system follows the same layout as the Lin8 topology, with all booms aligned along the longitudinal axis. After launch, the deployment involves only the rotational articulation mechanism (as introduced in Figure 7.8), rotating the booms into the final X-formation shown in (b). This transformation is required to ensure compatibility with the fairing during launch.

Unlike the Lin8 configuration, which uses long non-deployable booms, the X8 utilizes single-piece booms to span a baseline of 8 m with a 4 m distance between telescopes. Due to the more compact and centrally balanced distribution of mass in the X-layout, a smaller outer boom diameter of 134 mm was sufficient to achieve a fundamental natural frequency of 2 Hz, as determined through iterative modal analysis. The booms together with the structure used for rotation have a net weight of 57.63 kg.

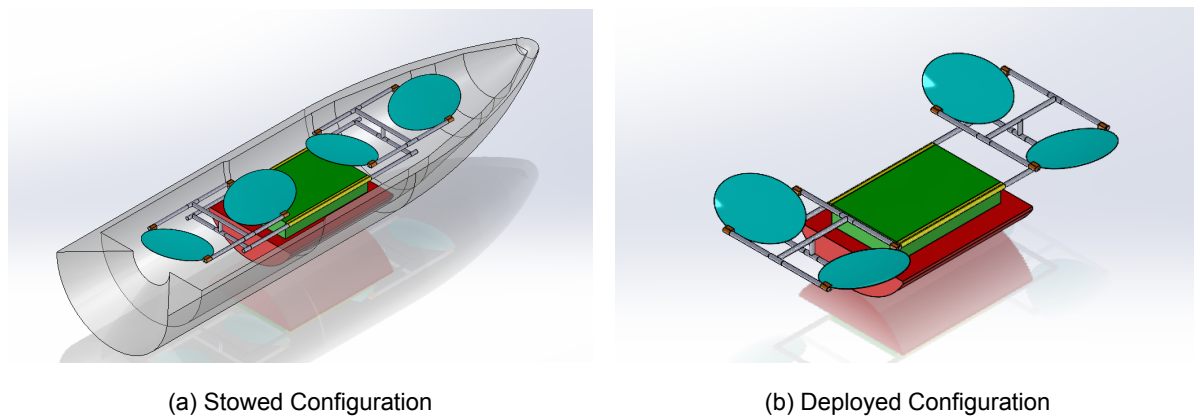


Figure 7.12: X8 spacecraft configuration in its stowed and deployed states designed for a 2 Hz fundamental frequency

7.3.2. X16

The X16 spacecraft builds upon the same X-array layout as X8 but requires both articulation and telescopic deployment to achieve a 16 m baseline. As shown in Figure 7.13, the spacecraft is shown in its stowed and deployed state using both rotation and two telescopic mechanisms: one extending to 4 m and the other to 8 m. Each mechanism consists of two nested sections, consistent with the designs detailed in Section 7.1.

Through iterative modal analysis, the telescopic booms for this configuration were assigned

an initial outer diameter of 362 mm, ensuring that the first natural frequency in the deployed state reaches the 2 Hz target. This result highlights the trade-off between increased deployed length and required structural stiffness, which is reflected in the larger diameter compared to the X8 configuration. The telescopic booms together with the structure used for rotation have a net weight of 250.50 kg.

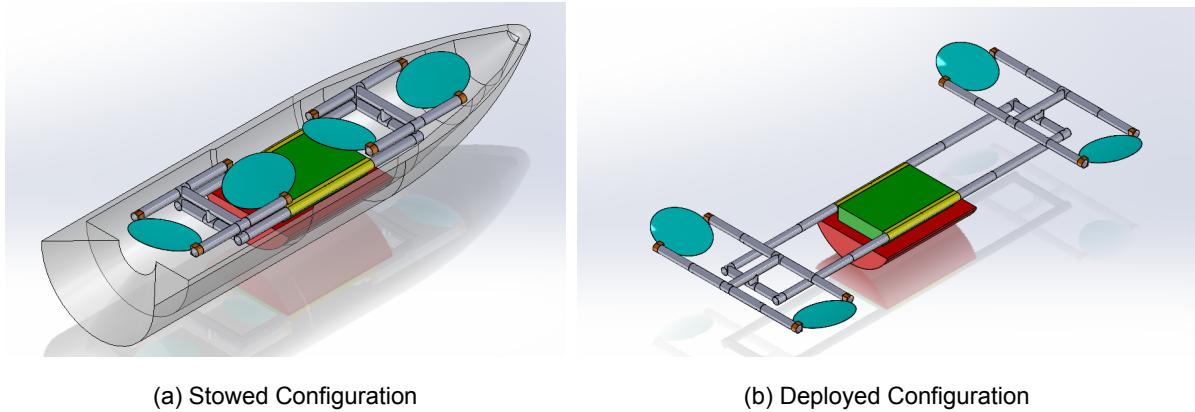


Figure 7.13: X16 spacecraft configuration in its stowed and deployed states designed for a 2 Hz fundamental frequency

7.3.3. X32

The X32 configuration represents the largest and most structurally complex of the X-array designs. When stowed, it maximizes the usable diameter of the Ariane 6 fairing, particularly in the tapered conical region. Figure 7.14 illustrates the spacecraft in its stowed and deployed state. To realize a 32 m interferometric baseline, the design employs two telescopic booms extending to 8 m and 16 m, each composed of four nested sections.

Unlike the X8 and X16 configurations, the X32 design was not tuned to achieve a specific natural frequency target. Instead, the design aimed to utilize the full fairing diameter. Consequently, the outer diameter of the telescopic booms was increased to 620 mm, the maximum that fits within the fairing without intersecting the tapered section while stowed. The telescopic booms together with the structure used for rotation have a net weight of 940.899 kg.

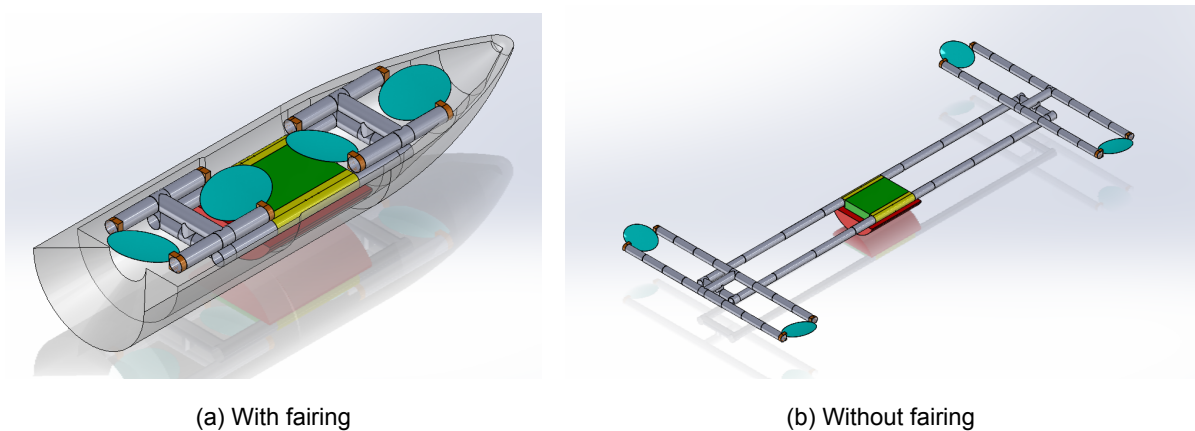
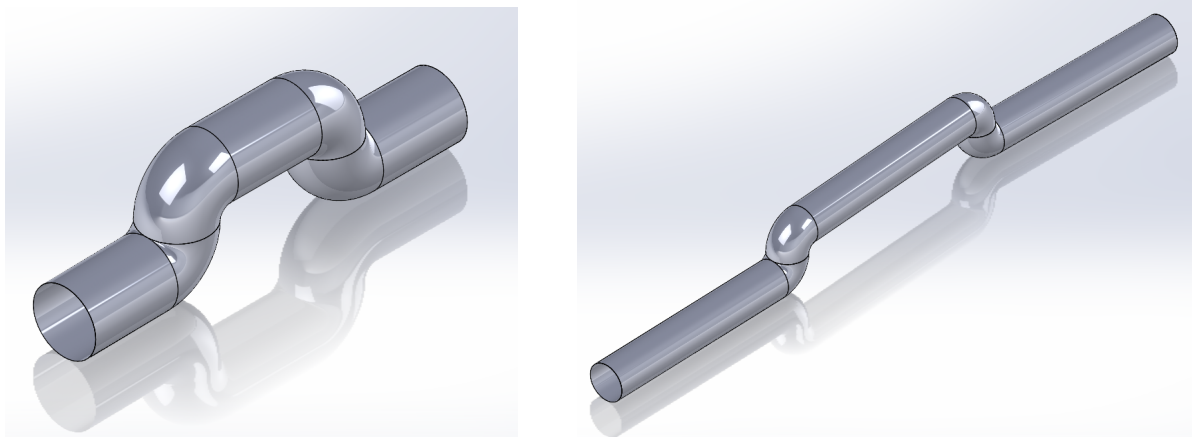


Figure 7.14: X32 spacecraft configuration in its stowed and deployed states designed for full fairing diameter utilization

7.4. Articulated Lin16

Resulting from the trade-off conducted in Chapter 5, articulated deployment would serve as a fallback option in case the telescopic booms fall short in performance. To showcase what a possible articulated version could look like, in this case for the Lin16 topology, a simplified version of the spacecraft was designed. It uses articulation mechanisms with deployed lengths of 4 and 8 meters and an outer diameter of 420 mm, just like the telescopic Lin16 spacecraft (figure 7.10). Each articulation mechanism consists of two articulation points and three booms. These articulation mechanisms are shown in Figure 7.15.

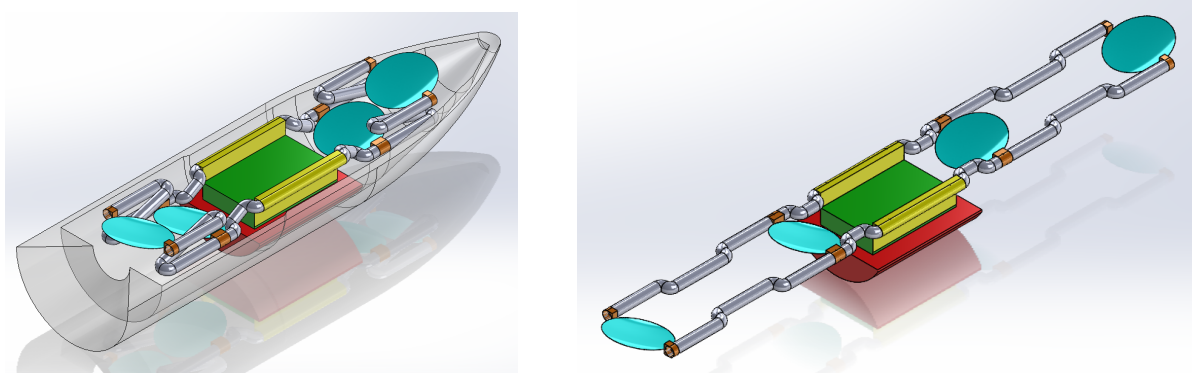


(a) 4m Articulated Boom

(b) 8m Articulated Boom

Figure 7.15: Articulation mechanisms used in the articulated Lin16 spacecraft

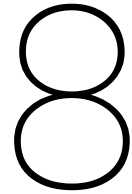
The stowed and deployed configurations of the articulated Lin16 spacecraft are shown in Figure 7.16. These images illustrate how the spacecraft would extend outward from its stowed position by rotating its booms. In the stowed position, it is clear why articulated mechanisms have such a poor packing ratio and were therefore not chosen as the primary deployment mechanism for further study and use in the nulling interferometer spacecraft. To properly stow the spacecraft, the booms must fold inward into a Z-shaped position. This layout uses significantly more fairing volume and leaves less space for stowing the sunshield underneath the structure.



(a) Stowed configuration

(b) Deployed configuration

Figure 7.16: Articulated Lin16 spacecraft configuration in its stowed and deployed states



Structural Dynamics and Stability Analysis

To ensure optimal nulling interferometry performance, each spacecraft topology must minimize dynamic disturbances that introduce optical path length errors. One key design constraint is derived from the isolator assembly used on the James Webb Space Telescope (JWST), which introduces a bounce mode at approximately 1 Hz. Such an isolator assembly is proposed for all spacecraft topologies to provide a predictable boundary condition between the spacecraft bus and the boom structure. Without this isolation, disturbance frequencies from individual spacecraft components (e.g., reaction wheels, cryocoolers) would couple directly into the optical system via the booms, degrading performance. This modal requirement is therefore critical to preserving the optical path stability necessary for successful nulling interferometry. To sufficiently isolate this mode from the structural dynamics of the spacecraft, a minimum fundamental natural frequency of 2 Hz is targeted for all designs. This ensures vibrational disturbances from the bus are not amplified through resonance in the deployable structure.

All structural simulations were conducted using **ANSYS Mechanical**, a commercial finite element analysis (FEA) software widely used in aerospace engineering for structural, thermal, and dynamic simulations. In this study, ANSYS was used to assess the structural dynamics and stability of each spacecraft topology via three core analyses:

- **Modal Analysis:** To extract the natural frequencies and corresponding mode shapes of each configuration. This identifies the dynamic response of the structure and confirms whether the 2 Hz requirement is met.
- **Static Structural Analysis:** A 1 N point load was applied to the tips of each spacecraft to determine the resulting deformation. The resulting deflection serves as a secondary measure of structural stiffness and complements the modal analysis results.
- **Eigenvalue Buckling Analysis:** To estimate the critical buckling load for each topology when subjected to axial loading. This analysis was conducted on the deployed structure. While no reference requirement was available for direct comparison, the obtained values can serve as early input once buckling criteria are established in future work. It should

be noted that the critical loads determined for the deployed structures are lower than what would be expected for the stowed configurations, except in the case of the Lin8 and X8 topologies, where the deployed and stowed lengths are equivalent.

For each topology, a modal analysis was conducted on (i) a boom structure designed to achieve a 2 Hz first natural frequency, and (ii) a maximum-volume configuration, which assumes fully filled circular booms within the stowage envelope to estimate upper bounds on vibrational performance. These booms have an outer diameter of 620 mm. The first six natural frequencies and corresponding mode shapes are reported for each configuration, along with tip stiffness and buckling limits to provide a complete view of each design's structural dynamics.

In all analyses, a fixed boundary condition was applied at the boom-to-beam combiner interface to represent the connection to the central spacecraft bus. Each telescope was modeled with an approximate mass of 750 kg, distributed at their respective locations on the boom structure. To approximate the additional structural rigidity and damping that would realistically be introduced at the interfaces between the boom structure and the telescope, for example through clamping mechanisms, structural joints, and interface hardware, the telescopes were modeled with a material stiffness approximately 100 times greater than that of the boom material. This simplification accounts for the effect of these very stiff and potentially lightly damping connections, which help attenuate vibrations transferred from the booms to the telescopes.

This approach ensures the telescopes act as quasi-rigid bodies, reducing their dynamic coupling with the boom and better representing the intended mechanical behavior of the integrated system.

8.1. Linear Configurations

8.1.1. Lin8 – Designed for 2 Hz Fundamental Frequency

The first and second mode shapes of the Lin8 spacecraft (see Figure 8.1) exhibit bending about the x-axis, resulting in lateral deflection in the y-direction. Conversely, Modes 3 and 4 show bending around the y-axis with corresponding deflection in the x-direction. Notably, in all four cases, only one side of the spacecraft undergoes significant deformation, indicating asymmetric modal behavior possibly driven by mass or stiffness distribution.

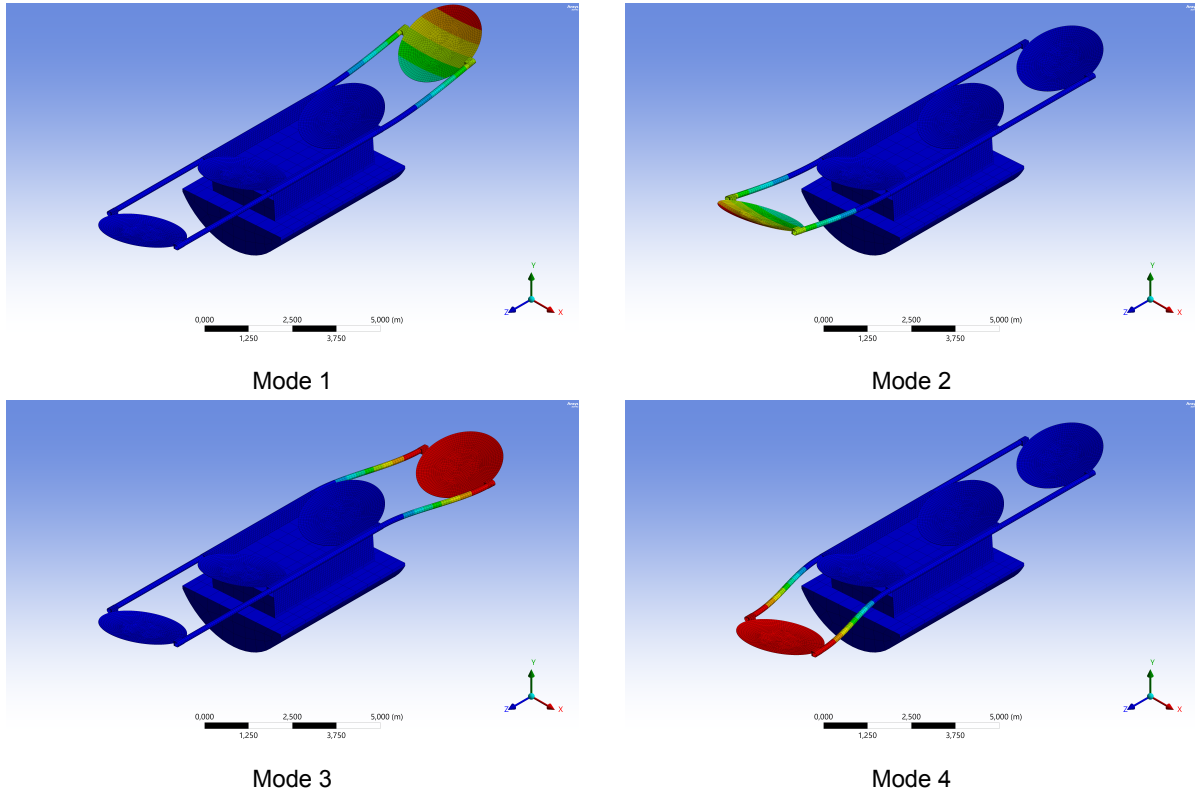


Figure 8.1: First four mode shapes of the Lin8 spacecraft designed for a 2 Hz fundamental frequency

The corresponding modal frequencies are shown in Table 8.1, where the fundamental frequency of 2.055 Hz satisfies the system constraint.

Mode	1	2	3	4	5	6
Frequency (Hz)	2.055	2.056	4.6171	4.6223	10.578	10.596

Table 8.1: Natural frequency values for the Lin8 spacecraft designed for a 2 Hz fundamental frequency (first 6 modes)

Structural performance results in Table 8.2 indicate a maximum static deflection of $9.05 \mu\text{m}$ under a 1 N load, which translates to a stiffness of $1.106 \times 10^5 \text{ N/m}$. The linear buckling load is approximately $2.14 \times 10^6 \text{ N}$.

Parameter	Value
Max Deflection [m]	9.0462×10^{-6}
Stiffness [N/m]	1.106×10^5
Buckling Load [N]	2.1432×10^6
Structure Weight [Kg]	26.25

Table 8.2: Structural performance of L8 topology

8.1.2. Lin8 – Maximum Volume Configuration

The mode shapes of the maximum volume variant (Figure 8.2) exhibit smooth C-shaped and S-shaped bending around both principal axes, indicating a more symmetric and stiff behavior. These shapes are associated with higher bending stiffness and evenly distributed structural inertia.

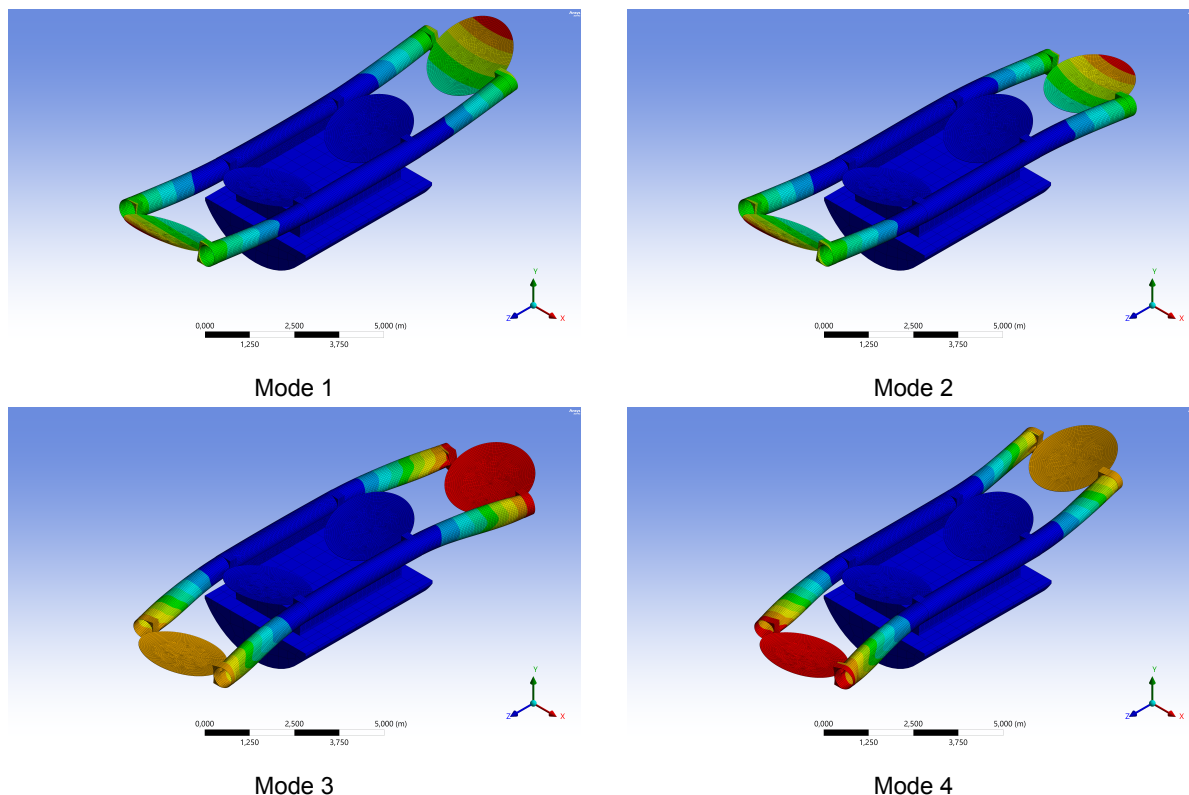


Figure 8.2: First four mode shapes of the Lin8 spacecraft in the maximum volume configuration

As summarized in Table 8.3, all six frequencies are significantly higher compared to the 2 Hz design, confirming the gain in dynamic performance due to increased boom diameter and overall stiffness.

Mode	1	2	3	4	5	6
Frequency (Hz)	13.387	13.566	18.302	18.544	32.502	33.206

Table 8.3: Natural frequency values for the Lin8 spacecraft in the maximum volume configuration (first 6 modes)

Table 8.4 further confirms the structural gains. The maximum deflection is reduced by two orders of magnitude, yielding a stiffness of 5.486×10^6 N/m, and the buckling load increases to 3.47×10^6 N.

Parameter	Value
Max Deflection [m]	1.8233×10^{-7}
Stiffness [N/m]	5.486×10^6
Buckling Load [N]	3.4709×10^6
Structure Weight [Kg]	102.21

Table 8.4: Structural performance of L8 Max Volume topology

In summary, Figures 8.1 and 8.2 together illustrate the range of deformation behavior expected across the design envelope for Lin8. The results in Tables 8.1–8.4 present a clear trade-off: the 2 Hz design achieves compact stowage but with limited stiffness, while the maximum volume variant offers vastly improved structural metrics at the cost of increased packaging complexity. These results define the feasible design envelope for the Lin8 topology.

8.1.3. Lin16 – Designed for 2 Hz Fundamental Frequency

The first four mode shapes of the Lin16 spacecraft, shown in Figure 8.3, demonstrate smooth C- and S-shaped bending patterns. Modes 1 and 3 form C-shapes, while Modes 2 and 4 take on S-shaped responses. These shapes bend around the x -axis (deflecting in y) and around the y -axis (deflecting in x), similar to the modal behavior observed in the Lin8 design. The consistent axis behavior is expected, as Lin16 is a longer variant of the same boom-based configuration.

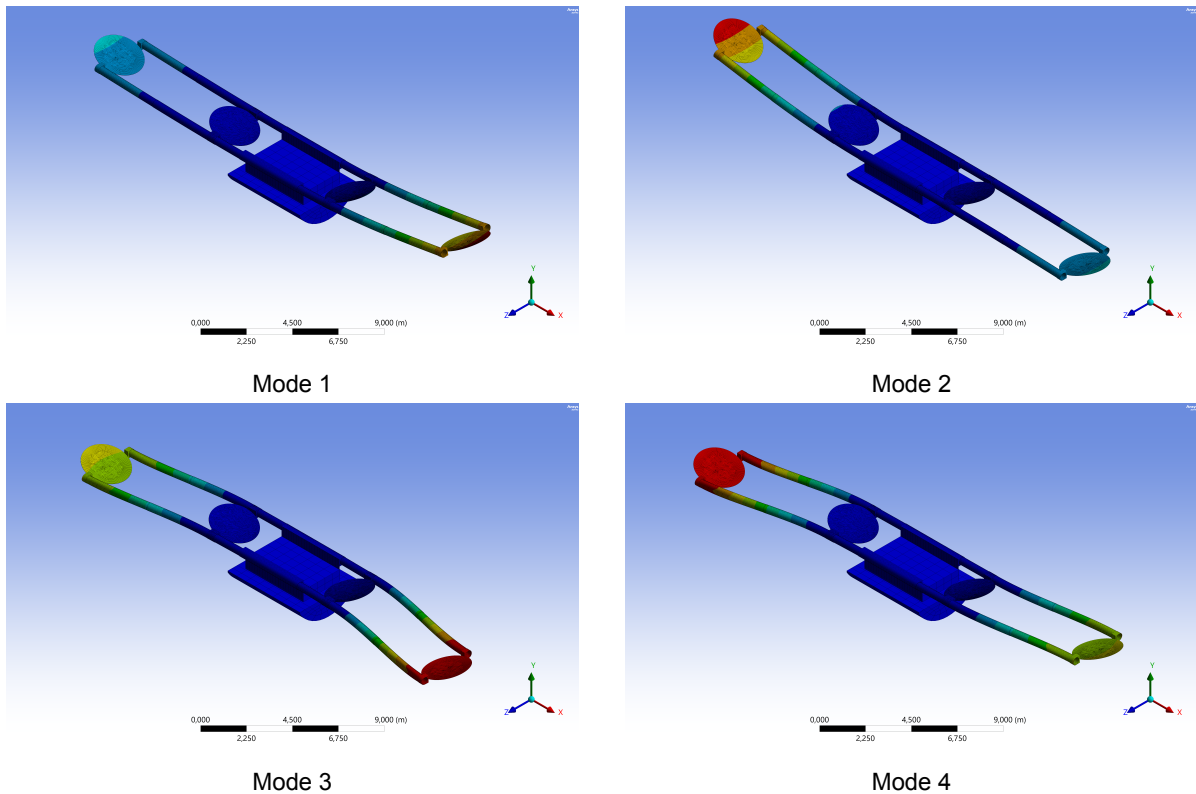


Figure 8.3: First four mode shapes of the Lin16 spacecraft designed for a 2 Hz fundamental frequency

Table 8.5 presents the corresponding modal frequencies. The fundamental mode is 2.0452 Hz, slightly above the 2 Hz requirement.

Mode	1	2	3	4	5	6
Frequency (Hz)	2.0452	2.0454	5.2527	5.2528	15.236	15.237

Table 8.5: Natural frequency values for the Lin16 spacecraft designed for a 2 Hz fundamental frequency (first 6 modes)

Table 8.6 shows the maximum static deflection under 1 N is $7.56 \mu\text{m}$, yielding a stiffness of $1.324 \times 10^5 \text{ N/m}$. Buckling resistance is somewhat lower than Lin8 due to the increased length, resulting in a critical load of $1.2842 \times 10^6 \text{ N}$.

Parameter	Value
Max Deflection [m]	7.5566×10^{-6}
Stiffness [N/m]	1.324×10^5
Buckling Load [N]	1.2842×10^6
Structure Weight [Kg]	137.64

Table 8.6: Structural performance of L16 topology

8.1.4. Lin16 – Maximum Volume Configuration

The first and second mode shapes of the maximum volume configuration, shown in Figure 8.4, still exhibit symmetric C- and S-shaped bending like the 2 Hz version. However, the third and fourth modes now display asymmetric bending behavior, where only one side of the spacecraft deflects, behavior that closely resembles the Lin8 2 Hz configuration.

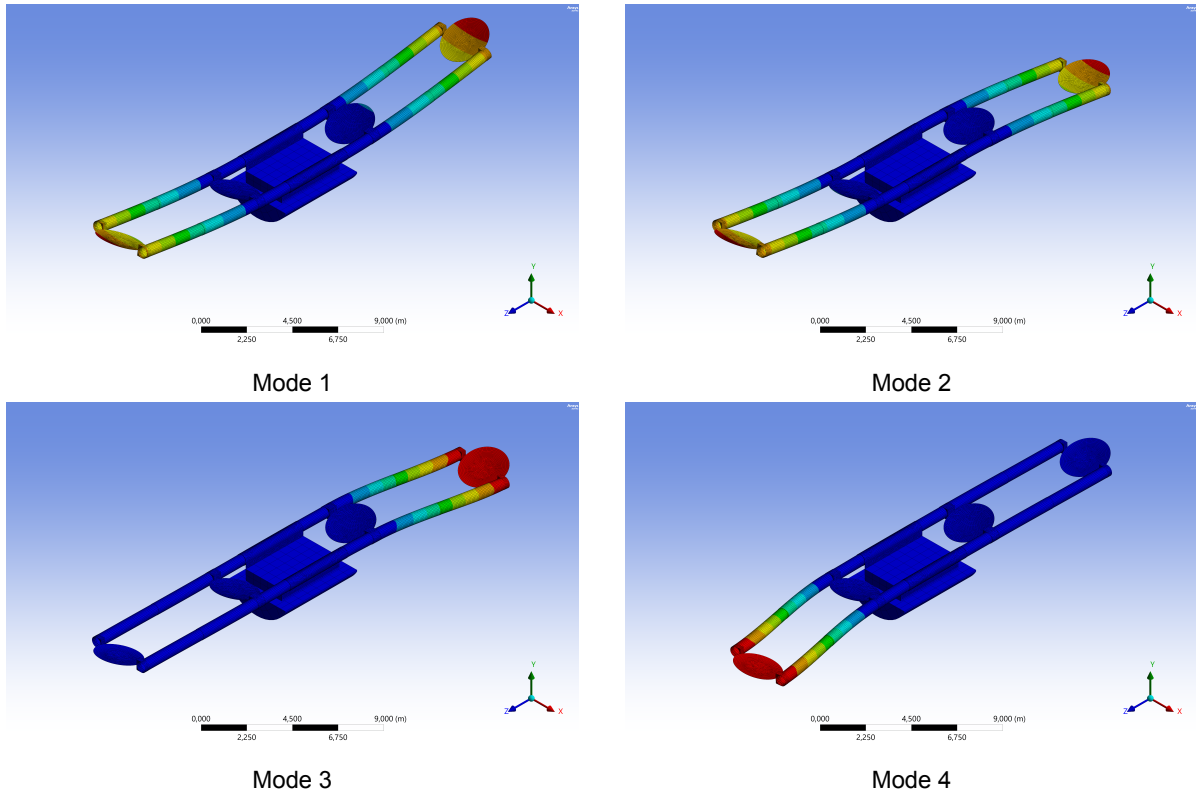


Figure 8.4: First four mode shapes of the Lin16 spacecraft in the maximum volume configuration

The natural frequencies listed in Table 8.7 are significantly higher than in the 2 Hz configuration; however, the increase is not as pronounced as the difference observed between the Lin8 variants. This is because the Lin16 2 Hz design already required a considerably larger outer diameter to meet the frequency constraint, leaving less room for further stiffness gains through diameter increase. As a result, the achievable improvement in modal performance from the maximum volume configuration is more limited. Still, the fundamental mode reaches 3.57 Hz, and the subsequent modes follow this trend, indicating a stiffer and more compact vibrational response.

Mode	1	2	3	4	5	6
Frequency (Hz)	3.5747	3.5866	8.2606	8.3069	21.355	22.806

Table 8.7: Natural frequency values for the Lin16 spacecraft in the maximum volume configuration (first 6 modes)

Table 8.8 confirms improved structural characteristics. The maximum deflection drops to $2.73 \mu\text{m}$, yielding a much higher stiffness of $3.660 \times 10^5 \text{ N/m}$, and the buckling load more than

doubles to 3.6765×10^6 N. This demonstrates the benefit of thicker booms and higher volume for structural robustness, albeit at the cost of increased stowage volume and mass.

Parameter	Value
Max Deflection [m]	2.733×10^{-6}
Stiffness [N/m]	3.660×10^5
Buckling Load [N]	3.6765×10^6
Structure Weight [Kg]	204.46

Table 8.8: Structural performance of L16 Max Volume topology

Together, Figures 8.3 and 8.4 highlight the difference in vibrational symmetry and deformation modes, while Tables 8.5 through 8.8 clearly present the structural trade-offs. These results define the design envelope for the Lin16 topology.

8.1.5. Lin32

The first four mode shapes of the Lin32 spacecraft are shown in Figure 8.5. Each mode exhibits bending on only one side of the spacecraft, similar to the asymmetrical modal behavior observed in the Lin8 2 Hz and Lin16 Max Volume configurations. The bending and corresponding deflection occur about the same principal axes as in the other linear variants around the x-axis for deflection in y, and around the y-axis for deflection in x.

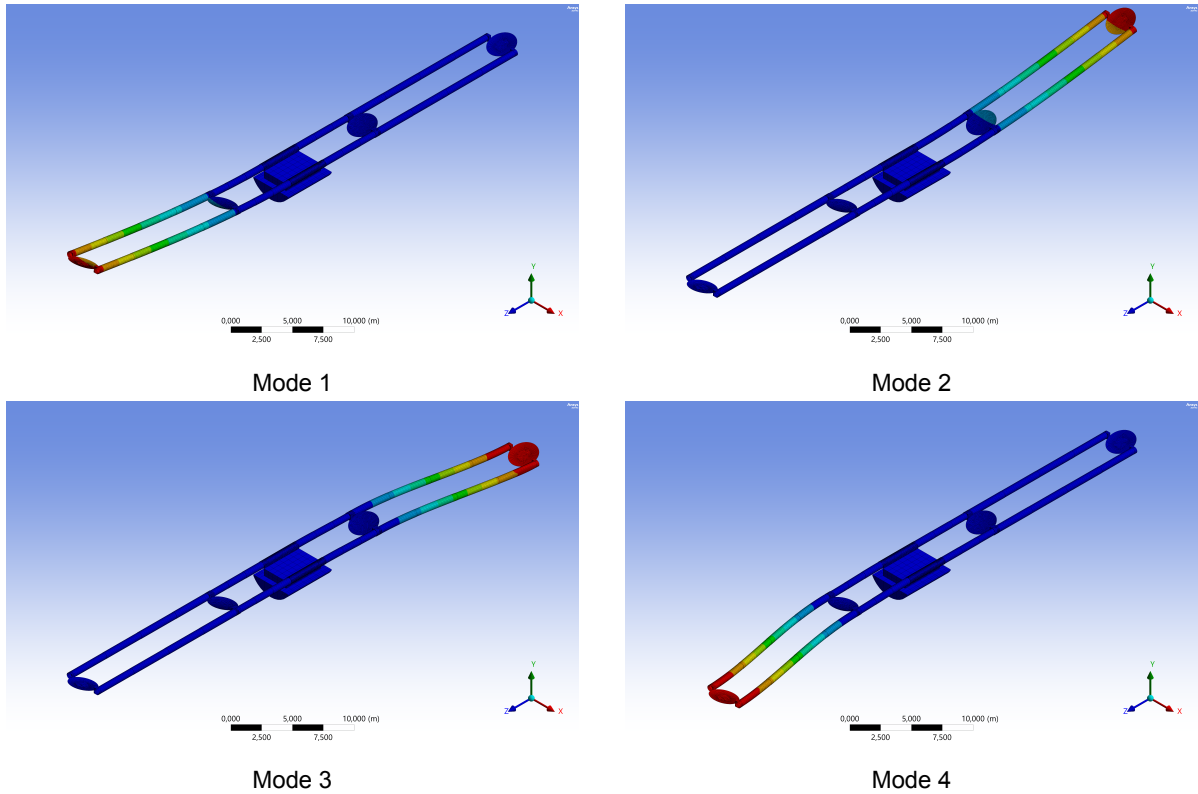


Figure 8.5: First four mode shapes of the Lin32 spacecraft

The corresponding natural frequencies are presented in Table 8.9. Notably, the fundamental mode reaches only 1.0676 Hz, failing to meet the 2 Hz requirement. Despite this, the outer diameter of the booms was already maximized within the available fairing constraints, leaving no room to further improve the stiffness without exceeding fairing diameter constraints.

Mode	1	2	3	4	5	6
Frequency (Hz)	1.0676	1.0676	2.9212	2.9397	9.4360	9.4376

Table 8.9: Natural frequency values for the Lin32 spacecraft (first 6 modes)

The structural performance is summarized in Table 8.10. The increased boom length leads to a relatively large maximum deflection of 2.42×10^{-5} m under a 1 N load, corresponding to a stiffness of only 4.138×10^4 N/m. The buckling load is also the lowest among the linear configurations, at 8.4364×10^5 N, further highlighting the structural limitations imposed by this extended baseline.

Parameter	Value
Max Deflection [m]	2.4171×10^{-5}
Stiffness [N/m]	4.138×10^4
Buckling Load [N]	8.4364×10^5
Structure Weight [Kg]	401.87

Table 8.10: Structural performance of L32 topology

In summary, while the Lin32 topology offers the longest interferometric baseline among the linear configurations, its dynamic and structural performance is constrained by geometric limitations. The failure to reach the 2 Hz target, despite maximizing the outer boom diameter, underscores the importance of researching alternate structural layouts when long baselines are required within strict launch constraints.

8.2. X-array Configurations

8.2.1. X8

8.2.1.1. X8 – Designed for 2 Hz Fundamental Frequency

The first four mode shapes of the X8 spacecraft are presented in Figure 8.6. Modes 1 and 2 exhibit bending along the x-axis, resulting in y-direction deflections. These occur exclusively in the booms connecting the two telescopes on the same arm, not in the booms linking the telescopes to the spacecraft bus or beam combiner. Modes 3 and 4, in contrast, involve bending around the global z-axis with deflection again in the y-direction. These modes primarily excite the booms connecting the telescopes to the central spacecraft body. This behavior is effectively equivalent to bending around the x-axis in the linear topologies, due to a 90-degree rotation in the local coordinate frame during the ANSYS setup.

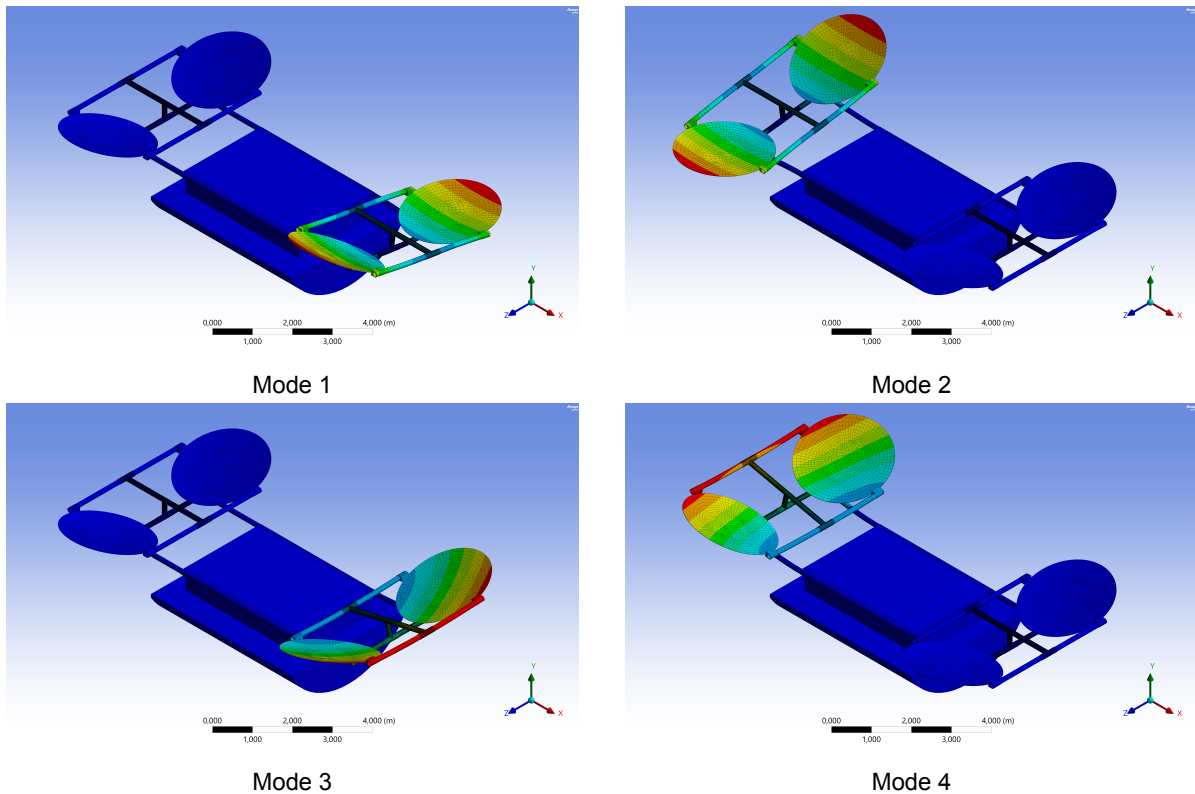


Figure 8.6: First four mode shapes of the X8 spacecraft designed for a 2 Hz fundamental frequency

Table 8.11 lists the modal frequencies. The first two modes just exceed the 2 Hz threshold, reaching 2.0173 and 2.0181 Hz respectively.

Mode	1	2	3	4	5	6
Frequency (Hz)	2.0173	2.0181	2.1616	2.1625	3.7531	3.7543

Table 8.11: Natural frequency values for the X8 spacecraft designed for a 2 Hz fundamental frequency (first 6 modes)

As seen in Table 8.12, the X8 design offers a good structural trade-off, with a stiffness of

$2.37 \times 10^5 \text{ N/m}$ under 1 N loading and maximum deflection of $4.22 \mu\text{m}$. Buckling behavior was evaluated in both the x- and z-directions, with loads of $1.33 \times 10^5 \text{ N}$ and $2.39 \times 10^5 \text{ N}$, respectively.

Parameter	Value
Max Deflection [m]	4.217×10^{-6}
Stiffness [N/m]	2.370×10^5
Buckling Load (X-dir) [N]	1.333×10^5
Buckling Load (Z-dir) [N]	2.3889×10^5
Structure Weight [Kg]	57.63

Table 8.12: Structural performance of X8 topology

8.2.1.2. X8 – Maximum Volume Configuration

The mode shapes of the maximum volume variant are shown in Figure 8.7. The same general bending patterns are observed as in the 2 Hz design: the first two modes exhibit bending in the boom connecting the telescopes on one arm, while the third and fourth modes correspond to flexing of the structure between the spacecraft and telescope assemblies.

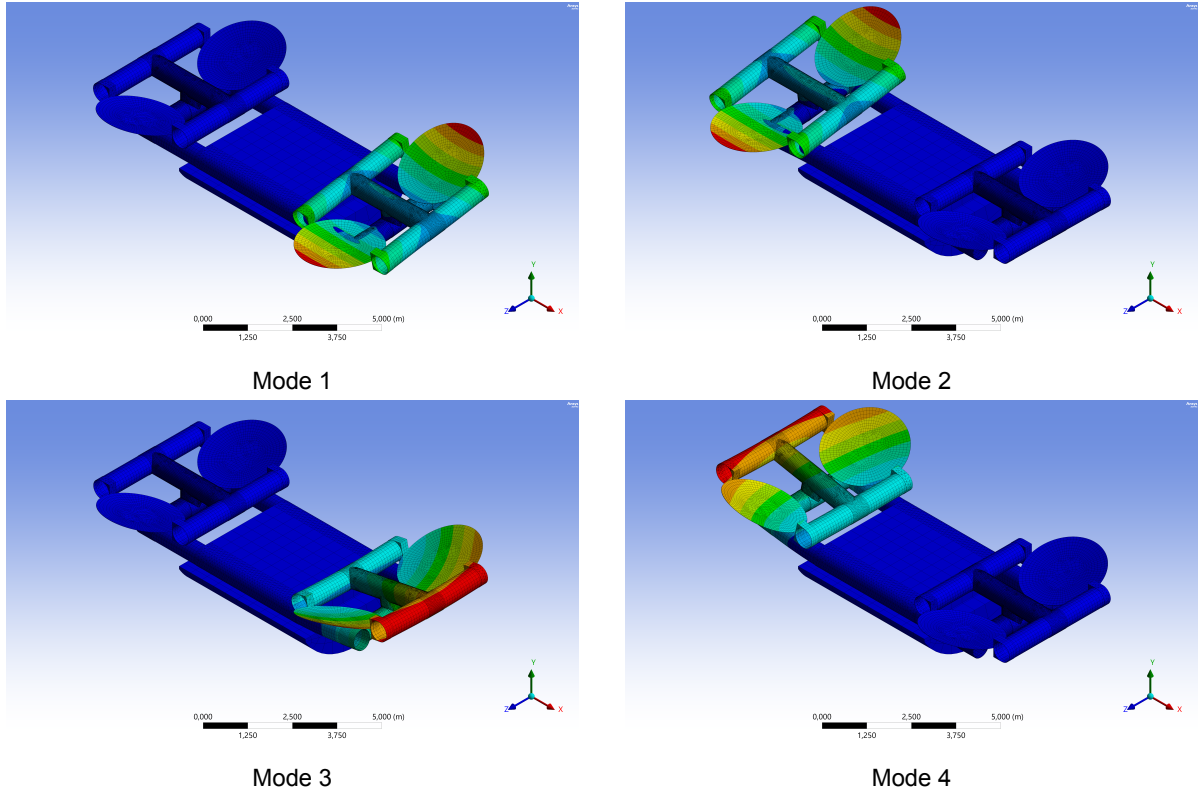


Figure 8.7: First four mode shapes of the X8 spacecraft in the maximum volume configuration

As listed in Table 8.13, the modal frequencies increase dramatically. The fundamental frequency rises to 15.97 Hz, with the first through fourth modes clustered around 16–17 Hz.

Mode	1	2	3	4	5	6
Frequency (Hz)	15.966	16.014	17.224	17.257	27.967	27.976

Table 8.13: Natural frequency values for the X8 spacecraft in the maximum volume configuration (first 6 modes)

The results in Table 8.14 highlight the structural robustness of this configuration. The maximum deflection under a 1 N load is reduced by nearly two orders of magnitude to 55.9 nm, corresponding to a stiffness of 1.79×10^7 N/m. Buckling loads also increase significantly, reaching 1.14×10^6 N in the x-direction and 5.61×10^5 N in the z-direction.

Parameter	Value
Max Deflection [m]	5.5876×10^{-8}
Stiffness [N/m]	1.790×10^7
Buckling Load (X-dir) [N]	1.136×10^6
Buckling Load (Z-dir) [N]	5.6144×10^5
Structure Weight [Kg]	325.98

Table 8.14: Structural performance of X8 Max Volume topology

In conclusion, the X8 topology offers strong dynamic and structural performance even in the compact 2 Hz configuration, with significant structural gains possible in the maximum volume variant.

8.2.2. X16

8.2.2.1. X16 – Designed for 2 Hz Fundamental Frequency

The first four mode shapes of the X16 spacecraft are shown in Figure 8.8. As with the X8 configuration, the first and second modes display bending along the x-axis with deflection in the y-direction. These deformations are localized to the boom structure connecting the two telescopes on a single arm. Again, only one side of the spacecraft deflects significantly per mode. Modes 3 and 4 involve bending around the z-axis with continued deflection in the y-direction. These deformations occur primarily in the booms linking the telescope assemblies to the spacecraft bus and beam combiner.

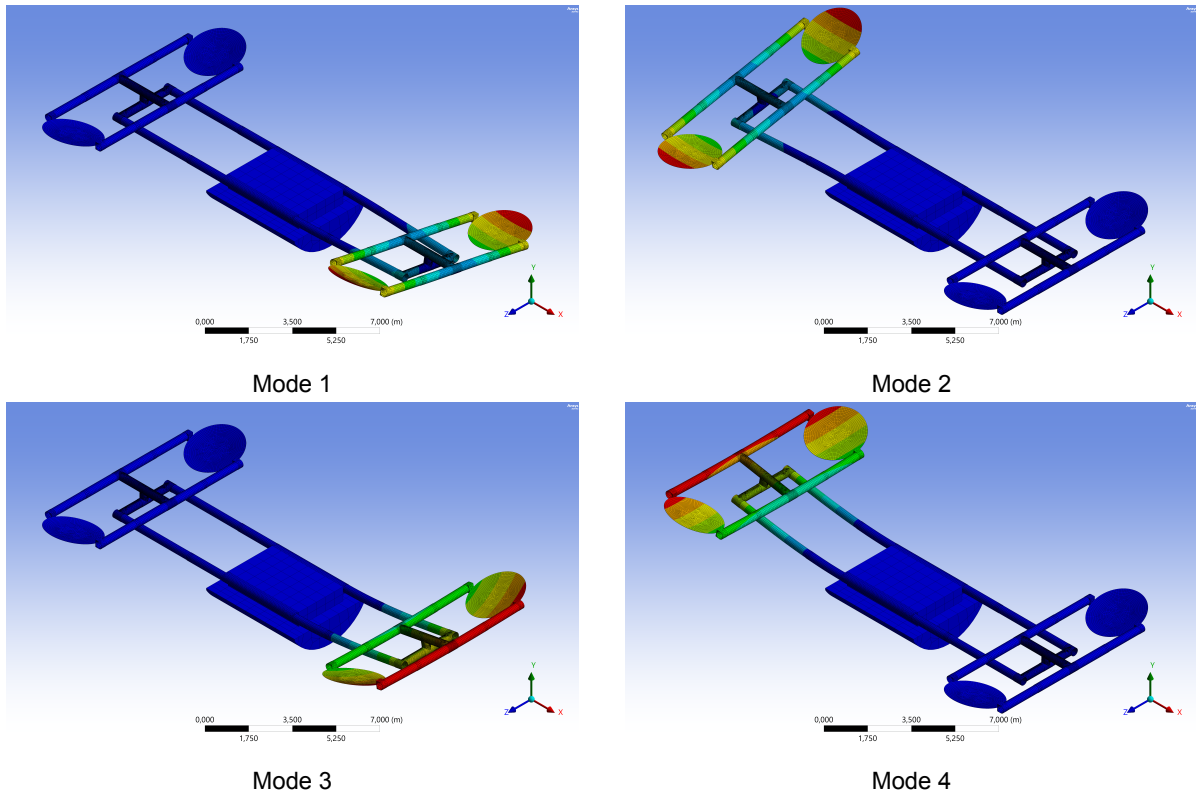


Figure 8.8: First four mode shapes of the X16 spacecraft designed for a 2 Hz fundamental frequency

Table 8.15 lists the modal frequencies for the 2 Hz configuration. The first two modes meet the system requirement, with frequencies just above 2 Hz. The next two modes occur around 2.24 Hz, consistent with behavior seen across all X-array topologies.

Mode	1	2	3	4	5	6
Frequency (Hz)	2.0061	2.0107	2.2381	2.2381	4.1158	4.1470

Table 8.15: Natural frequency values for the X16 spacecraft designed for a 2 Hz fundamental frequency (first 6 modes)

As presented in Table 8.16, the X16 configuration achieves a moderate maximum deflection of 3.54×10^{-6} m under a 1 N load, corresponding to a stiffness of 2.821×10^5 N/m. The buckling

loads are 8.12×10^5 N in the x-direction and 1.67×10^5 N in the z-direction.

Parameter	Value
Max Deflection [m]	3.544×10^{-6}
Stiffness [N/m]	2.821×10^5
Buckling Load (X-dir) [N]	8.1173×10^5
Buckling Load (Z-dir) [N]	1.6747×10^5
Structure Weight [Kg]	250.50

Table 8.16: Structural performance of X16 topology

8.2.2.2. X16 – Maximum Volume Configuration

The first four mode shapes of the maximum volume variant are shown in Figure 8.9. As in the 2 Hz case, the first two modes correspond to intra-arm telescope bending, while Modes 3 and 4 reflect deformation between the bus and telescope structures.

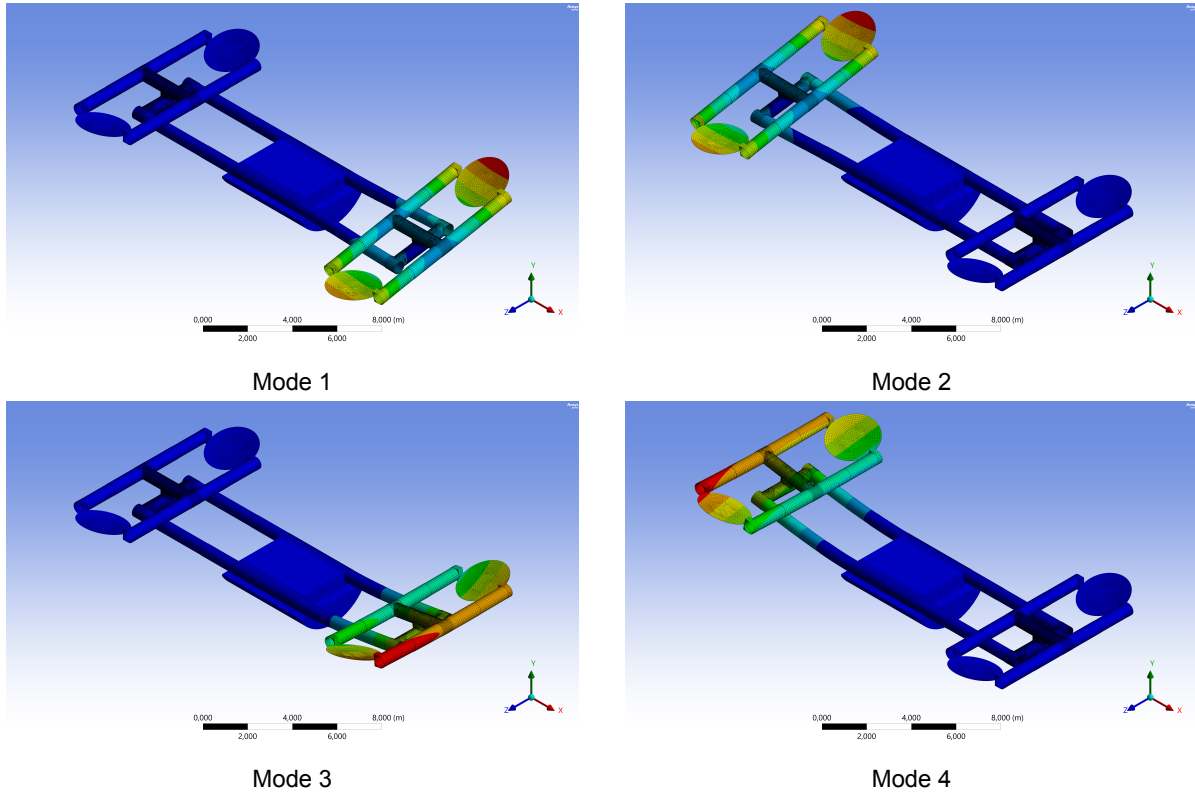


Figure 8.9: First four mode shapes of the X16 spacecraft in the maximum volume configuration

The natural frequencies in Table 8.17 show a clear increase compared to the 2 Hz configuration; however, the improvement is not as pronounced as that observed for the X8 variants. This is because the X16 design already required a significantly larger outer boom diameter to meet the 2 Hz constraint in the compact configuration, leaving less margin for further stiffness gains through diameter expansion. The fundamental mode reaches 4.39,Hz, with subsequent modes ranging from 4.5 to 9.3,Hz, reflecting enhanced structural rigidity across the full system.

Mode	1	2	3	4	5	6
Frequency (Hz)	4.3899	4.5044	4.7675	4.7709	8.9171	9.3506

Table 8.17: Natural frequency values for the X16 spacecraft in the maximum volume configuration (first 6 modes)

Table 8.18 confirms the enhanced structural performance. The deflection under 1 N is reduced to 742 nm, yielding a stiffness of 1.346×10^6 N/m. Buckling loads are increased to 1.01×10^6 N and 2.08×10^5 N in the x- and z-directions, respectively.

Parameter	Value
Max Deflection [m]	7.4243×10^{-7}
Stiffness [N/m]	1.346×10^6
Buckling Load (X-dir) [N]	1.0074×10^6
Buckling Load (Z-dir) [N]	2.0761×10^5
Structure Weight [Kg]	536.09

Table 8.18: Structural performance of X16 Max Volume topology

In summary, the X16 configuration provides a structurally efficient and dynamically stable layout for a 16-meter baseline. Even in its compact 2 Hz configuration, it meets design constraints, while the maximum volume variant offers significantly higher stiffness and frequency margins, supporting missions requiring improved resistance to optical path disturbances.

8.2.3. X32

The first four mode shapes of the X32 spacecraft are shown in Figure 8.10. As with other X-array configurations, the first and second modes show bending along the x-axis with deflection in the y-direction, localized to the booms connecting the telescopes on the same arm. The third and fourth modes correspond to bending around the z-axis with similar lateral deflections, primarily involving the structural elements between the telescope units and the spacecraft bus or beam combiner.

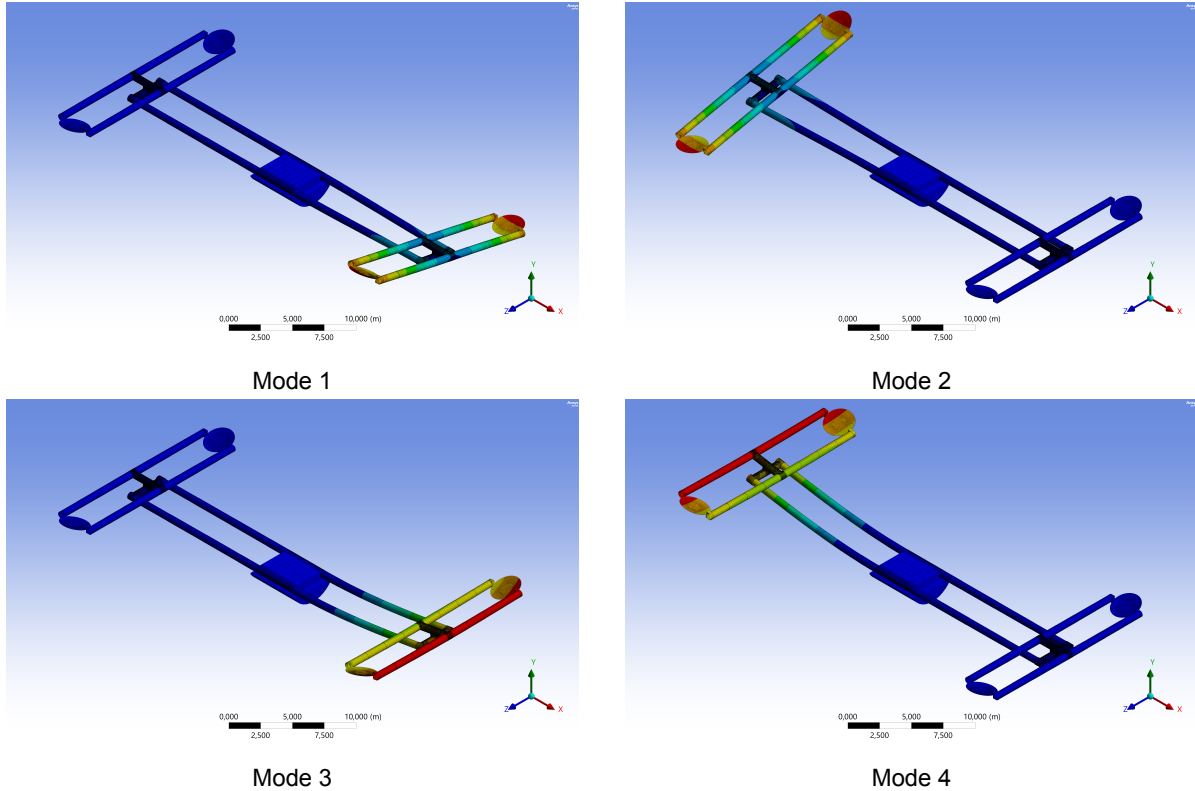


Figure 8.10: First four mode shapes of the X32 spacecraft

Table 8.19 lists the natural frequencies for the first six modes. The fundamental frequency of 1.3313 Hz does not meet the 2 Hz minimum threshold required to isolate the dynamic behavior from the isolator assembly, similar to the limitation observed in the Lin32 topology. This is a direct result of the extended boom lengths and the geometric constraints of the fairing, which limit further diameter increases and thus restrict structural stiffness enhancement.

Mode	1	2	3	4	5	6
Frequency (Hz)	1.3313	1.3315	1.3422	1.3425	2.5419	2.5429

Table 8.19: Natural frequency values for the X32 spacecraft (first 6 modes)

The structural performance data in Table 8.20 highlights the limitations of this configuration. The maximum static deflection is 7.56×10^{-6} m, yielding a stiffness of 1.323×10^5 N/m, which is notably lower than the X8 and X16 variants. Buckling loads are also reduced compared to

shorter-baseline configurations, with values of 5.99×10^5 N in the x-direction and 1.33×10^5 N in the z-direction.

Parameter	Value
Max Deflection [m]	7.5618×10^{-6}
Stiffness [N/m]	1.323×10^5
Buckling Load (X-dir) [N]	5.9931×10^5
Buckling Load (Z-dir) [N]	1.3332×10^5
Structure Weight [Kg]	940.90

Table 8.20: Structural performance of X32 topology

In conclusion, while the X32 configuration provides the longest interferometric baseline within the X-array family, its structural dynamics fall short of the required performance. The inability to meet the 2 Hz frequency constraint highlights the stiffness limitations imposed by fairing volume constraints. Future optimization may require material upgrades, alternate boom designs, or compromises in baseline length to satisfy dynamic isolation criteria.

8.3. Summary and Comparative Discussion

This section compares the key findings from the structural dynamics and stability analyses presented for all spacecraft topologies. The performance of each design is evaluated in terms of its natural frequencies, tip stiffness, maximum deflection, and buckling loads. By comparing both the 2 Hz-optimized and maximum volume configurations, critical trade-offs in deployable boom geometry, structural behavior, and packaging constraints can be fully appreciated.

8.3.1. Modal Performance Comparison

Table 8.21 presents a comparison of the fundamental natural frequencies (Mode 1) across all spacecraft configurations. The topologies exhibit a clear degradation in frequency with increasing baseline length, particularly in the L32 and X32 designs, which fail to meet the 2 Hz criterion. In contrast, all other topologies satisfy the modal requirement in their 2 Hz configurations. The maximum volume variants significantly enhance dynamic stiffness in all cases, with the X8 reaching nearly 16 Hz.

Table 8.21: Fundamental natural frequencies for all topologies

Topology	2 Hz Configuration (Hz)	Max Volume Configuration (Hz)
Lin8	2.055	13.387
Lin16	2.0452	3.5747
Lin32	N/A	1.0676
X8	2.0173	15.966
X16	2.0061	4.3899
X32	N/A	1.3313

8.3.2. Stiffness and Deflection Comparison

The stiffness performance, derived from the static structural analysis under a 1 N tip load, is summarized in Table 8.22. The maximum volume configurations greatly improve resistance to deformation, particularly in the X8 variant, which shows a two-order-of-magnitude increase in tip stiffness. Among the configurations, X-array topologies outperform their linear counterparts due to its shorter boom spans and more compact architecture.

Table 8.22: Tip deflection and equivalent stiffness under 1 N load

Topology	Deflection	Stiffness (N/m)
Lin8 (2 Hz)	9.05 μm	1.106×10^5
Lin8 (MaxVol)	0.182 μm	5.486×10^6
Lin16 (2 Hz)	7.56 μm	1.324×10^5
Lin16 (MaxVol)	2.73 μm	3.660×10^5
Lin32 (2 Hz)	24.17 μm	4.138×10^4
X8 (2 Hz)	4.22 μm	2.370×10^5
X8 (MaxVol)	55.9 nm	1.790×10^7
X16 (2 Hz)	3.54 μm	2.821×10^5
X16 (MaxVol)	0.742 μm	1.346×10^6
X32 (2 Hz)	7.56 μm	1.323×10^5

8.3.3. Buckling Capacity Comparison

Table 8.23 presents the critical buckling loads for all configurations as computed from eigenvalue buckling analysis. While buckling is generally not a limiting design driver for deployable structures, it remains essential to verify that each topology offers sufficient compressive capacity to survive launch loads and potential thermal contraction in space.

The linear configurations were assessed for buckling along the axial direction of their primary booms (X-direction), which is aligned with the launch load path. In contrast, the X-array configurations were evaluated for buckling in both the X- and Z-directions due to their orthogonal boom layout. These results offer insight into the relative structural robustness of each design, particularly under asymmetric loading scenarios.

All topologies exhibit buckling loads well above typical axial launch loads, which are often in the range of 10^4 – 10^5 N for instrument-class payloads. As such, the computed buckling capacities provide an additional safety margin rather than a critical constraint. Nonetheless, the Lin32 and X32 topologies show the lowest margins due to their extended boom lengths and limited geometric stiffness, which reinforces the value of checking these characteristics as part of a complete structural verification process.

Table 8.23: Critical buckling loads for all configurations

Topology	Buckling Load X-dir (N)	Z-dir (if applicable) (N)
Lin8 (2 Hz)	2.143×10^6	N/A
Lin8 (MaxVol)	3.471×10^6	N/A
Lin16 (2 Hz)	1.284×10^6	N/A
Lin16 (MaxVol)	3.677×10^6	N/A
Lin32 (2 Hz)	8.436×10^5	N/A
X8 (2 Hz)	1.333×10^5	2.389×10^5
X8 (MaxVol)	1.136×10^6	5.614×10^5
X16 (2 Hz)	8.117×10^5	1.675×10^5
X16 (MaxVol)	1.007×10^6	2.076×10^5
X32 (2 Hz)	5.993×10^5	1.333×10^5

8.3.4. Mass Comparison

Table 8.24: Structural mass of the deployable truss for each topology and packaging variant (telescope and bus masses are identical for all concepts and are therefore omitted).

Topology	2 Hz Configuration [kg]	Max Volume Configuration [kg]
Lin8	26.3	102.2
Lin16	137.6	204.5
Lin32	N/A	401.9
X8	57.6	326.0
X16	250.5	536.1
X32	N/A	940.9

The X-array topologies exhibit a consistently higher structural mass compared to the linear designs for all baseline lengths and maximum volume variants. This increased mass is primarily

driven by the additional structure required to realize the X-array geometry. Specifically, the X-array incorporates a two rotation mechanisms and associated support structure, alongside the use of twelve telescopic booms, whereas the linear configurations rely on only eight telescopic booms. Even in the X8 configuration, where the booms are not telescopic, the total net boom length exceeds that of the linear counterpart due to the additional spans needed for the rotational mechanism and to form the X-array layout.

This mass penalty reflects the intrinsic mechanical complexity of the X-array topology and must be considered alongside its dynamic and structural benefits. Although Ariane 6 provides sufficient launch margin of 11.5 t, every extra kg of structure translates directly into restricting propellant or scientific payload weight. A dedicated mission-level study is therefore recommended to quantify the maximum weight that can be allocated to the spacecraft structure.

8.3.5. Cross-Topology Observations

Several important trends emerge when comparing linear and X-array configurations:

- **Dynamic Margin:** X-array topologies generally provide higher dynamic margins, except for X32, which like Lin32, fails to meet the 2 Hz constraint.
- **Structural Efficiency:** X-array designs benefit from shorter boom spans in the spacecraft length, yielding lower deflections and higher buckling resistance.
- **Scalability Limits:** Both Lin32 and X32 illustrate the challenges of achieving modal isolation at long baselines under fairing volume constraints.
- **Optimization Sensitivity:** Maximum volume configurations offer substantial structural gains for short-to-mid baseline designs, but yield diminishing returns in longer systems where boom sizes are already near fairing limits.
- **Mass Consideration:** The X-array topologies exhibit significantly higher structural mass than linear configurations for all baseline lengths and configurations. This is a direct consequence of their additional telescopic elements, rotation mechanisms, and the structural reinforcements necessary to support the X-array geometry.

8.3.6. Conclusion

The X-array configurations exhibit superior static and dynamic performance compared to linear variants for equivalent baselines. While Lin8 benefits from compact stowage, X8 delivers significantly greater stiffness and frequency margins. Among long-baseline designs, Lin32 and X32 both fail to meet modal criteria, highlighting the need for geometric redesign or alternate materials. These findings provide a clear framework for selecting feasible topologies and justify the speculative investigations in the following section into shape and wall thickness modifications.

However, this enhanced static and dynamic performance in the X-array topologies comes at the cost of increased mechanical complexity and structural mass. Unlike linear configurations, X-array spacecraft require additional telescopic elements, rotation mechanisms, and structural reinforcements to achieve the final deployed geometry. This results in a significantly higher structural mass for all baseline lengths and configurations, as detailed in the mass comparison. Also these additional deployment systems introduce potential failure modes and demand

careful integration of deployment sequencing, synchronization, and structural locking. Furthermore, although the X-array offers clear advantages in terms of stiffness and natural frequency, it does not exhibit superior buckling resistance in the deployed state compared to the linear designs. Consequently, the choice between linear and X-array topologies involves a trade-off between dynamic performance, mechanical simplicity, and mass efficiency, which must be weighed in the context of mission reliability and launch mass budget.

8.4. Improving L32 Boom Design

8.4.1. Effect of Elliptical Cross-Section on Natural Frequency Behavior

The geometry of the deployable booms plays a critical role in shaping the dynamic response of the spacecraft. To investigate whether the L32 topology could achieve a minimum first natural frequency of 2 Hz, a geometric redesign was explored wherein the booms were given an elliptical cross-section. The elliptical booms retain the same minor axis as the original circular design but expand the major axis significantly, up to 862 mm, to take advantage of unused fairing space in the orthogonal direction. This was done to evaluate the theoretical potential of increasing vertical bending stiffness. The elliptical boom is shown in Figure 8.11.

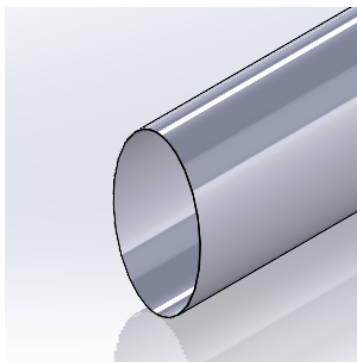


Figure 8.11: Elliptical boom

Since this is an informative investigation to see whether it is useful to explore elliptical boom designs in future work, and not an actual spacecraft to be directly compared to the comprehensive designs of the Linear and X-array topologies from above, the elliptical boom is not telescopic but simply a straight boom to simplify this preliminary analysis. Using the elliptical booms, a new version of the Lin32 spacecraft was designed and is shown in Figure 8.12. A modal analysis was performed to see how the modes would change compared to the Lin32 using circular booms. These results are shown in Table 8.25.

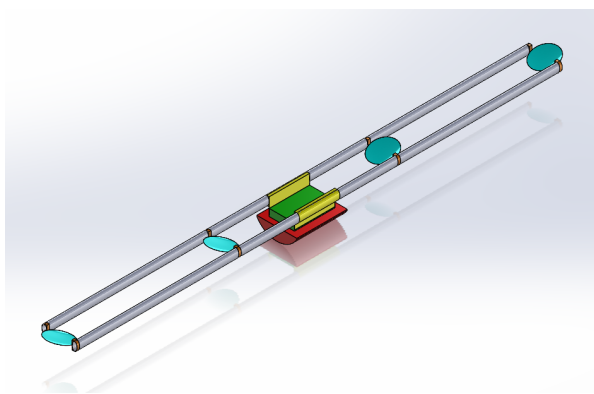


Figure 8.12: Simplified Lin32 using elliptical booms

Configuration	Mode 1	Mode 2	Mode 3	Mode 4
Circular boom	1.0676	1.0676	2.9212	2.9397
Elliptical boom	1.4409	1.4413	2.5591	2.5609

Table 8.25: First four natural frequencies for L32 configurations

The first and second natural frequencies increase from 1.07 Hz to 1.44 Hz due to enhanced stiffness in the vertical direction (major axis), confirming the effectiveness of the elliptical design in improving symmetric bending modes. However, the third and fourth frequencies *decrease* from approximately 2.92 Hz and 2.94 Hz to 2.56 Hz and 2.56 Hz, indicating a loss in stiffness or additional dynamic coupling in those modes. This trend is explained by three primary mechanisms:

1. Mass Redistribution and Increased Cross-Sectional Area While the second moment of area in the vertical direction (I_y) increases, the total cross-sectional area also increases, thereby raising the mass per unit length μ . Since the frequency of bending modes follows:

$$f \propto \sqrt{\frac{EI}{\mu L^3}}, \quad (8.1)$$

an increase in mass without a proportional increase in stiffness in all directions results in lower frequencies for certain modes.

2. Torsional Stiffness Reduction For circular cross-sections, torsional rigidity is maximized due to the uniform radial distribution of material. The torsional stiffness is given by:

$$GJ \quad (\text{torsional rigidity}) \quad (8.2)$$

where G is the shear modulus and J is the polar moment of inertia. For elliptical thin-walled sections, J is significantly lower than that of a circular section of comparable size, especially as the aspect ratio b/a increases. Since the 3rd and 4th modes may contain coupled torsional components or involve out-of-phase motion between the booms, the reduction in GJ contributes to a lower restoring torque and, hence, lower modal frequencies.

3. Coupling Effects and Mode Reordering Changing the cross-section alters the distribution of stiffness across the structure, which affects modal orthogonality and may cause mode reordering. This can redistribute vibrational energy into unintended modes, resulting in reduced frequencies even if geometric stiffness remains unchanged in that direction.

In summary, the elliptical redesign successfully improves vertical bending performance, increasing the first two frequencies. However, it also leads to a modest decrease in the third and fourth modes due to increased mass and reduced torsional stiffness. This highlights the importance of holistic structural evaluation when modifying cross-sectional shapes.

8.4.2. Effect of Increasing Wall Thickness on Natural Frequency Behavior

To further enhance the dynamic response of the elliptical boom, the wall thickness was increased from 1 mm to 2 mm. This adjustment maintains the same elliptical minor and major diameter while doubling the structural material volume, thereby increasing both bending and torsional stiffness.

Configuration	Mode 1	Mode 2	Mode 3	Mode 4
Elliptical boom with 2 mm wall thickness	1.9779	1.9784	2.8057	2.8163

Table 8.26: First four natural frequencies for elliptical boom with a wall thickness of 2 mm

The first two frequencies now approach the 2 Hz design target, while the 3rd and 4th frequencies—previously degraded by the switch to elliptical geometry—recover and even slightly improve compared to the circular baseline. The increased stiffness results from the fact that, for thin-walled elliptical beams, the second moment of area scales linearly with wall thickness t :

$$I_y = \frac{\pi}{4} ab^3 t, \quad (8.3)$$

$$I_x = \frac{\pi}{4} a^3 b t. \quad (8.4)$$

Thus, a doubling of t leads to a proportional increase in bending stiffness EI , while also improving torsional rigidity GJ . These changes collectively contribute to the observed frequency increases.

By increasing the wall thickness by just 0.1 mm, the first two modes exceeded the minimum requirement of 2 Hz, demonstrating that optimizing the shape and increasing the wall thickness could enable longer baselines to achieve a minimum first natural frequency of 2 Hz (table 8.27). However, this comes at the cost of a significantly higher mass. In the case of the elliptical boom with a 2.1 mm wall thickness, a major diameter of 862 mm, and a minor diameter of 620 mm, the mass is 929.68 kg compared to 401.87 kg for the circular Lin32, a 130% increase. That is the price of achieving the requirements for longer baselines.

Configuration	Mode 1	Mode 2	Mode 3	Mode 4
Elliptical boom with 2.1 mm wall thickness	2.0207	2.0213	2.8617	2.8708

Table 8.27: First four natural frequencies for elliptical boom with a wall thickness of 2.1 mm

These findings demonstrate that a combination of elliptical geometry and increased wall thickness can feasibly meet the modal requirements for the L32 topology. Nonetheless, selecting the optimal shape, wall thickness, and deployment configuration remains a multi-variable problem, and a dedicated structural optimization study is recommended as future work.

9

Conclusion

The primary objective of this thesis was to investigate how changes in structural and deployment design factors affect the overall volume of a space-based nulling interferometer spacecraft, and how these factors can be managed to ensure compatibility with the Ariane 6 launch vehicle. To answer this main research question, the study focused on four key goals:

- Identifying key inputs for the mechanical design and understanding their impact on the optical system.
- Sizing the booms and deployment mechanisms, ensuring they meet vibrational stability requirements and offer precise deployment control.
- Developing a stowage and deployment strategy for integration with the Ariane 6.
- Conducting 3D modeling to verify spacecraft dimensions and ensure proper stowage.

Key Mechanical Inputs and Their Optical Impact The early chapters established that optical path length stability, crucial for deep nulling, is directly influenced by structural choices such as boom geometry and length, material selection, and deployment mechanism performance. For both linear and X-array configurations, the structure must exhibit high bending stiffness and minimal thermal expansion. These requirements were met by employing pitch based carbon-fiber-reinforced polymer for all designs which show great mechanical and thermal stability. Furthermore, deployment tolerances and mechanical alignment play a critical role in maintaining optical performance post-deployment.

Boom Sizing and Deployment Mechanism Selection To achieve the required baseline lengths and maintain structural integrity, various deployment mechanisms were evaluated. Telescopic booms emerged as the most viable solution due to their compactness, structural stiffness, and compatibility with the Ariane 6 fairing. Articulated booms, while mechanically more voluminous in their stowed configuration, were considered as a fallback option in case telescopic booms fall short in performance. As shown in Chapter 7.4, an articulated Lin16 design was developed to illustrate this alternative, demonstrating how the booms must fold inward into a Z-shaped layout, resulting in significantly higher fairing volume usage and reduced

space for other spacecraft components such as the sunshield. However, articulation mechanisms were selected as a secondary deployment system for the X-array topologies due to their ability to rotate the booms into the required X geometry. Truss structures, despite reasonable stiffness characteristics, were excluded due to their excessive diameters and poor stowage efficiency. Hence, the deployment strategy adopted in this study combines telescopic mechanisms for linear deployments and articulated-telescopic systems for X-array configurations.

Stowage and Deployment Strategy for Ariane 6 Compatibility The spatial constraints of the Ariane 6 long fairing, particularly its 4.6 m maximum diameter and internal taper beyond 11.2 m, shaped the stowage strategy. 3D CAD models confirmed that both linear and X-array topologies could be accommodated within these dimensions for baseline lengths up to 32 m. For linear designs, telescoping segments were stacked to stow into a compact vertical assembly, while for 4T X configurations, articulation mechanisms enabled an initial 90° rotation prior to telescoping. These findings demonstrate that all systems up to 32 m can be stowed within Ariane 6.

Dynamic and Structural Performance Modal and structural analysis revealed that X-array topologies offer superior stiffness and natural frequency margins compared to linear equivalents. The X8 configuration, for instance, outperformed Lin8 in dynamic response while still fitting within fairing constraints. However, long-baseline concepts like Lin32 and X32 failed to meet the 2 Hz fundamental frequency requirement, emphasizing the need for geometric redesign or advanced materials for such missions.

Notably, this improved dynamic performance in X-arrays comes with increased mechanical complexity. These topologies demand more telescopic segments and articulation mechanisms, raising risks related to deployment reliability and structural locking. Consequently, while X-array designs are in terms of structural stiffness more favorable, they involve a trade-off between performance and simplicity that must be carefully balanced against mission risk tolerance and integration constraints.

Final Remarks This thesis presents a comprehensive framework for managing the trade-offs between structural performance, stowage feasibility, and deployment complexity in the design of a space-based nulling interferometer. By evaluating multiple spacecraft topologies in terms of optical, mechanical, and geometric constraints, it provides a clear understanding of how structural and deployment design factors influence the overall volume of the spacecraft, and how these factors can be managed to ensure compatibility with the Ariane 6 launch vehicle. Designs with baseline lengths up to 16 m were shown to fit within the fairing while meeting all mechanical requirements. The modular telescopic boom architecture developed in this work offers a robust foundation for the future design of space-based nulling interferometer missions.

Recommendations and future work While this study provides a high-level design framework and evaluates the structural feasibility of several topologies, several aspects warrant further investigation.

First, the results indicate that the use of elliptical boom geometries and increased wall thickness can enable longer baseline configurations such as L32 to meet modal requirements.

However, the choice of boom shape, wall thickness, and deployment method introduces a complex, multi-variable design space. A dedicated structural optimization study is recommended to systematically explore this trade-off, incorporating constraints on mass, stiffness, and manufacturability. Furthermore, the deployment actuators and their control strategies should be developed in more detail. Special attention must be given to asymmetric deployment behavior, where a mismatch in deployment speed between different sides could lead to mechanical locking or jamming of the system.

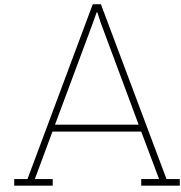
Second, thermal considerations were only implicitly treated through material selection and stowage assumptions. A detailed thermal analysis, including sunshield sizing and layout, is essential to validate whether the passive cooling requirements can be met in orbit. This analysis should also feed back into the geometric design to ensure the sunshield integrates cleanly with the stowed configuration and does not interfere with deployment. In addition, regarding the eventual choice of spacecraft topology, as the sunshield size will likely differ between topologies. A trade-off must be conducted to assess whether the improved static and dynamic performance of the X-array topologies outweighs their larger sunshield size, added structural mass, and more complex deployment sequence. It may ultimately be preferable to accept a reduction in structural performance in exchange for a lighter structure, a smaller or simpler sunshield, and fewer failure points.

Finally, while no frequency-versus-deflection analysis under representative microvibration conditions was conducted due to the absence of suitable disturbance force inputs, this forms an important area for future work. Such an analysis would help verify the dynamic performance of the structure under realistic disturbance loads and further de-risk the design. Together, these future efforts would further mature the structural and thermal design of space-based nulling interferometers, improving readiness for a mission implementation phase.

References

- [1] Arianespace. *Ariane 6 User's Manual, Issue 2 Revision 0*. Arianespace. 2021.
- [2] R. K. Barry et al. "The Fourier-Kelvin Stellar Interferometer: A Progress Report and Preliminary Results from our Laboratory Testbed". In: *Proceedings of the 2nd TPF/Darwin International Conference*. 2006, pp. 547–552.
- [3] L. Bourrec et al. "Telescopic Boom for Space Applications Engineering Model". In: *14th European Space Mechanisms and Tribology Symposium (ESMATS)*. Constance, Germany, 2011, pp. 337–341.
- [4] Carpenter Technology Corporation. *CarTech Invar 36 Alloy - Data Sheet*. URL: <https://www.carpentertechnology.com/hubfs/7407324/Material%20Safety%20Data%20Sheets/Invar%2036.pdf>.
- [5] Nippon Graphite Fiber Corporation. *Pitch-Based Carbon Fibers - Granoc XN-90/XN-60*. URL: <https://www.ngfworld.com/e/products/carbon/granoc.html>.
- [6] W. C. Danchi et al. "The Fourier Kelvin Stellar Interferometer (FKSI): A Review, Progress Report, and Update". In: *Proceedings of SPIE*. Vol. 7013. 2008, 70132Q.
- [7] W. C. Danchi et al. "The Fourier-Kelvin Stellar Interferometer: A Low Complexity, Low Cost Space Mission for High-Resolution Astronomy and Direct Exoplanet Detection". In: *Astrophysical Journal* 579 (2003), pp. L57–L60.
- [8] European Space Agency. *How nulling interferometry works*. 2002. URL: https://www.esa.int/ESA_Multimedia/Images/2002/03/How_nulling_interferometry_works.
- [9] Gabrian International. *7075 Aluminum Alloy - Properties*. URL: <https://www.gabrian.com/7075-aluminum-properties/>.
- [10] J. Loicq et al. "TN2- ESA nulling interferometry - Technology review and trade-off analysis". In: *Internal ESA Report* (2024).
- [11] LLC MatWeb. *Ti-6Al-4V Titanium Alloy Property Data*. URL: <https://asm.matweb.com/search/specificmaterial.asp?bassnum=mtp641>.
- [12] M. Menzel et al. "The Design, Verification, and Performance of the James Webb Space Telescope". In: *Publications of the Astronomical Society of the Pacific* 135 (2023), 058002 (42pp).
- [13] Mehran Mobrem and Chris Spier. "Design and Performance of the Telescopic Tubular Mast". In: *Proceedings of the 41st Aerospace Mechanisms Symposium*. Developed by Astro Aerospace, a division of Northrop Grumman Aerospace Systems. Jet Propulsion Laboratory. Pasadena, California: NASA, 2012.
- [14] NASA. *Webb's First Deep Field (NIRCam Image)*. 2022. URL: <https://webbtelescope.org/contents/media/images/2022/035/01G7DCWB7137MYJ05CSH1Q5Z1Z%7D>.

- [15] M. Parisse and F. Angeletti. “Thermo-mechanical jitter in slender space structures”. In: *International Journal of Space Engineering* (2024).
- [16] L. Puig, A. Barton, and N. Rando. “A review on large deployable structures for astrophysics missions”. In: *Acta Astronautica* 67 (2010), pp. 12–26. DOI: 10.1016/j.actaastro.2010.02.021.
- [17] C. Dandumont R. Laugier and D. Defrère. “High-Level Requirement Consolidation”. In: *Internal ESA Report* (2023).
- [18] Y. Tang et al. “Five-Meter Nonmagnetic Telescopic Tubular Mast: Design, Test, and On-Orbit Application”. In: *Space Science and Technology* 4 (2024). DOI: 10.34133/space.0171.
- [19] Jacob Job Wijker. *Spacecraft Structures*. Springer-Verlag Berlin Heidelberg, 2008. ISBN: 978-3-540-75552-4. DOI: 10.1007/978-3-540-75553-1.
- [20] Wikipedia contributors. *Angular resolution*. 2024. URL: https://en.wikipedia.org/wiki/Angular_resolution.
- [21] X. Xing and Z. Shen. “Thermoelastic–structural dynamics analysis of a satellite with composite thin-walled boom”. In: *Journal of Thermal Engineering* (2022).
- [22] Kan Yang et al. “Thermal Model Performance for the James Webb Space Telescope OTIS Cryo-Vacuum Test”. In: *48th International Conference on Environmental Systems*. NASA Goddard Space Flight Center. Albuquerque, New Mexico: NASA, 2018. URL: <https://ntrs.nasa.gov/api/citations/20205007347/downloads/20205007347.pdf>.
- [23] S. ZingMing et al. “Experimental investigation of the thermally induced vibration of a space boom section”. In: *Science China Physics, Mechanics & Astronomy* 58.4 (2015), p. 044601. DOI: 10.1007/s11433-014-5622-y.



Design Requirements

Requirement Type	Requirement Description
SREQ1	The instrument shall be able to directly detect and characterise temperate rocky exoplanets.
FREQ1	The instrument shall observe the thermal light of exoplanets around nearby stars.
FREQ2	The instrument shall measure the spectrum of exoplanets.
FREQ3	The instrument shall be able to detect new temperate rocky exoplanets.
TREQ1	The concept shall use multi-aperture nulling interferometry as a baseline technique but may refer to sampled aperture nulling for technology demonstration.
TREQ2	The implementation shall not require formation flight.
TREQ3	Payload shall be compatible with launch on Ariane 6.
TREQ5	The instrument shall target the mid-Infrared wavelength range (3–20 μm).
TREQ8	The instrument shall yield an inner working angle lower than 300 mas at 10 μm .
TREQ9	The instrument shall reach a level of starlight suppression lower than 10^{-5} at 10 μm .
TREQ10	The instrument shall reach a sensitivity lower than 1 μJy at 10 μm .
TREQ11	The instrument shall reach a limiting magnitude lower than 30 Jy at 10 μm .
TREQ12	The instrument shall offer a minimum spectral resolution of 20.
TREQ13	The instrument shall use between three and five collectors.

Table A.1: List of scientific (SREQ), functional (FREQ), and technical (TREQ) requirements.

B

MATLAB Script for SCB Shape Adjustments

The following MATLAB script computes the required parameter x for the spacecraft bus (SCB) shape and saves the results to a SolidWorks design table.

```
clc; clear; close all;

V = 18; % Volume in m^3
t = 0.1; % Thickness in meters
h = 4; % Height in meters
r = 2.3; % Radius in meters

x_computed = compute_x_from_V(V, t, h, r);
d = r - x_computed;
L = 2 * sqrt(r^2 - d^2);

V_actual = compute_volume(x_computed, t, h, r);

% Parameter Checks
if x_computed < 0 || x_computed > r
    error('Computed x is out of bounds! x must be between 0 and r.');
```

```
end

if L <= 0 || L > 2*r
    error('Invalid chord length L! Check input parameters.');
```

```
end

if abs(V_actual - V) > 1e-6 % Allow small numerical error
    warning('Computed volume does not match the desired V! Difference: %.6f m^3', V_actual)
```

```
end
```

```

% Convert values to mm
h_mm = h * 1000;
L_mm = L * 1000;
r_mm = r * 1000;

% Create SolidWorks Design Table Data
design_table = cell(2, 4);
design_table(1, :) = {'Configuration Name', 'H@Boss-Extrude1', 'L@Sketch1', 'R@Sketch1'}; %
design_table(2, :) = {'SCB', h_mm, L_mm, r_mm}; % Values

output_filename = 'SolidWorks_DesignTable.xlsx';
writecell(design_table, output_filename);

% Display Results
fprintf('Computed x: %.4f meters (%.2f mm)\n', x_computed, x_computed * 1000);
fprintf('Computed L: %.4f meters (%.2f mm)\n', L, L_mm);
fprintf('Computed Volume: %.6f m^3\n', V_actual);
fprintf('Design Table saved to "%s"\n', output_filename);

% Function to Compute x using fsolve
function x = compute_x_from_V(V, t, h, r)
    volume_equation = @(x) volume_function(x, V, t, h, r);
    x_initial_guess = r / 2;
    options = optimset('Display', 'off'); % Suppress output
    x = fsolve(volume_equation, x_initial_guess, options);
end

function V_actual = compute_volume(x, t, h, r)
    theta = 2 * acos((r - x) / r); % in radians
    A_sector = (r^2 / 2) * theta;
    A_triangle = (r - x) * sqrt(r^2 - (r - x)^2);
    L = 2 * sqrt(r^2 - (r - x)^2);
    A_rectangle = L * t;
    A_total = A_sector - A_triangle + A_rectangle;
    V_actual = A_total * h;
end

function V_calc = volume_function(x, V, t, h, r)
    % Compute the volume equation given x, V, t, h, and r
    V_actual = compute_volume(x, t, h, r);
    V_calc = V_actual - V; % Solve for V_calc - V = 0
end

```